Experimental Studies in a Supersonic Through-Flow Fan Blade Cascade

by

Christopher J. Chesnakas

Dissertation submitted to the Faculty of the

Virginia Polytechnic Institute and State University

in partial fulfillment of the requirements for the degree of

Doctor of Philosophy

in

Mechanical Engineering

APPROVED:

Dr. Wing. F. Ng, Chairman

Dr. Clinton L. Dancey

Dr. Walter F. O'Brien

Dr. Larry A. Roe

Dr. Joseph A. Schetz

May, 1991

Blacksburg, Virginia

Experimental Studies in a Supersonic Through-Flow Fan Blade Cascade

by

Christopher J. Chesnakas

Dr. W. F. Ng, Chairman

Mechanical Engineering

(ABSTRACT)

An investigation has been performed of the flow in a supersonic through-flow fan blade cascade. The blade shapes are those of the baseline supersonic through-flow fan (STFF) under investigation at the NASA Lewis Research Center. Measurements were made at an inlet Mach number of 2.36 over a 15° range of incidence. Flowfield wave patterns were recorded using spark shadowgraph photography and steady-state instrumentation was used to measure blade surface pressure distributions and downstream total and static pressure distributions. A two-dimensional LDV system was used to map the downstream flowfield. From these measurements, the integrated loss coefficients are presented as a function of incidence angle along with analysis indicating the source of losses in the STFF cascade. The results are compared with calculations made using a two-dimensional, cell-centered, finite-volume, Navier-Stokes code with upwind options. Good general agreement is found at design conditions, with lesser agreement at off-design conditions. Analysis of the leading edge shock shows that the leading edge radius is a major source of losses in STFF blades. Losses from the leading edge bluntness are convected downstream into the blade wake, and are difficult to distinguish from viscous losses. Shock losses are estimated to account

for 70% to 80% of the losses in the STFF cascade.

Acknowledgements

I would like to thank the members of my advisory committee — Dr. Wing F. Ng, Dr. Clinton L. Dancey, Dr. Walter F. O'Brien, Dr Larry A. Roe, and Dr. Joseph A. Schetz — for the time and effort they invested in this project over the last three years. I would especially like to thank Dr. Ng for his guidance and support through frustrating times.

I would like to thank Rodney Bowersox for his help with the flow visualization and pressure probe measurements, and Philip Andrew for his help with the LDV measurements and the CFD calculations. I would also like to thank Kumud Ajmani and Jerry Brock for their guidance through the world of computational fluid dynamics.

I would also like to acknowledge the support of the Turbomachinery Technology Branch at NASA Lewis Research Center, Dr. L. J. Bober, Branch Chief. I would like to thank Dan Tweedt, the contract monitor for this program, for his assistance and oversight, and Mr. C. L. Ball for his continued support of this program.

Table of Contents

List of Illustrations

List of Tables

List of Symbols

c	chord length
C_D	coefficient of drag
d	diameter
i	incidence angle relative to design
Kn	Knudsen number
M	Mach number
p	pressure
r	relative to the particle
Re	Reynolds number
s	blade spacing
T	temperature
t	time
u	velocity component in the y-direction
V	total velocity
w	uncertainty
x	distance in the axial direction
y	distance in the direction of the cascade line

z distance in the spanwise direction

α flow angle

β flow angle relative to the axial direction

γ ratio of specific heats

δ shock flow turning angle

κ beam half angle

λ molecular mean free path

μ absolute viscosity

ν kinematic viscosity

ρ density

σ solidity, *c/s*

ω loss coefficient

Superscripts

$*$ normalized

$\bar{}$ averaged

$'$ fluctuating component

Subscripts

0 settling chamber

1 upstream of the casacade

2 downstream of the cascade

3	far downstream of the cascade (mixed out)
b	bluntness
f	fluid
meas	measured
p	Pitot or particle (Appendix C)
pg	passage
r	relative
s	shock
t	total
v	viscous
w	wake

Chapter 1

Introduction

The rapid growth in air traffic across the Pacific has sparked renewed interest in supersonic passenger transports. The current generation of aircraft engines, however, do not perform well at supersonic cruise. In order to make such supersonic transports economically viable, supersonic cruise engines must be improved in both weight and efficiency.

One component of the supersonic cruise engine which could be improved substantially in both of these areas is the inlet. A supersonic inlet for a typical gas turbine engine must be capable of decelerating the supersonic inflow to subsonic speeds at the engine face. This deceleration of the flow is not easily managed, and shock and boundary layer losses are inevitable. In order to minimize these losses, a long and heavy inlet employing variable geometry is necessary. Thus, an inlet for a typical supersonic cruise engine is both heavy and inefficient.

As far back as 1958, Ferri[1] pointed out that a fan capable of accepting supersonic axial flow would allow for the use of a light, simple inlet with high pressure recovery at supersonic cruise. As envisioned by Ferri, the fan would operate with a normal shock in the rotor passage, and the outlet flow would be subsonic. The efficiency of such rotors, however, is not high, due to the large losses from the passage normal shock. A more promising way of increasing the compression system (inlet plus compressor) efficiency is to employ a fan in which the flow is

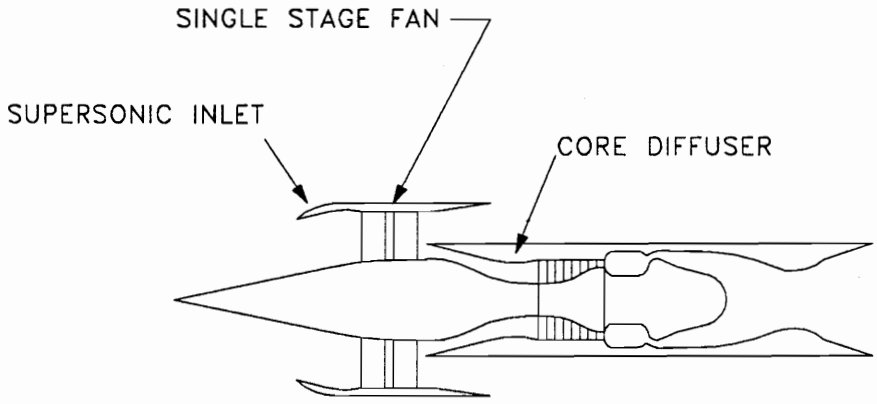

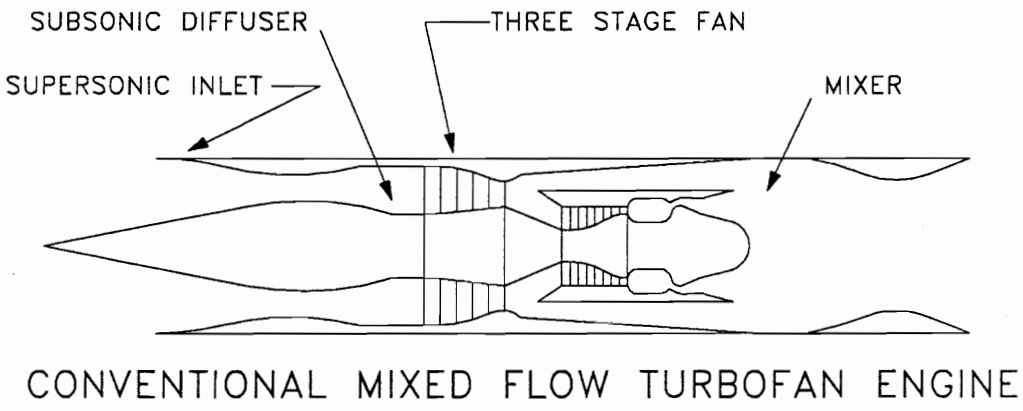

Figure 1. Comparison of STFF Engine and Conventional Supersonic Turbofan

axially supersonic throughout. An engine employing such a fan is sketched in Figure 1. First proposed by Advanced Technology Laboratory Inc. and studied under NASA contract[2], the core flow in this engine would still need to be diffused to subsonic velocity, but the losses in such a diffusion process would be confined to only the fraction of air which goes through the core, and thus overall losses would be reduced. The weight of the supersonic through-flow fan (STFF) equipped engine would be reduced relative to a conventional turbofan engine since, not only would a lighter inlet be needed, but fewer stages would be required — the STFF being capable of much higher pressure ratios than lower speed fans.

Several studies have been conducted to estimate the performance potential of the STFF equipped engine. Tavares[3] suggested that a STFF efficiency of 68% is required to provide a performance advantage over a turbojet engine for a Mach 2.7 transport. Champagne[4] suggested that a STFF engine equipped Mach 2.3 transport would have a 14% increase in range compared to a conventional turbofan due to the 9% reduction in specific fuel consumption and 31% reduction in installed engine weight. Franciscus and Maldonado[5] found that for a Mach 3.2 transport with a 5000 mile range, a STFF engined aircraft would have a takeoff gross weight 13% less than an aircraft equipped with an advanced turbine bypass engine.

Unfortunately, all these studies suffer from a lack of experimental data confirming the assumed fan performance. Only two experimental studies to date have examined the performance of supersonic axial blading. Savage et al.[6] examined the performance of a transonic rotor operating above design speed in a Mach 1.5 flow and obtained limited performance data. Breugelmans[7] tested a rotor designed for Mach 1.5 inlet flow, but was unable to obtain substantial data due to an early rotor blade failure. In both cases, the rotor operated with a normal shock in the rotor, and therefore, the exit velocity was axially subsonic.

In order to better quantify the performance potential of the STFF, the NASA Lewis

Table 1. STFF Design Parameters

	Rotor	Stator
Rotative Speed (rpm)	17,189	0
Tip Speed (m/s)	457	0
Total Pressure Ratio	2.7	0.91
Hub Radius (cm)	17.78	17.78
Tip Radius (cm)	25.40	25.40
Blade Number	44	52
Chord (cm)	9.04(hub) to 11.30(tip)	8.33(hub) to 9.27(tip)
Solidity, σ (blade chord to spacing ratio)	3.56(hub) to 3.11(tip)	3.88(hub) to 3.02(tip)
Aspect Ratio (span to mean chord ratio)	0.97	0.86
Maximum Thickness/Chord, percent	4 to 7	5
Leading Edge Thickness/Chord, percent	0.15 to 0.19	0.14 to 0.15
Trailing Edge Thickness/Chord, percent	0.27 to 0.37	0.27

Research Center has undertaken a program to design, build, and test a proof-of-concept supersonic through-flow fan stage. The fan stage has been designed for a total pressure ratio of 2.45 at a fan face Mach number of 2.0. The design of the fan stage and the details of the blading are described in Schmidt et al.[8] . The dimensions of the stage and the design operating parameters as outlined in Schmidt are summarized in Table 1.

As a part of this program, 2-D cascade studies of mean blade sections have been undertaken in the VPI supersonic cascade wind tunnel. These cascade studies have been undertaken in order to (1) obtain an understanding of the flow physics and loss mechanisms in a supersonic through-flow fan, (2) measure the cascade losses so that the performance of a STFF equipped engine can be better predicted, (3) verify the ability of CFD codes to accurately model the flow through STFF blades, and (4) establish a database for STFF analysis codes.

This paper will detail the results of the cascade studies and analyze the results in light of

the above stated objectives. Before presenting the results, the wind tunnel, cascade, and instrumentation used to analyze the cascade will be described. The results will be compared to CFD calculations of the cascade flow in order that the capabilities and limitations of these codes can be assessed for the problem of STFF design. The results of the testing and the computational predictions of the flow will be analyzed in light of an empirical shock loss model in order to better understand the loss mechanisms in the STFF cascade. A detailed analysis of the measurement uncertainties will be presented in the appendix.

Chapter 2

Facilities

2.1 Wind Tunnel

All measurements were conducted in the VPI supersonic cascade wind tunnel. This blow down facility was equipped with a two-dimensional Mach 2.4 (nominal) nozzle and a 15.2 × 22.9 cm (6 × 9 inch) test section. The cascade wind tunnel was typically operated at a total pressure of 400 kPa and a total temperature of 285 K, for a Reynold's number of approximately 4.4×10^5 per cm. Storage tank capacity limited run time to approximately 10 seconds. The air was dried and filtered to reduce the level of particulates in the flow. Upstream of the nozzle, the settling chamber was equipped with flow straighteners and screens to reduce large scale turbulence. The Mach number in the settling chamber was approximately 0.11.

Mach number at the face of the cascade was measured as 2.36 ± 0.05. The freestream turbulence intensity has been found by Bowersox[9] to be approximately 1%. Details of the flowfield two-dimensionality and repeatability are detailed in Appendix B.

2.2 *Cascade*

The cascade blade shapes were derrived from the NASA Lewis baseline STFF rotor at mid-span. The cascade consisted of six full scale blades with chord length, c, of 100.3 mm, spacing, s, of 30.2 mm, and width of 152 mm as shown in Figure 2. The solidity, σ, of the blades was 3.32. Maximum blade thickness was 5.8 mm. The blade shape is detailed in Table 2.

The cascade was mounted in a circular door that could be rotated to obtain any desired inflow angle, β_1, as shown in Figure 3. β_1 is defined as the angle of the flow to the axial direction (perpendicular to the cascade). "Design incidence", $i = 0°$, is defined as $\beta_1 = 37°$. At design, the flow is approximately parallel to the blade suction surface at the leading edge. Markings on the circular door allowed the incidence angle to be set within ±0.5°. All measurements downstream of the cascade are referred to an x-y-z coordinate system in which the z-direction is parallel to the blade trailing edge, the y-direction is parallel to the cascade, and the x-coordinate is in the axial direction. The origin of the coordinate system is at mid-span of the trailing edge of the third blade from the bottom of the cascade as shown in Figure 3. In order to obtain shadowgraphs of the blade passage, the blades were mounted in a plexiglas window. For LDV measurements, a second set of doors was used with a 90 mm diameter schlieren quality glass window mounted to provide access to the blade trailing edge region as shown in Figure 4.

No endwall suction is applied in the test section. Due to the high Mach number in the cascade, the characteristics are fairly shallow and any disturbance caused by thickening of the endwall boundary layer only propagates a limited distance towards the center of the blade passage. As a consequence, the axial velocity density ratio (AVDR), $(\rho u)_2/(\rho u)_1$, is 1, and the flow at the center of the passage is two-dimensional. The contrast to lower speed cascades, in which the

thickening of the endwall boundary layer pushes the flow towards the center of the passage is illustrated in Figure 5. In subsonic axial cascades, the AVDR is typically greater than 1, and the flow is three-dimensional at mid-span. Oil streaks on the blade surfaces and downstream pitot measurements verified the two-dimensionality of the STFF cascade flow at mid-span. Additional documentation of the two-dimensionality of the flow can be found in Appendix B.

It should be noted that there are some features of this cascade which are quite different from blading which is supersonic relative to the blades but subsonic in the axial direction. The first of these is that shocks coming off of the leading edge will be contained within the blade passage. Since no waves propagate in front of the blades, no "unique incidence" condition exists for supersonic axial blading. Also, since the flow is supersonic axial at the exit of the cascade, the static pressure at the exit of the cascade is prescribed by the inlet conditions, and back pressure is not an independent parameter.

It should also be noted that in these blades, the flow is turned towards the axial direction, and so the passage area increases. For a supersonic flow, this means that the Mach number increases through the blade passage and the static pressure drops. This drop in the static pressure is opposite of that in conventional fan and compressor blading, and is important in that the favorable overall pressure gradient limits boundary layer growth and helps to prevent massive boundary layer separation.

Table 2. STFF Cascade Blade Shape.

	Suction Surface		Pressure Surface	
Chord	X (mm)	Y (mm)	X (mm)	Y (mm)
-0.2000	-59.439	-34.768	-60.264	-33.569
-0.1000	-50.790	-29.157	-51.171	-28.641
0.0000	-42.476	-23.170	-42.200	-23.612
0.0500	-38.445	-20.036	-37.760	-21.059
0.1000	-34.498	-16.807	-33.350	-18.481
0.1500	-30.561	-13.561	-28.956	-15.928
0.2000	-26.573	-10.373	-24.567	-13.429
0.2500	-22.479	-7.305	-20.178	-10.978
0.3000	-18.255	-4.404	-15.781	-8.669
0.3500	-13.886	-1.712	-11.367	-6.434
0.4000	-9.380	0.749	-6.924	-4.308
0.4500	-4.752	2.969	-2.441	- 2.299
0.5000	-0.023	4.950	2.090	-0.414
0.5500	4.808	6.640	6.647	1.412
0.6000	9.708	8.052	11.245	3.180
0.6500	14.648	9.243	15.888	4.872
0.7000	19.604	10.264	20.579	6.472
0.7500	24.562	11.171	25.314	7.978
0.8000	29.510	12.007	30.089	9.393
0.8500	34.445	12.817	34.889	10.729
0.9000	39.373	13.630	39.708	11.996
0.9500	44.287	14.455	44.539	13.193
1.0000	49.195	15.293	49.380	14.321
1.1000	58.986	17.008	59.093	16.370
1.2000	68.748	18.773	68.847	18.146

Elliptic Ends

	L.E.	T.E.
Center - X (mm)	-42.314	49.261
Center - Y (mm)	-23.371	14.801
Major Axis Slope	32.21°	10.84°
Semi-major Axis (mm)	0.394	0.744
Semi-minor Axis (mm)	0.264	0.495

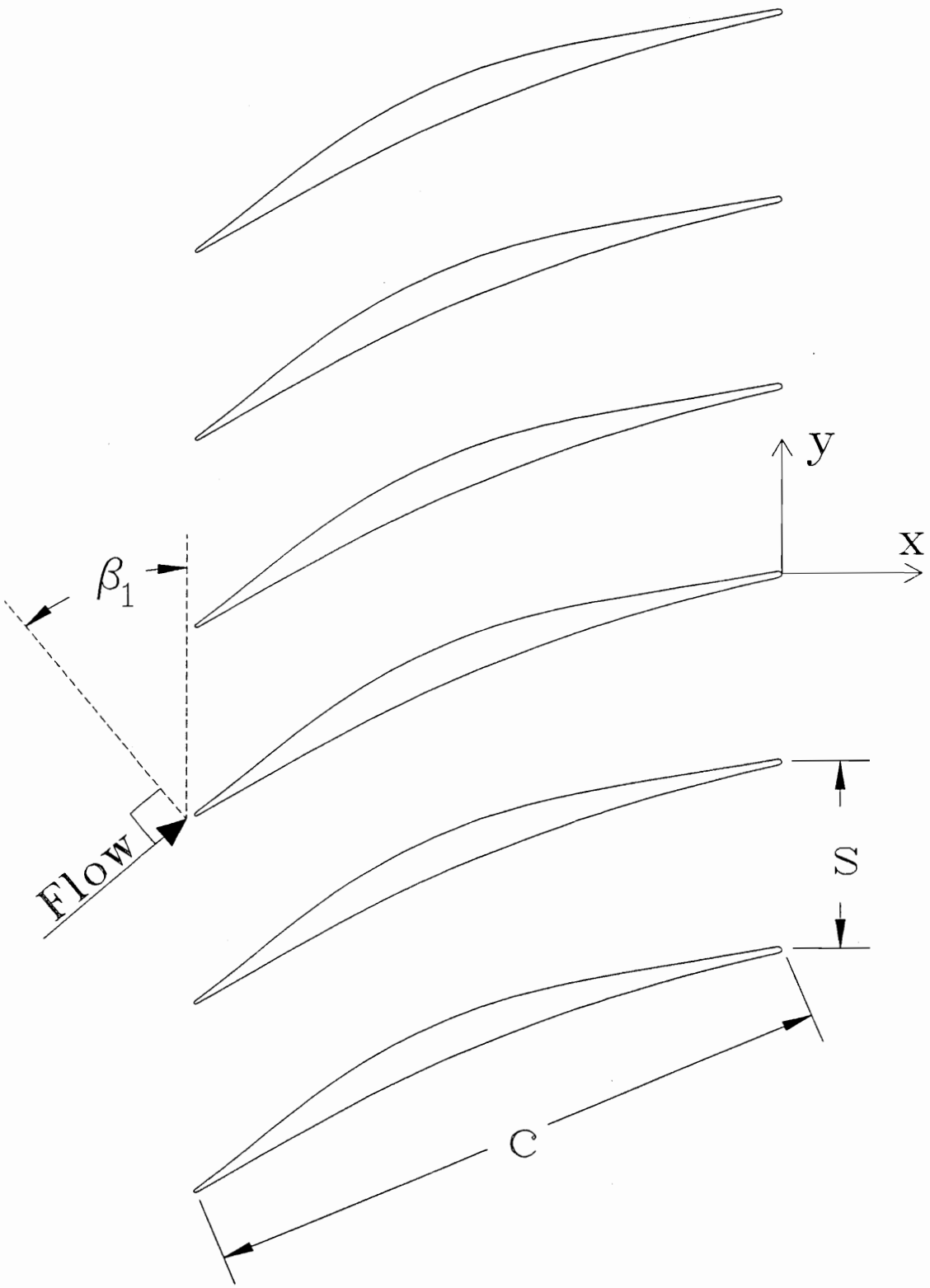

Figure 2. STFF Cascade

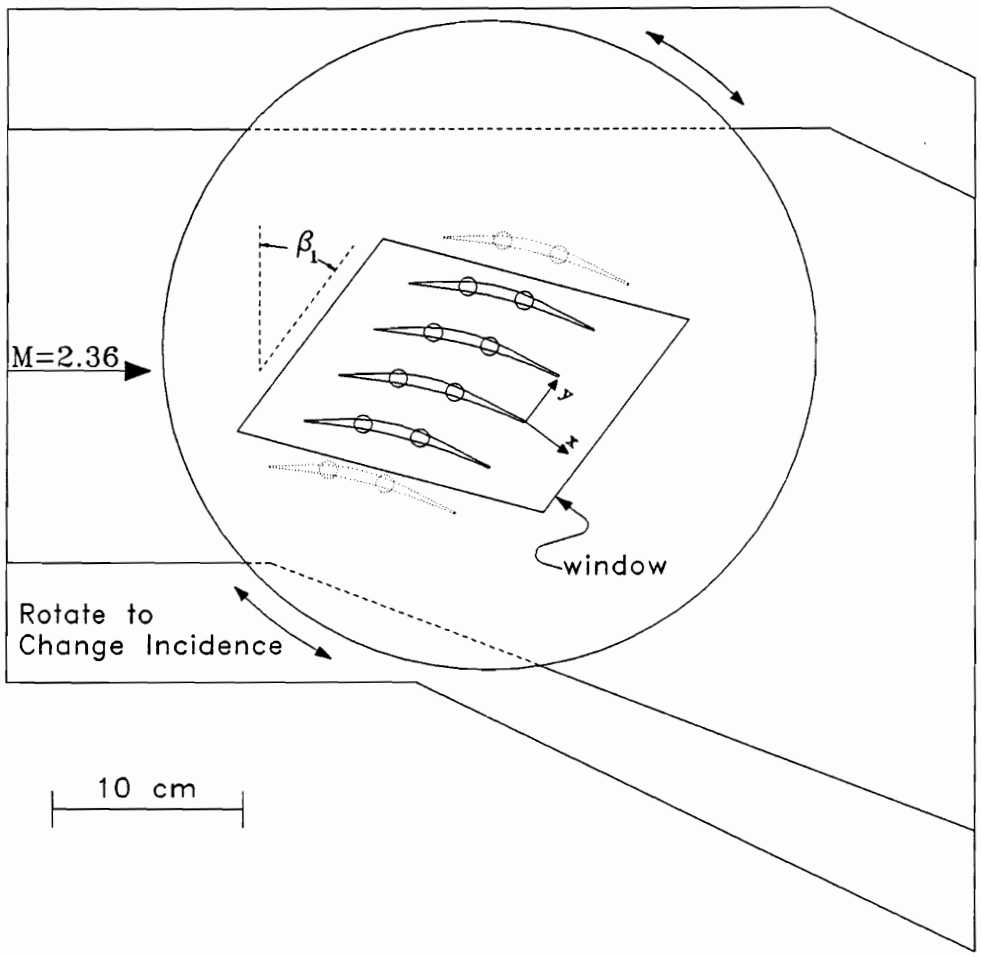

Figure 3. Cascade Test Section

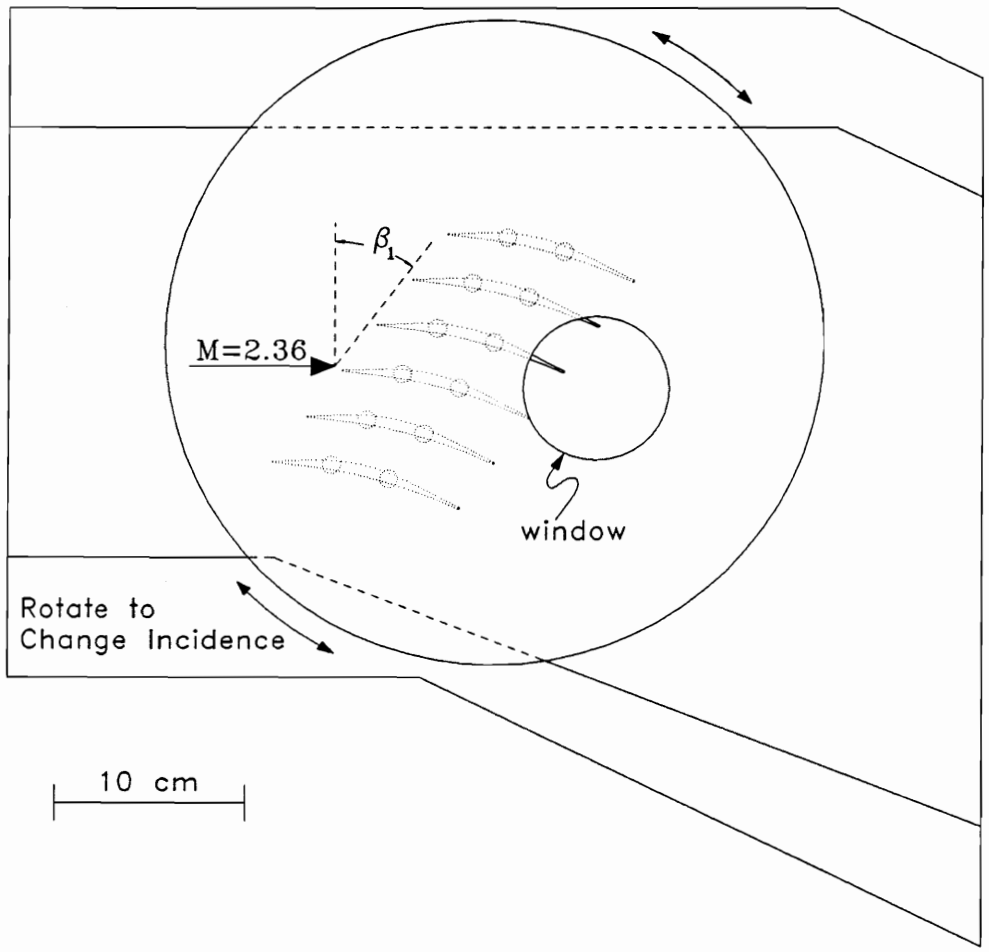

Figure 4. Glass Window For LDV Measurements

Subsonic Axial Cascade
Axial Velocity Density Ratio (AVDR) > 1

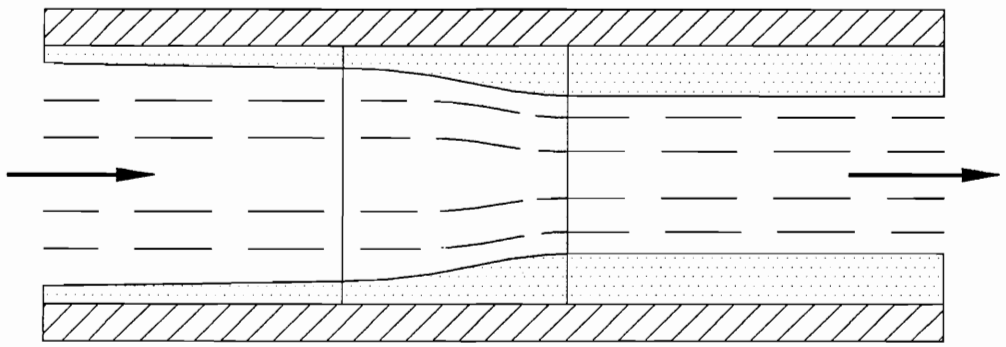

Supersonic Through-Flow Cascade
AVDR = 1

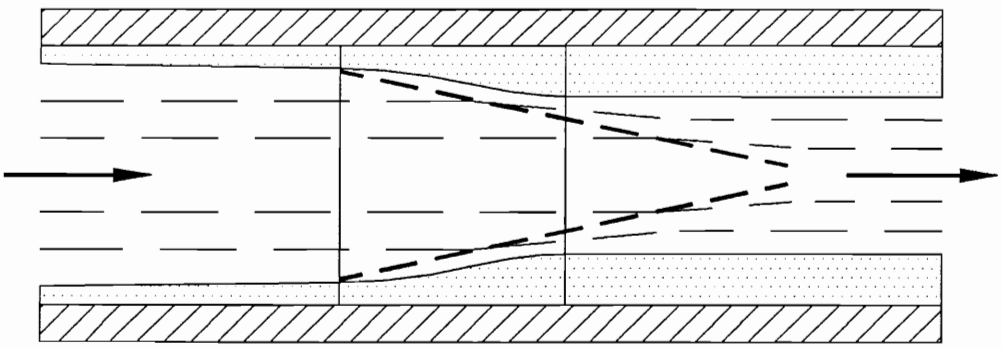

Figure 5. The Endwall Boundary Layer

Chapter 3

Instrumentation

The supersonic through-flow fan blade cascade was examined using four different sets of instrumentation: the spark shadowgraph system, the instrumented blades, the Pitot/static probe, and the 2-D laser Doppler velocimeter (LDV) system. In this section a description of each of these measurement systems will be presented along with a description of the kinds of data which can be obtained with these systems. The actual measurements made with these systems will be presented in the following chapter.

3.1 Shadowgraphs

The VPI supersonic cascade wind tunnel is equipped with a spark shadowgraph system. The STFF cascade was mounted in doors with plexiglas windows which provided optical access to the entire blade passage. The plexiglas windows were not of sufficient quality to allow the use of schlieren photography. The spark shadowgraphs revealed the shock structure in the STFF cascade along with the presence of any separated regions in the boundary layer. These "snapshots" of the flowfield were invaluable in interpreting all other measurements.

3.2 *Instrumented Blades*

The STFF cascade could be equipped with a pair of blades instrumented with static pressure taps. The blades were placed in the cascade in adjacent positions with the upper blade measuring the static pressure on the pressure surface and the lower blade measuring the static pressure on the suction surface. The pressure taps were machined from the surface opposite that being measured so that the blade passage being examined would be undisturbed by the presence of the pressure taps. Sixteen pressure taps were placed on each blade from $x/c = 0.038$ to $x/c = 0.962$. The locations of the pressure taps are listed in Table 3.

Pressures were measured with a PSI systems model 780B scanning pressure system. Simultaneously, the total pressure in the settling chamber was measured with a strain gauge type pressure transducer. All pressures were digitized and recorded. Blade static pressure measurements are reported here normalized by the settling chamber total pressure.

The instrumented blades provided information on the pressure gradients acting on the boundary layers, the location of shock impingement on the blades, the strength of those shocks, and the extent of the shock/boundary layer interaction. The surface pressure measurements are important in understanding the growth of the boundary layers and the generation of viscous losses.

3.3 *Pitot/Static Probe*

Early measurements, reported in Bowersox[9], were made with a Pitot/cone-static probe which had poor frequency response and which could make accurate cone static measurements only

Table 3. Static Pressure Tap Location, Instrumented Blades

Tap	Percent Chord	
	Suction Surface	Pressure Surface
1	3.95	3.75
2	7.62	6.89
3	13.75	10.73
4	20.28	13.16
5	26.91	19.59
6	33.34	26.13
7	39.62	32.33
8	45.97	39.06
9	52.18	44.99
10	58.41	51.22
11	64.51	60.63
12	70.53	69.87
13	79.80	79.47
14	89.19	89.04
15	94.43	93.04
16	96.71	96.71

at relatively small pitch angles. As a result of these limitations, the Pitot/cone-static probe could measure only a fraction of a blade passage during a single blow down run and regions of the downstream flow were sometimes measured as having a total pressure exceeding the upstream total pressure. A search of the literature on probes capable of measuring the Mach number and total pressure in this cascade revealed none which showed any promise of improved performance. For this reason, a new probe, the Pitot/static probe, was designed and built to provide an improved measurement of Mach number and total temperature in the STFF cascade.

The Pitot/static probe is illustrated in Figure 6. The Pitot/static probe is a rake type probe

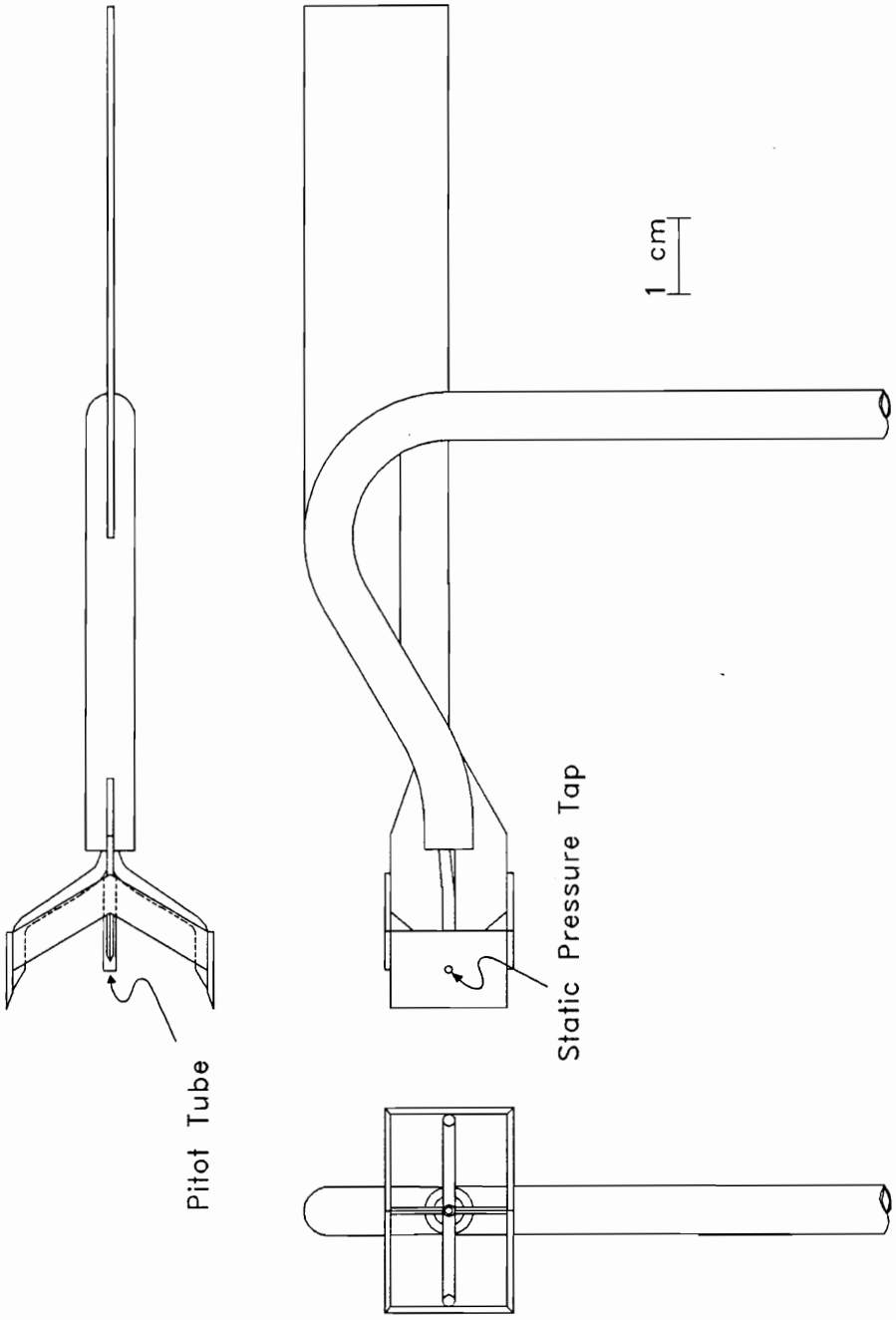

Figure 6. Pitot/Static Probe

with three pressure taps. The centrally mounted tube measures a Pitot pressure, which for a supersonic flow is the total pressure behind a normal shock. Two parallel plates are located 13 mm to either side of the centrally mounted Pitot tube. These plates are located far apart so that the plates will not interfere with the flow to the Pitot tube at Mach numbers above 1.4. On each plate is a pressure tap to measure the static pressure. The pressure measurement of each side tap is very sensitive to the angle of the plate to the flow. However, when the pressure measurements on the two parallel plates are averaged, an accurate static pressure measurement is obtained which is relatively insensitive to the yaw of the probe. The nature of the probe also makes it relatively insensitive to pitch. Pressure taps are all 1.0 mm in diameter, providing good frequency response and allowing measurement of a full blade passage in a single blow-down run. Since the two static pressure measurements are 26 mm apart, this probe is only suited to measurements in two-dimensional flowfields.

The three measurements were made independently with three strain gauge type pressure transducers. Simultaneously, a measurement of the settling chamber total pressure, p_{t0}, was made. The output from the pressure transducers was digitized and recorded.

From the Pitot and static pressure measurements, the Mach number, M, total pressure, p_t, and mass flux, ρu, can be calculated in the following manner. First, the Mach number is calculated from the ratio of the Pitot pressure, p_p, to the static pressure, p.

$$\left(\frac{p_p}{p}\right)^{\frac{\gamma-1}{\gamma}} = \left(\frac{\gamma+1}{2}\right)^{\frac{\gamma+1}{\gamma}} M^2 \left(\gamma M^2 - \frac{\gamma-1}{2}\right)^{-\frac{1}{\gamma}} \tag{3.1}$$

Since this expression is not explicit in M, the following curve fit to this relation was used.

$$M = 0.8889857\psi^{0.45676} + 0.020721\psi + 0.0917443 \tag{3.2}$$

$$\psi = \frac{p_p}{p} - 0.892929$$

The total pressure can be calculated from:

$$\frac{p_{t2}}{p_{t1}} = \frac{p}{p_{t1}}\left[1 + \frac{\gamma-1}{2}M^2\right]^{\frac{\gamma}{\gamma-1}} \tag{3.3}$$

and the mass flux from:

$$\frac{(\rho u)_2}{(\rho u)_1} = \frac{p_{t2}}{p_{t1}}\frac{M_2}{M_1}\left[\frac{1 + \frac{\gamma-1}{2}M_1^2}{1 + \frac{\gamma-1}{2}M_2^2}\right]^{\frac{\gamma+1}{2(\gamma-1)}} \tag{3.4}$$

Equation 3.4 is calculated assuming that flow through the nozzle is isentropic.

The profiles of these measurements show shock location and the location, magnitude and extent of the wake. The performance of the cascade can be quantified by integrating these profiles to obtain the mass-averaged and mixed-out total pressure losses for the cascade.

3.4 2-D Laser Doppler Velocimeter

A two component TSI Laser Doppler Velocimeter (LDV) was used to measure the velocity of particles injected into the flow. The system was optimized for use in the supersonic through-flow fan blade cascade. The light source was a 4 Watt Argon-Ion laser with an etalon tuned for single longitudinal mode operation in both the green (514.5 nm) and blue (488 nm). Total power output with the etalon was 2 Watts. The system was set to measure velocity components at plus and minus 45° to the mean flow. Beam spacing was 9 mm prior to a 3.75× beam expander. A 480 mm lens focused the beams on the measurement volume, giving a fringe spacing of approximately 7 μm. One of each of the blue and green beams was frequency shifted by 40 Mhz, so that the fringes would move in the direction of the flow, and angular bias would be minimized. Light was collected in direct forward scatter, and counters with 1 ns resolution clocks were used to measure the time for eight fringe crossings. A 10 μs coincidence window was employed to ensure that green and blue velocity measurements were correlated. This was the minimum coincidence window available with the counters used. No frequency downmixing was employed. At each measurement position, 1024 data points were taken, and the mean velocity of the flow was taken as the arithmetic mean of the 1024 measurements. The LDV system was mounted on a TSI three axis traversing mechanism and could be positioned to an accuracy of 0.05 mm. A thermocouple in the wind tunnel settling chamber measured the total temperature of the flow.

A suspension of 0.6 μm polystyrene latex spheres (PSL) in ethanol was injected directly into the tunnel approximately 3 m upstream of the nozzle throat. The 0.6 μm PSL was chosen to maximize scattered light while minimizing particle lag. The 0.6 μm particles will follow the

flow closely through most of the blade passage, and will only lag the flow significantly in very small regions behind the cascade shocks. The analysis of the particle lag for the STFF cascade is detailed in Appendix C.

The seeder, shown in Figure 7, was similar in design to that described by Seegmiller[10]. The seeder consisted of a 9.5 mm (3/8 in) pipe with a linear array of five 1.8 mm (0.070 in) air holes spaced 9.5 mm (3/8 in) apart. Attached to the pipe and adjacent to the air holes were two 2.4 mm (3/32 in) tubes which carried the ethanol/PSL mixture. Adjacent to each air hole, the tubes were drilled with 0.51 mm (0.020 in) holes canted at 20° to the air flow. Thus the seeder had two liquid holes for each air hole. When high pressure air (approximately 2700 kPa) was injected through the air holes, the ethanol/PSL mixture was induced to flow due to the venturi effect. High shear at the liquid/air interface promoted the generation of small droplets which evaporated to leave monodisperse PSL particles. Using ethanol with 13×10^9 particles per ml, it was possible to inject 27×10^9 particles per second into the flow — producing a data rate in the range of 4,000 to 40,000 per second. The mass fraction of particles in the flow with this amount of seed was less than 1×10^{-6}. A concern regarding ethanol as a carrier fluid was whether the LDV system was responding to ethanol droplets which could exist due to either incomplete evaporation or renucleation. Comparison of the data rate when injecting pure ethanol into the flow relative to the case of no ethanol injection confirmed complete evaporation of the ethanol carrier. Electron microscopy revealed excellent particle size uniformity and very little agglomeration of the seeder output. Pitot/static probe measurements upstream of the cascade showed the seeder to have no measureable effect on the cascade inflow.

The LDV system was used to obtain velocity measurements downstream of the cascade. When combined with the total temperature measurement, Mach number can be obtained from

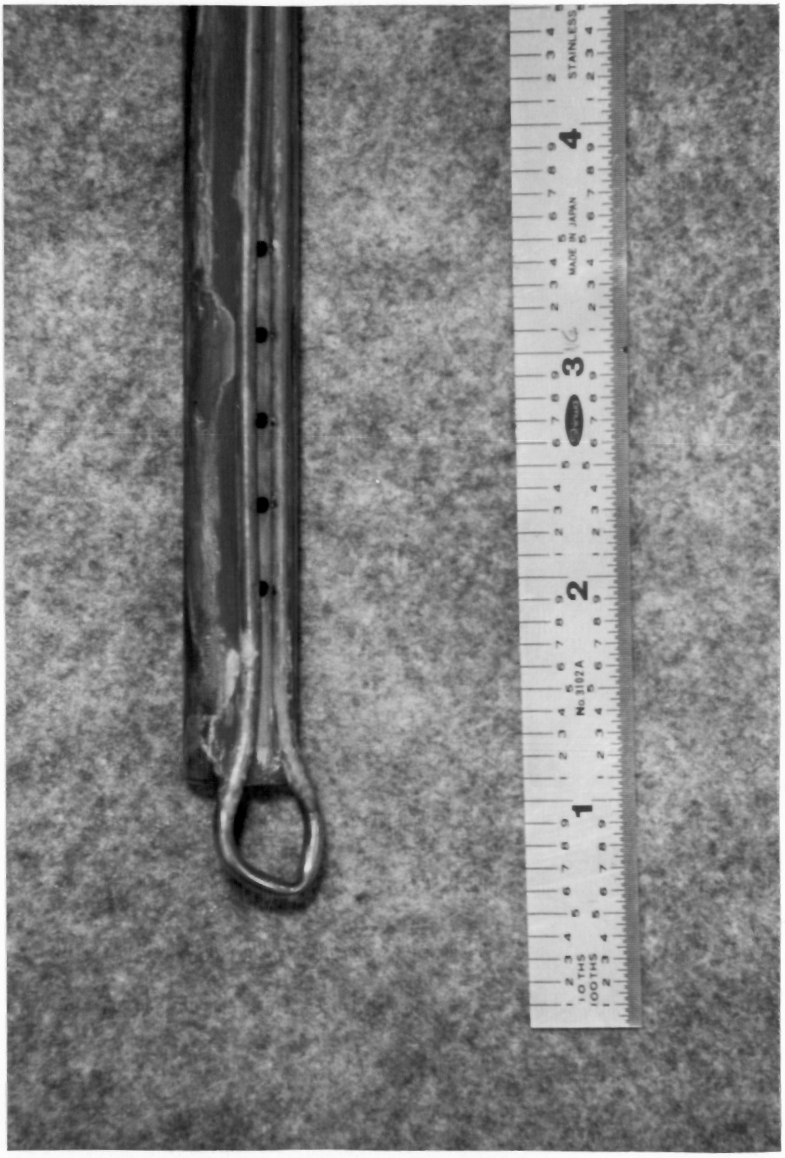

Figure 7. Seeder for LDV System

$$M = \left[\frac{\gamma R T_t}{V^2} - \frac{\gamma - 1}{2} \right]^{-1/2} \tag{3.5}$$

If a Pitot pressure measurement is available, the total and static pressures can be found as well from

$$\frac{p_{t2}}{p_{t1}} = \frac{p_{p2}}{p_{t1}} \left[\frac{(\gamma+1) M_2^2}{(\gamma-1) M_2^2 + 2} \right]^{-\frac{\gamma}{\gamma-1}} \left[\frac{\gamma + 1}{2\gamma M_2^2 - (\gamma-1)} \right]^{-\frac{1}{\gamma-1}} \tag{3.6}$$

and

$$\frac{p_2}{p_{t1}} = \frac{p_{p2}}{p_{t1}} \left(\frac{\gamma+1}{2} M_2^2 \right)^{-\frac{\gamma}{\gamma-1}} \left[\frac{\gamma + 1}{2\gamma M_2^2 - (\gamma-1)} \right]^{-\frac{1}{\gamma-1}} \tag{3.7}$$

The LDV system provided several unique capabilities that made it a valuable tool in analyzing the STFF cascade flow. Due to the high turbulence in the wake regions, there was considerable uncertainty in the accuracy of the pressure probe measurements. The LDV system is relatively insensitive to turbulence and so provided mean-flow measurements of high accuracy in the wake to resolve the uncertainty. The LDV allowed the measurement of the angle of the flow as well as the magnitude of the velocity. Turbulent quantities were also obtained with the

system — although analysis of the turbulence data is not yet complete, and presentation of this data will be in a future report. The LDV system could be used to make measurements wherever there was optical access to the blade passage. The system was much more versatile in this than the Pitot/static probe, which was unable to make measurements close to the blade trailing edge or within the blade passage.

Chapter 4

Experimental Results

Measurements were made at four different incidence angles over a range of 15°. Measurements were made at design incidence (β_1 = 37°), ±5° incidence, and -10° incidence. In the following sections of this chapter the measurements made with each type of instrumentation will be presented. In the last section of the chapter, the measurements will be used to obtain integrated loss coefficients for the cascade.

No measurements were made at +10° incidence. Shadowgraphs taken at this incidence showed the shocks coming off the leading edge of the blades propagating upstream of the cascade, indicating that the flow at the inlet plane of the cascade was axially subsonic. Measurement of the static pressure on the wind tunnel nozzle confirmed that the tunnel was operating at the design Mach number. Two-dimensional calculations at the +10° incidence case suggested that flow through the cascade should be axially supersonic at this condition. The exact reason that the cascade could not achieve supersonic axial flow at +10° incidence is not known. One hypothesis is that the thickening of the endwall boundary layers at this incidence was severe, thus allowing the downstream pressure to disturb the upstream flow. The two-dimensional calculations would then not correctly model the cascade flow, since the strong three-dimensional effects could not be captured. The flow at this condition will be investigated further.

All pressure measurements presented in this section are normalized by the total pressure just upstream of the cascade, p_{t1}. The total pressure at station 1 was measured at several spanwise and axial positions, and it was found that $p_{t1}/p_{t0} = 0.96$, where p_{t0} is the settling chamber pressure. The reasons for the losses through the supersonic nozzle are not entirely clear, although some of the measured drop in total pressure can be attributed to condensation shocks. A more thorough discussion of the upstream total pressure measurements and the losses between stations 0 and 1 can be found in Appendix B.

4.1 Shadowgraphs

Spark shadowgraphs of the cascade operating at the four measured conditions are shown in Figure 8 through Figure 11. The shock structure in the blade passage is clear in these photographs. Expansion waves and turbulent structures, however, are not easily discerned.

Figure 10 shows the flow through the cascade at design incidence, $\beta_1 = 37°$. In this photograph, the shocks coming off the leading edge can be seen to be contained within the blade passage. This indicates that the component of velocity in the axial direction (perpendicular to the cascade) is supersonic. The leading edge shock from the suction side (upper) of the leading edge intersects the pressure surface (lower) at approximately 12% chord, and generates a reflected shock. There is no indication of boundary layer separation at this shock/boundary layer interface. Visible behind the point at which this shock intersects the pressure surface is a wave which seems to emanate from the pressure surface at approximately 30% chord. For now, the existence of this wave will simply be noted. Discussion on the nature of this wave will be presented in the section on surface pressure measurements. The leading edge shock from the pressure side intersects the

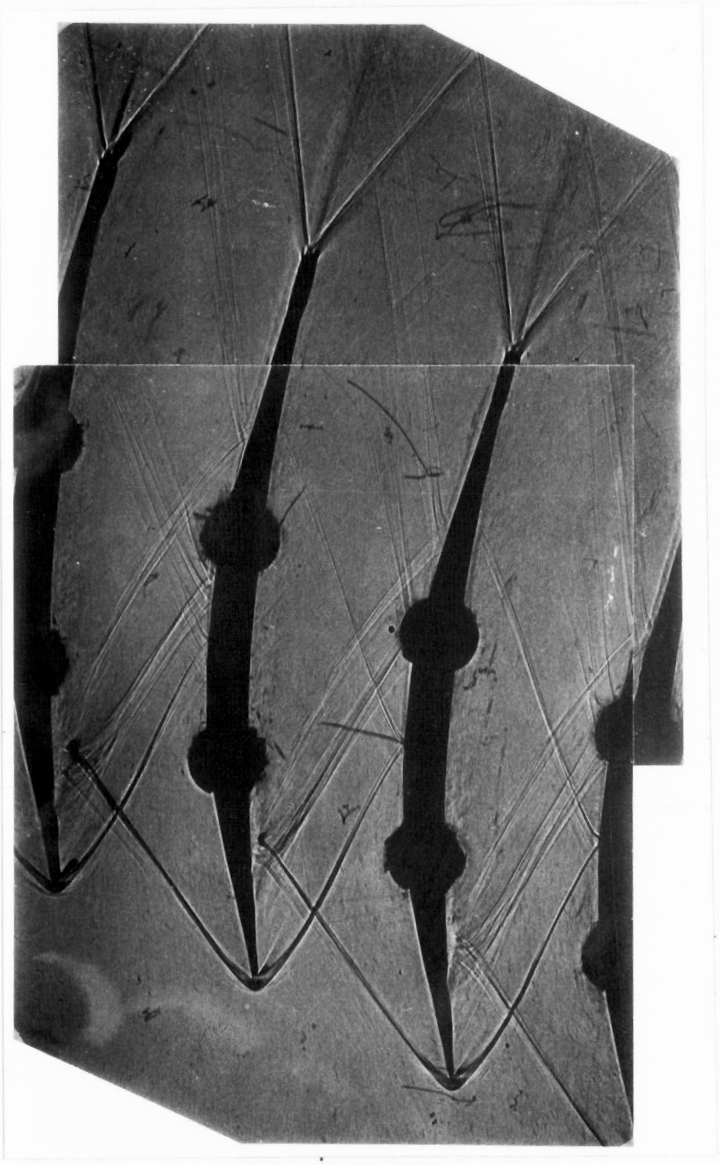

Figure 8. Cascade Shadowgraph, -10° Incidence, $\beta_1 = 27°$

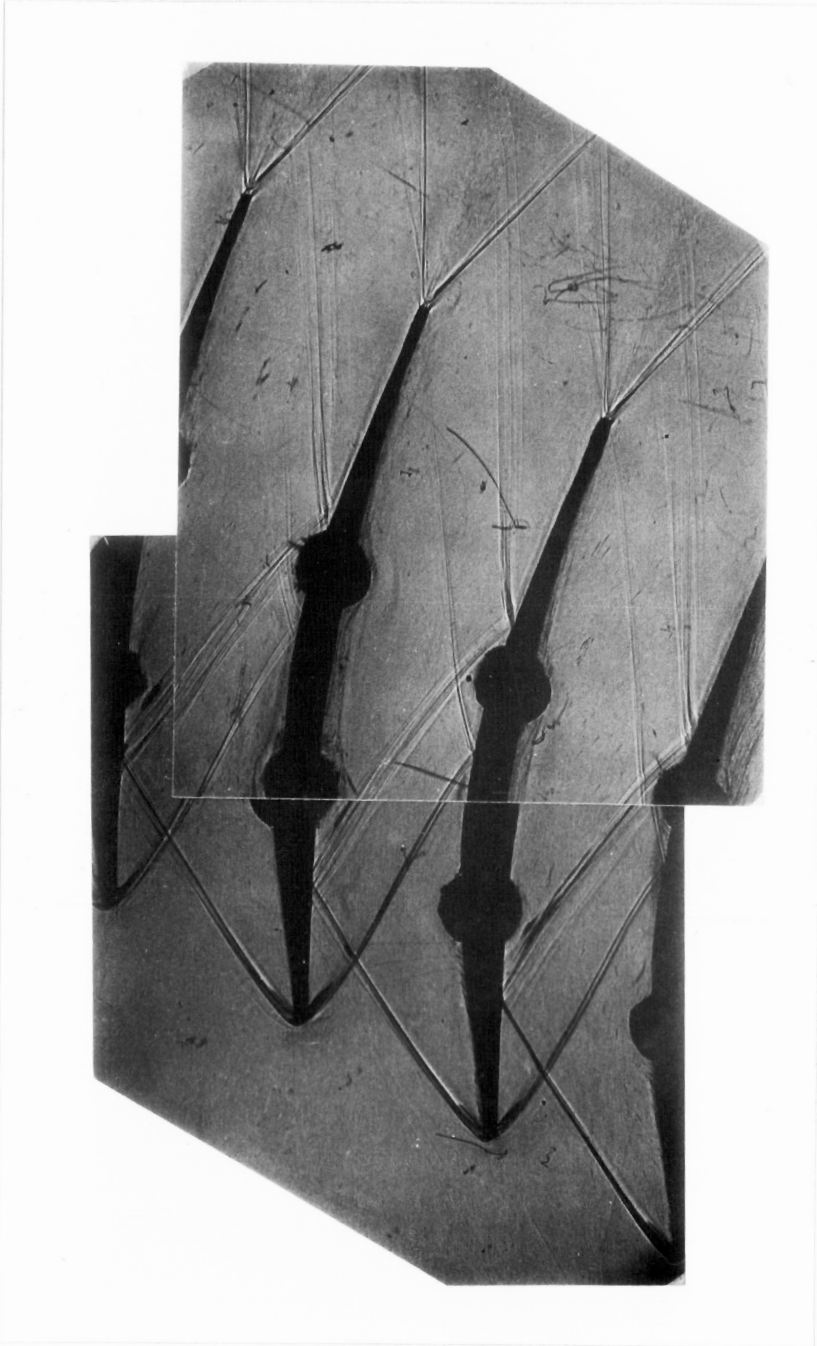

Figure 9. Cascade Shadowgraph, -5° Incidence, $\beta_1 = 32°$

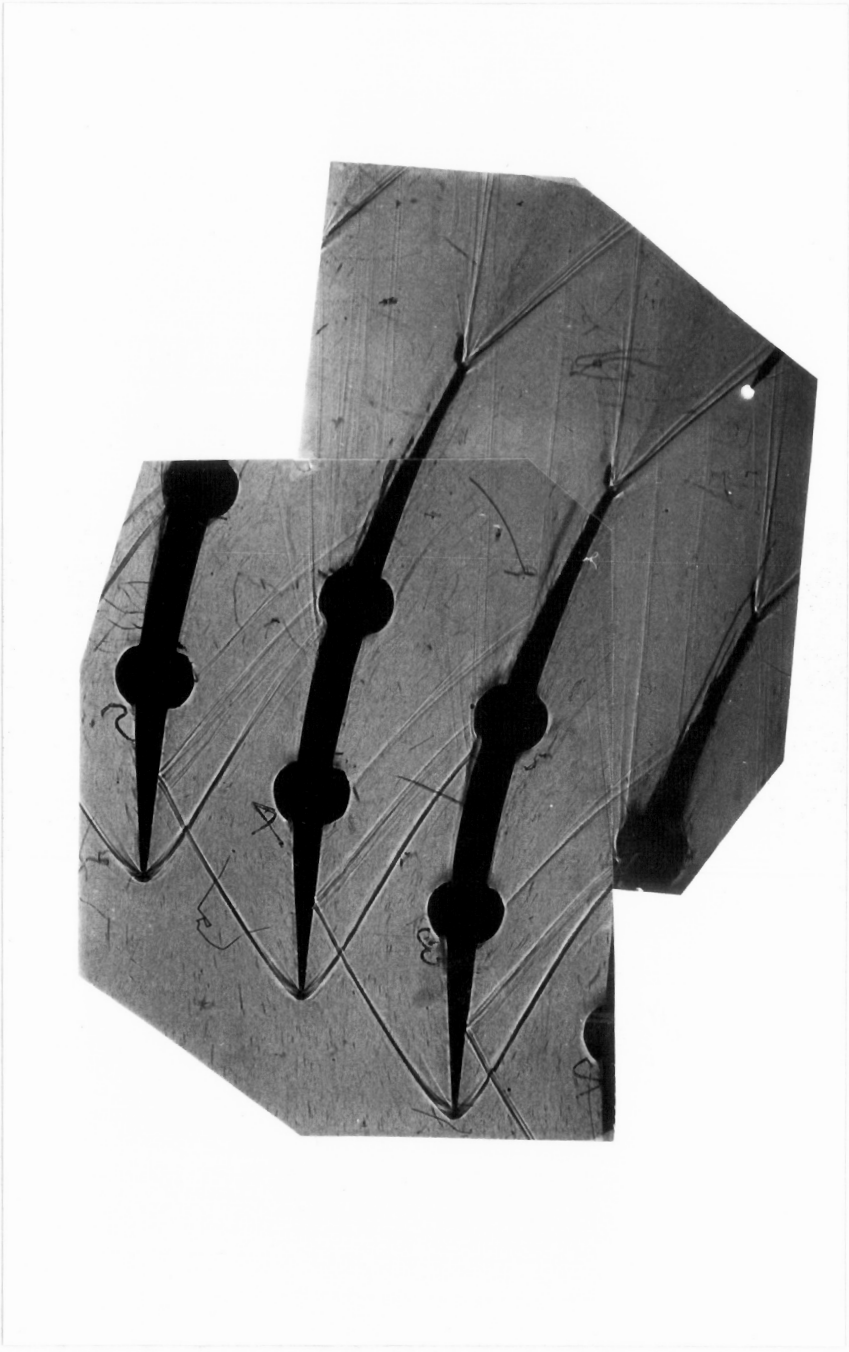

Figure 10. Cascade Shadowgraph, Design Incidence, $\beta_1 = 37°$

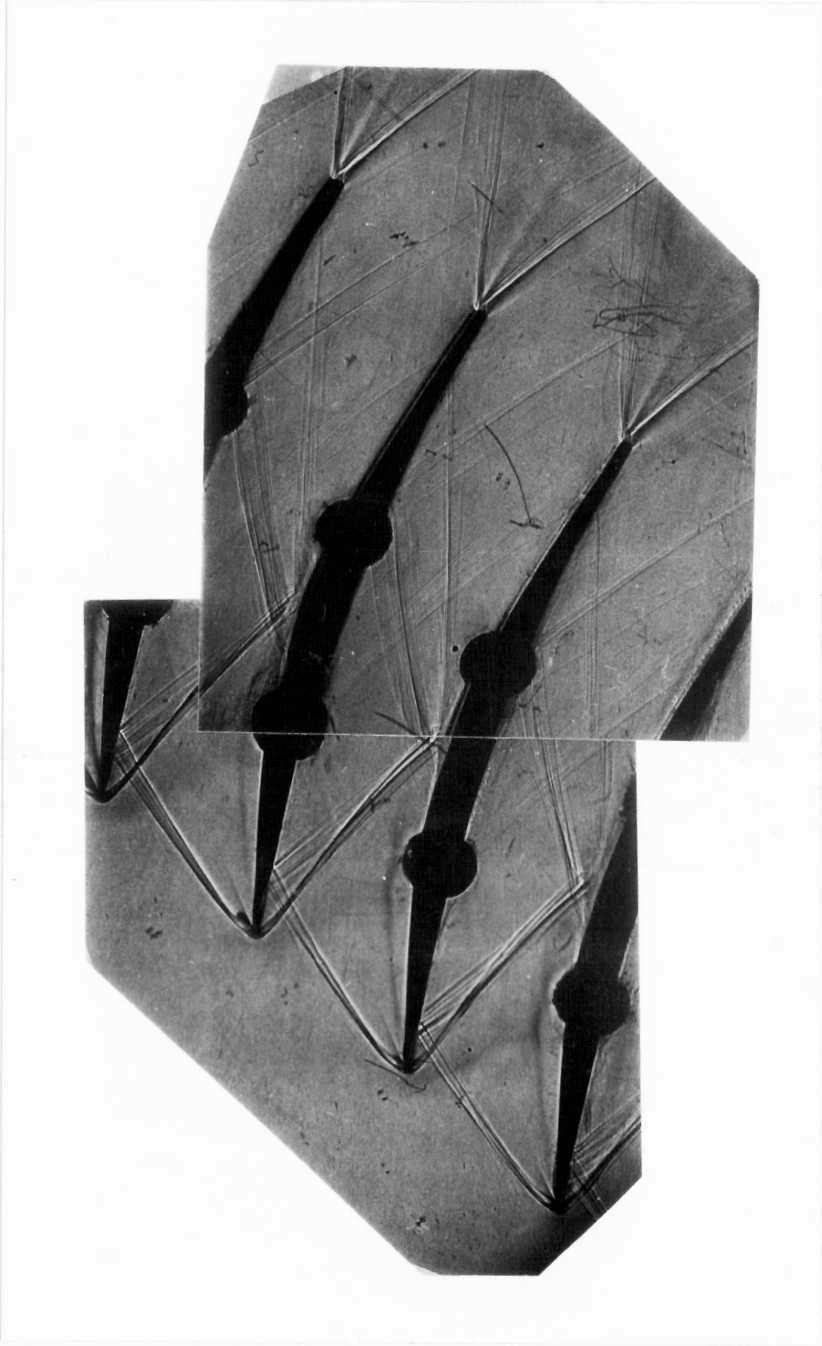

Figure 11. Cascade Shadowgraph, +5° Incidence, $\beta_1 = 42°$

suction surface at approximately 55% chord and reflects weakly. Again, there is no indication of shock induced boundary layer separation. Originating from the trailing edge are a pair of "fishtail" shocks. These shocks exist to equilibrate the flows from the suction and pressure surfaces, which arrive at the trailing edge at slightly different pressures and slightly different flow angles. The blade wake is only weakly visible in the shadowgraph, and little about its extent or structure can be inferred. Visible in the bottom right of the shadowgraph is one of the pressure probes used downstream of the cascade.

Figure 8 shows the flow through the cascade at -10° incidence. At this incidence, the shock coming off the suction side of the leading edge is much stronger than in the design case. The shock structure revealed in the shadowgraph clearly indicates a strong shock/boundary layer interaction where this shock impinges on the pressure surface, approximately 17% chord. In the photograph, compression waves can be seen to originate from the pressure surface just upstream of the impinging shock as the flow is deflected by the separation zone. These compression waves then coalesce to form a "separation shock". Just downstream of the shock impingement point, the shadowgraph shows another shock emanating from the pressure surface. This shock exists due to the flow reattaching after turning around a separation bubble. Further evidence of flow reattachment is visible on the pressure surface at approximately 73% chord, where a wave approaching the pressure surface can be seen to impinge. If the flow at this point had been separated, the flow near the blade would have been subsonic, and the wave would have bent toward the blade and disappeared as it approached the surface. All waves impinging on the suction surface can be seen to reflect weakly, without causing any separation of the suction surface boundary layer. Again, the fishtail shocks are clearly visible downstream of the blades, but the wake is only faintly visible.

Figure 9 shows the flow through the cascade at -5° incidence. At this incidence, the flow

is nearly symmetric to the leading edge wedge, and both shocks emanating from the leading edge are relatively weak. There is no evidence of boundary layer separation anywhere in the blade passage.

Figure 11 shows the flow through the cascade at +5° incidence. For this angle, the shock emanating from the pressure side of the leading edge is much stronger than in the design case. The shock structure revealed in the shadowgraph clearly indicates the presence of a separation bubble on the suction surface at approximately 50% chord where this shock wave impinges. A separation shock emanating upstream of the shock impingement point and a reattachment shock originating downstream of the impingement point are clearly visible. No other separation regions are visible in the shadowgraph. Similar to design incidence, there appears to be a set of waves emanating from the pressure surface of the blade at approximately 35% chord. Again, the existence of these waves will simply be noted here, and a discussion of the nature of these waves will be presented in the blade surface pressure measurements section.

4.2 Blade Surface Pressure

Blade static pressure measurements for the four measured incidence angles are shown in Figure 12 through Figure 15. The pressure measurements have been non-dimensionalized by the upstream total pressure, p_{t1}. The uncertainty in the pressure measurements, as detailed in Appendix A, is ±1.2% — approximately the size of the symbols on the plots. To interpret these plots, it is helpful to compare each of the plots to the corresponding shadowgraph.

Figure 12 shows the blade static pressure distribution for the case of -10° incidence. The pressure on the suction surface can be seen to first rise slightly as the flow is compressed through

the slight concavity of the suction surface at the leading edge. The pressure then drops as the flow is turned and accelerated. Between 45% and 60% chord, two shocks intersect the suction side and raise the pressure. The first of these shocks comes from the pressure side of the leading edge. The second is the separation shock from the pressure surface. The flow then expands once again, reaching a minimum pressure at approximately 70% chord, before the pressure increases due to the impingement of the reattachment shock from the pressure surface. Over the last 20% of the suction surface the static pressure rises slightly under the influence of compression waves originating from the pressure surface.

On the pressure surface of the blade at -10° incidence, the measurements show the pressure rising from very near the leading edge. The pressure side of the blade, however, has very little curvature near the leading edge and has no shocks impinging on the surface until approximately 20% chord. It is apparent from these measurements that the separated zone of the boundary layer has allowed the pressure rise of the shock to extend considerably upstream of the impingement point. It is impossible to identify the downstream extent of the separation bubble influence on the pressure rise since the pressure rise due to the shock is complemented by the pressure rise due to blade concavity. The static pressure peaks at approximately 35% chord. After this point, the expansion waves emanating from the suction surface cause a monotonic drop in pressure to the trailing edge. This steady drop in pressure over the last two thirds of the pressure surface is only slightly disrupted by the shock impinging at 75% chord, a reflection of the leading edge shock from the suction surface, indicating that the shock is weak. The pressure on the pressure side of the blade is almost equal to that on the suction side at the trailing edge, indicating that only small adjustments in the flow should occur downstream of the cascade, and that the fishtail shocks should be weak.

Figure 13 shows the blade static pressure distribution for the case of -5° incidence. The

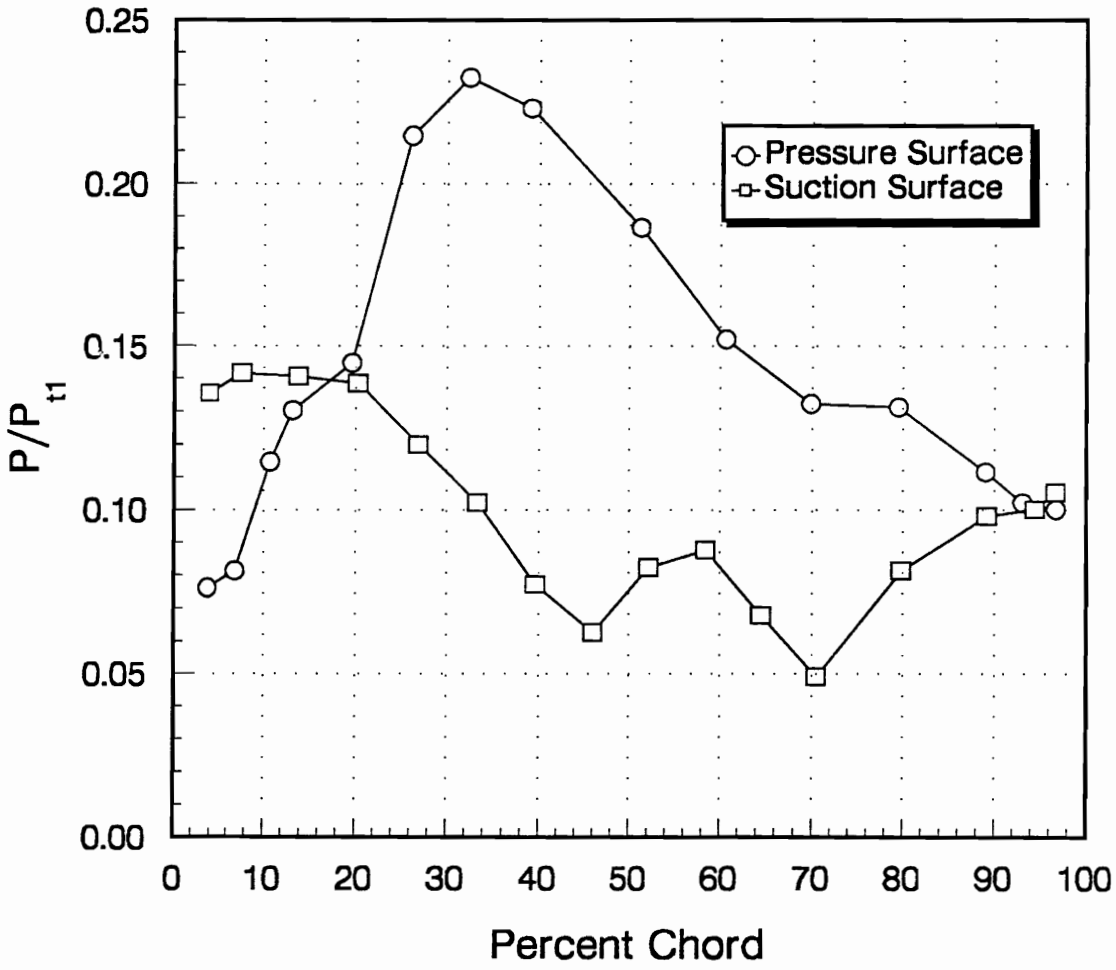

Figure 12. Blade Surface Pressure, -10° Incidence

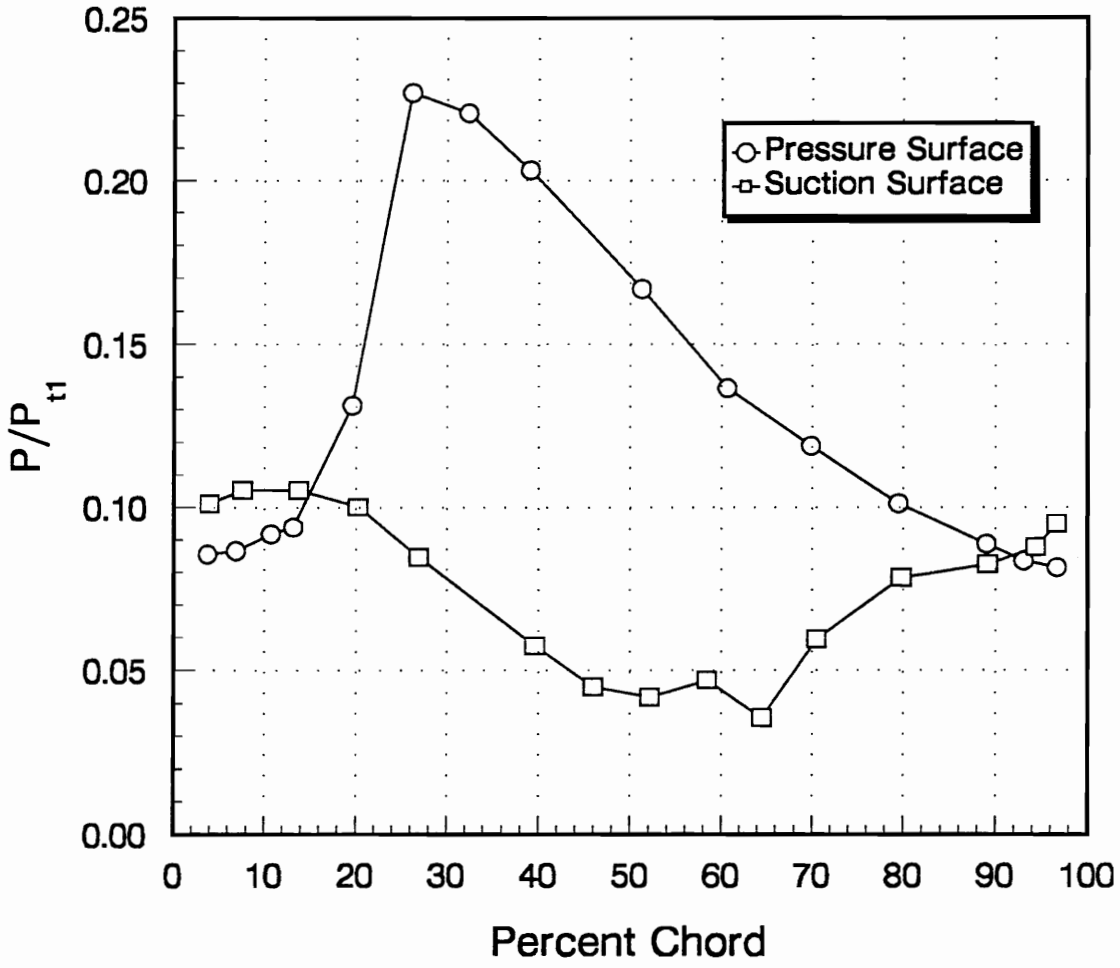

Figure 13. Blade Surface Pressure, -5° Incidence

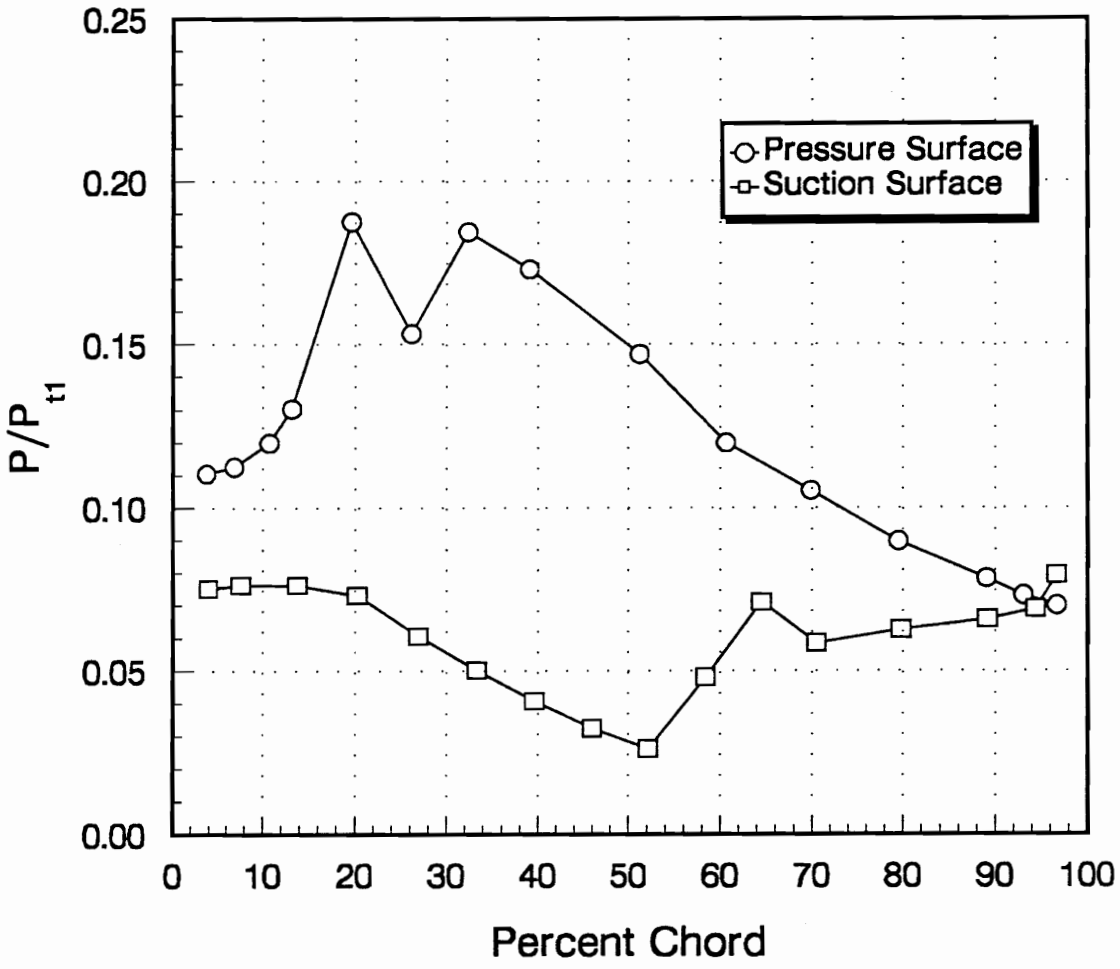

Figure 14. Blade Surface Pressure, Design Incidence

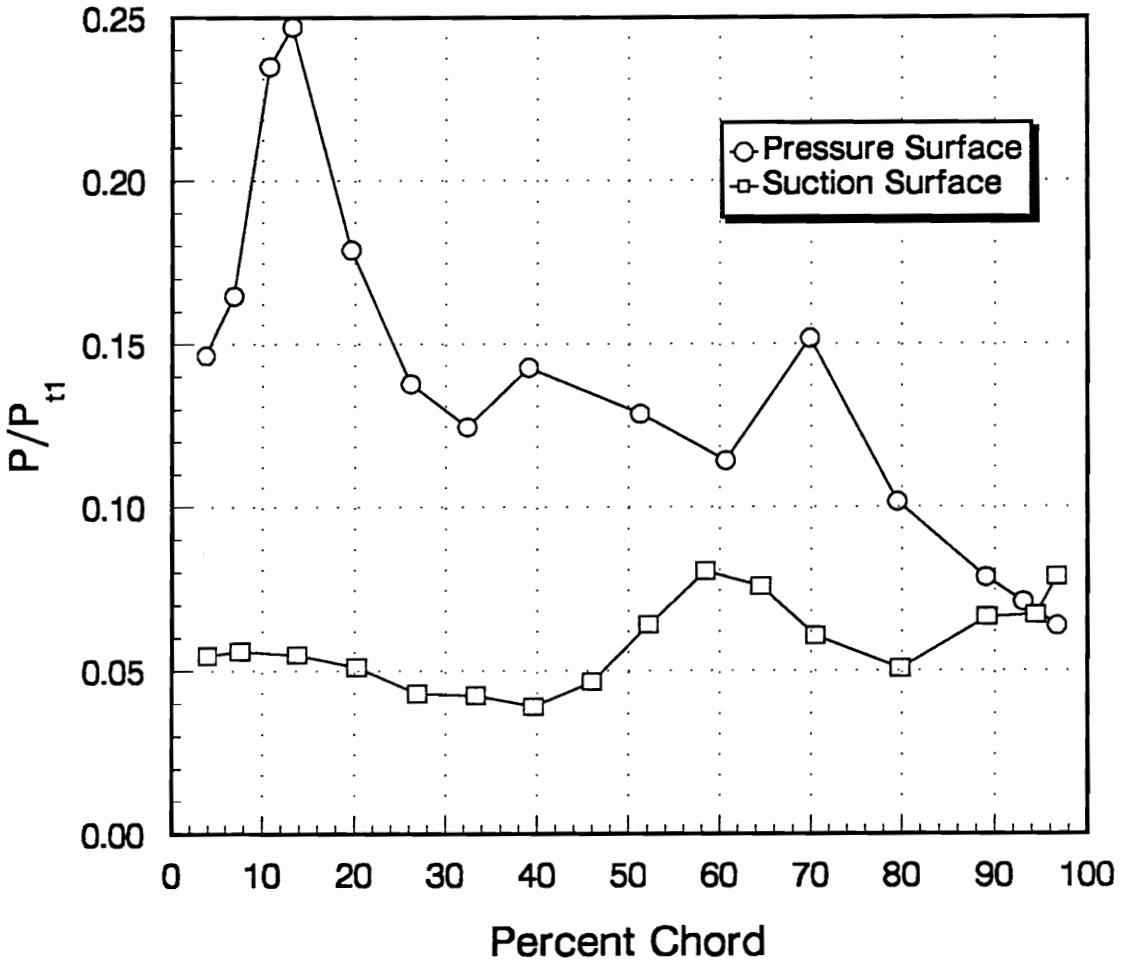

Figure 15. Blade Surface Pressure, +5° Incidence

pressure on the suction surface initially rises slightly as the flow is compressed through the slight concavity of the suction surface at the leading edge. After this initial rise, the static pressure decreases monotonically until approximately 50% chord, where the pressure side leading edge shock intersects the suction surface. The pressure rise from the shock is quite small, indicating that the lower leading edge shock is weak. The leading edge shock reflected off the pressure surface intersects the suction surface at approximately 70% chord and causes the pressure to jump. Over the last 30% of the suction surface, the pressure rises gradually under the influence of compression waves emanating from the pressure surface.

On the pressure surface at -5° incidence, the measurements show the pressure increasing only slightly over the first 15% of the blade, indicating that the influence of the leading edge shock impinging on the pressure surface does not extend far upstream through the boundary layer. The impinging leading edge shock causes a sharp jump in the pressure between 15 and 25% chord. Beyond this shock, the pressure drops steadily towards the trailing edge under the influence of expansion waves originating from the suction surface. This steady drop in pressure is in agreement with the shadowgraph of the flow, which shows no shock waves intersecting the pressure surface between 20% chord and the trailing edge. At the trailing edge, the suction side and pressure side pressures were measured to differ by only 15%.

Figure 14 shows the blade static pressure distribution for the case of design incidence. The pressure on the suction surface initially rises slightly as the flow is compressed through the slight concavity of the suction surface at the leading edge. After this initial rise, the static pressure decreases monotonically until approximately 55% chord, where the pressure side leading edge shock intersects the suction surface. After the pressure rise from this shock, and two others which closely follow, the pressure over the last 30% of the suction surface is nearly constant, rising slightly towards the trailing edge.

Measurements of the pressure surface static pressure at design incidence show the pressure increasing slowly over the first 10% of the blade, and then sharply around 15% chord where a shock from the leading edge intersects the pressure surface. After the sharp rise in pressure from this shock, the surface pressure drops and then rises again. On the shadowgraph of the flow at design incidence, this second pressure rise can be seen to correspond to a wave which originates from the pressure surface at 30% chord. The origin of this wave is uncertain. The shadowgraph shows no wave impinging upon the pressure surface at this point to cause a reflected wave, and there is no inflection on the pressure surface to generate a shock wave. It is surmised that compression waves originating from the concave portion of the leading edge suction surface coalesce to form a shock wave very near the pressure surface. These compression waves would not be visible in the shadowgraph until they converged. The wave emanating from the pressure surface at 30% chord would then be a shock similar to the "precompression" shocks commonly seen in supersonic relative, subsonic axial compressor blading. Past this second wave, the pressure drops steadily from 35% chord to the trailing edge. At the trailing edge, the pressure side and suction side pressures are nearly equal.

Figure 15 shows the blade static pressure distribution for the case of +5° incidence. The pressure on the suction surface initially rises slightly as the flow is compressed through the slight concavity of the suction surface at the leading edge. After this initial rise, the static pressure decreases until approximately 40% chord. At approximately 50% chord, the pressure side leading edge shock intersects the suction surface, creating a separation bubble. The pressure rise from this shock is spread out from 45% chord to 55% chord. The pressure then decreases to 80% chord before rising once again due to waves reflected from the pressure surface.

The pressure on the pressure surface rises sharply near the leading edge due to the shock impinging on the pressure surface at 9% chord. This sharp rise in pressure is followed by a steep

decrease in pressure between 15% and 30% chord. This rapid rise and fall in pressure indicates that the shock/expansion wave system generated by the rounded leading edge on the suction side does not fully merge into a single wave before meeting the pressure surface, and so the pressure surface is intersected by a strong shock followed by a rapid expansion. Following the expansion the pressure rises again, apparently under the influence of compression waves from the forward section of the suction surface coalescing at 35% chord. As was noted in the previous section, the reflection of these waves is visible in the shadowgraph. Between 35% and 65% chord, the pressure on the pressure surface drops under the influence of expansion waves generated on the suction surface. At 65% chord, the shock generated from the suction surface separation bubble impinges on the pressure surface, raising the pressure. The flow then expands from 70% chord to the trailing edge. Once again, the pressure side and suction side pressures are nearly equal at the trailing edge.

4.3 Pitot/Static Rake Profiles

The Pitot/static probe measurements give the most complete quantitative information on the cascade flowfield. Measurements were performed at a distance $0.37 \times c$ downstream of the blades at all incidence angles. At design incidence, three additional downstream locations were surveyed: x/c = 0.11, 0.24, and 0.50. At each station, measurements were made across the blade passage of the Pitot and static pressures. The Mach number and total pressure were then calculated from the measured pressures. Profiles of the downstream Pitot pressure, Mach number, and total pressure will be presented in this section as a function of downstream position at design incidence and as a function of incidence angle at the downstream position x/c = 0.37. The

complete set of measurements is presented in Appendix D. The coordinate system in which these measurements are presented is defined in Chapter 2.

Figure 16 shows the Pitot pressure profiles measured at the four downstream locations at design incidence. The uncertainty of the Pitot measurements is small, ±0.15% in the freestream and ±1.0% in the wake. In each of the four plots in Figure 16, the location and extent of the wake can be seen along with the location of the fishtail shocks. The wakes are visible as the two large dips in each of the profiles. The wake position moves in the positive y-direction in the sequence of plots since the flow at the trailing edge exits close to the metal angle of the blades, 11°. Deviation from the trailing edge metal angle is small due to the high solidity of the blades and the fact that the flow remains attached.

The fishtail shocks are indicated by the small spikes in each of the Pitot pressure profiles. At x/c = 0.11, the fishtail shocks are just inside the wake region. At x/c = 0.24, the fishtail shocks have moved towards the center of the passage, and at x/c = 0.37, the shocks cross. It should be noted that the spikes in the Pitot profiles which indicate the fishtail shocks do not mean that there are corresponding large fluctuations in the flow at those locations. The spikes in the profiles result from the shock wave disrupting the flow around the Pitot tube, and are therefore, anomalous.

Figure 17 shows the Mach Number profiles measured at the four downstream locations at design incidence. Plotted on the top profile in this figure are the uncertainty bands for the Mach number measurements, ±3.7% in the freestream and ±2.0% in the wake. In this figure it can be seen that the Mach number in the core flow downstream of the cascade is slightly greater than the inlet Mach number of 2.4, thus indicating an overall static pressure drop through the cascade. Notable in this plot is the behavior of the wake as the flow moves downstream. The width of the wake does not measurably change from x/c = 0.11 to x/c = 0.50, and the deficit of

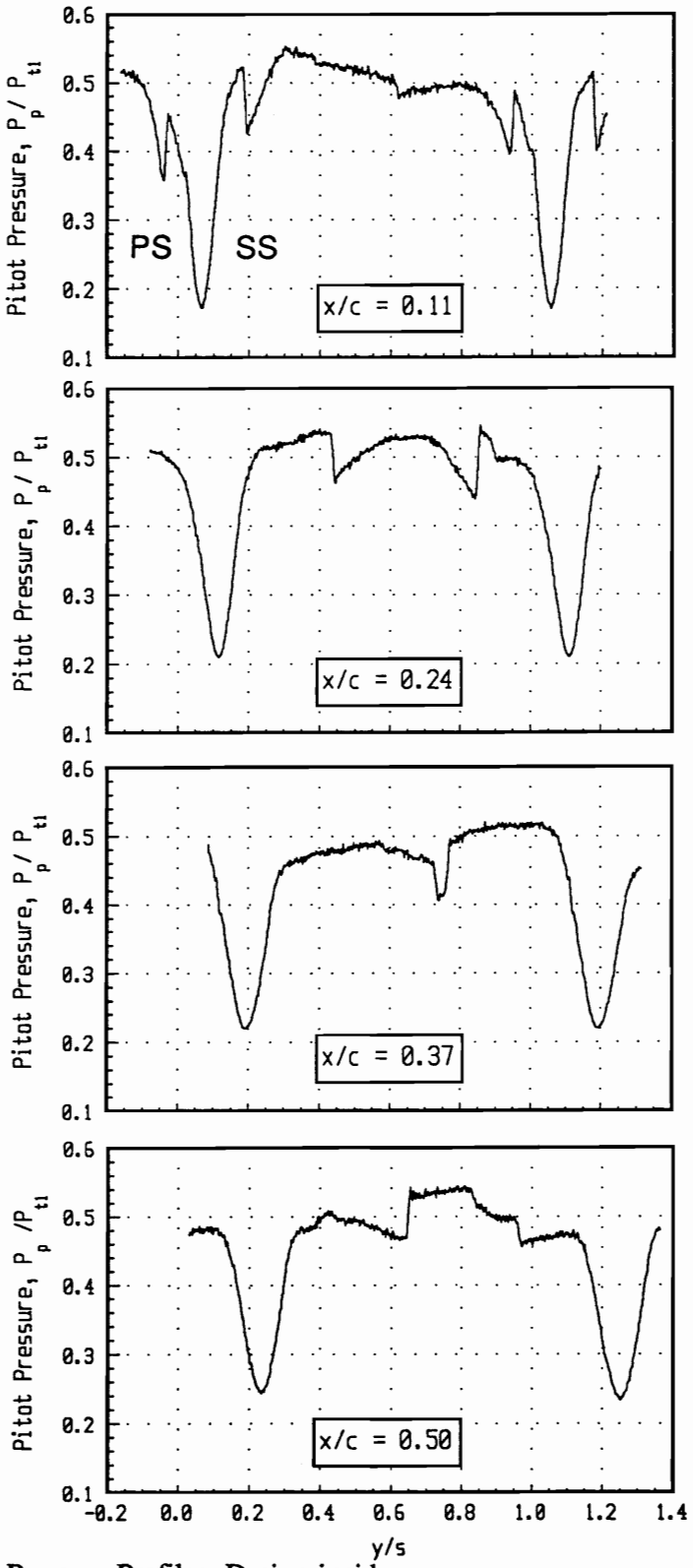

Figure 16. Pitot Pressure Profiles, Design incidence

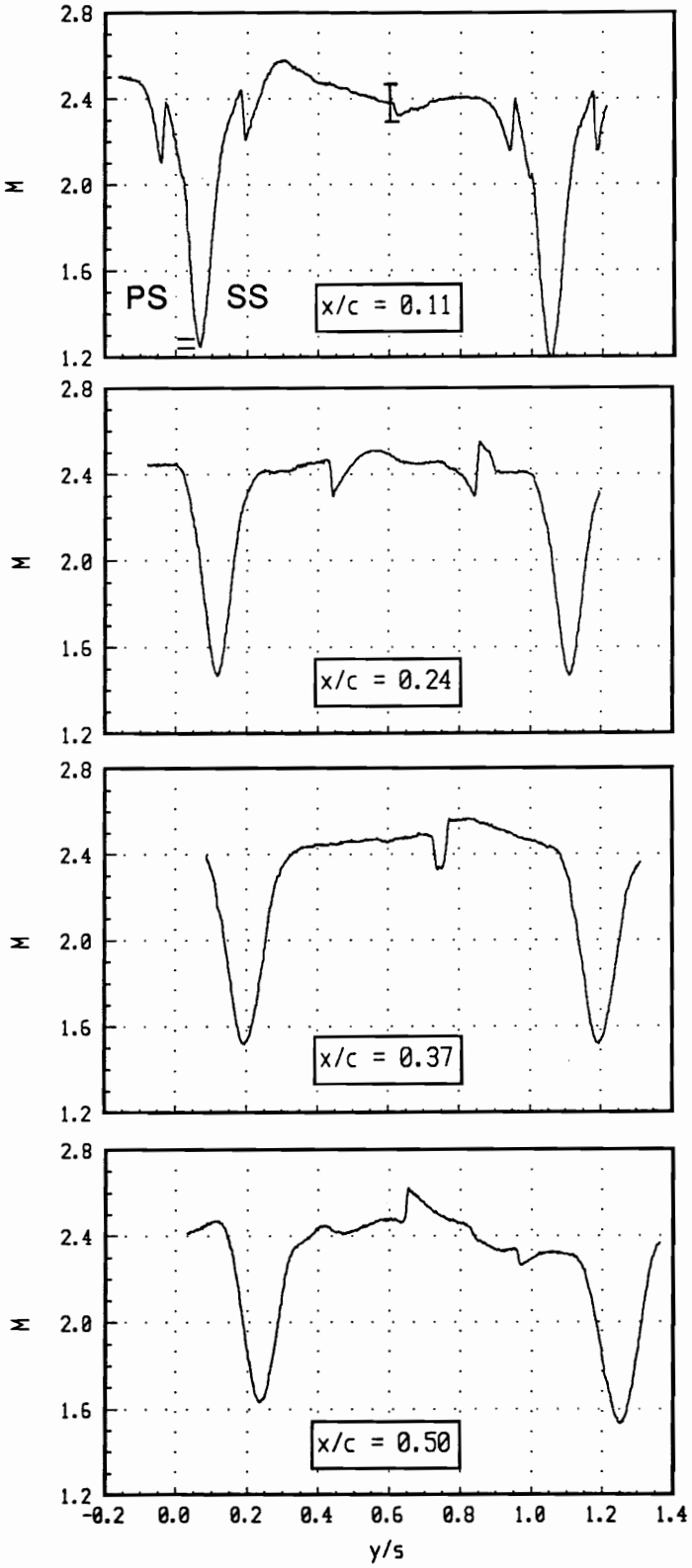

Figure 17. Mach Number Profiles, Design Incidence

Pitot pressure and Mach number compared to the core of the flow decreases only slightly. Thus there is little dissipation of the wake in the measured region, indicating that transport of momentum and energy is much more rapid in the downstream direction than in the cross-stream direction.

The profiles measured with the Pitot/static probe off design incidence are shown in Figure 18 and Figure 19. Figure 18 shows the Mach number profiles downstream of the cascade and Figure 19 shows the total pressure profiles. The uncertainty in the total pressure, ±2.3% in the wake and ±7.4% in the freestream, is plotted on the top profile in Figure 19. Regions of the core flow in Figure 19 which are measured as having p_{t2}/p_{t1} greater than 1 should not be interpreted too literally. In the center of the blade passage, particularly at design and -5° incidence, the losses are small (the total pressure ratio is close to 1) and the uncertainty in p_{t2}/p_{t1} is large. It is to be expected that the measurements will indicate some regions of the flow with p_{t2}/p_{t1} greater than 1 even though the actual total pressure ratio should always be less than 1.

Using Figure 18 and Figure 19, it is possible to get a measure of the deviation angle. All of these measurements were made at $x/c = 0.37$, and in each of these plots, the wake is at approximately $y/s = 0.19$, indicating that the deviation angle is approximately 9° for all incidence angles. The deviation angle is very close to the trailing edge metal angle of 11°. It is apparent that the very high solidity ($\sigma = 3.32$) of this cascade causes the exit flow angle to be substantially independent of the inlet flow angle.

Also notable in these figures is the shape of the wakes. For the $i = 0°$ and $i = -5°$ cases the wakes are symmetric. However, the wakes for the $i = +5°$ and the $i = -10°$ cases are skewed. At $i = +5°$ the wake is thicker on the suction side and at $i = -10°$ the wake is thicker on the pressure side. The asymmetries in the wake profiles are caused by the separation regions in the boundary layers. In the shadowgraph of Figure 8, it can be seen that at $i = -10°$ the pressure

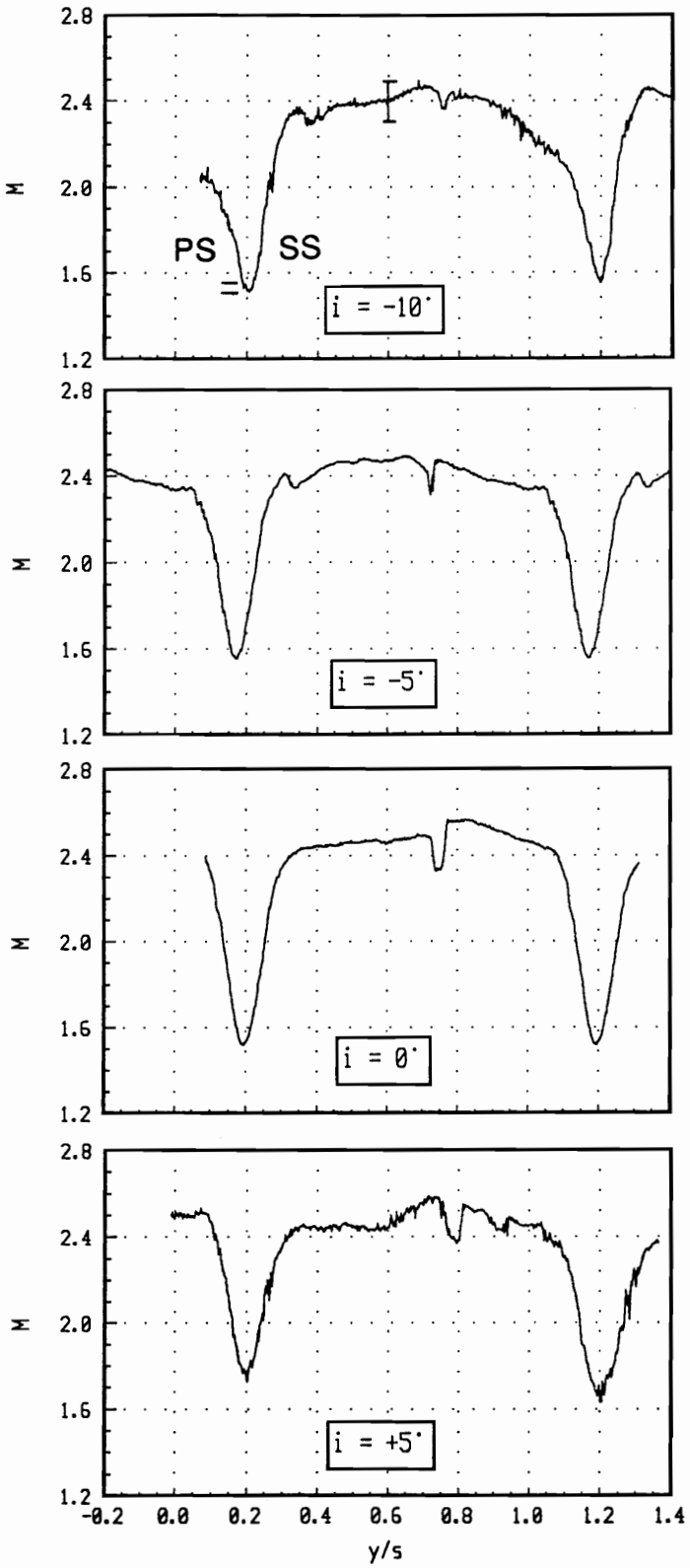

Figure 18. Mach Number Profiles, $x/c = 0.37$

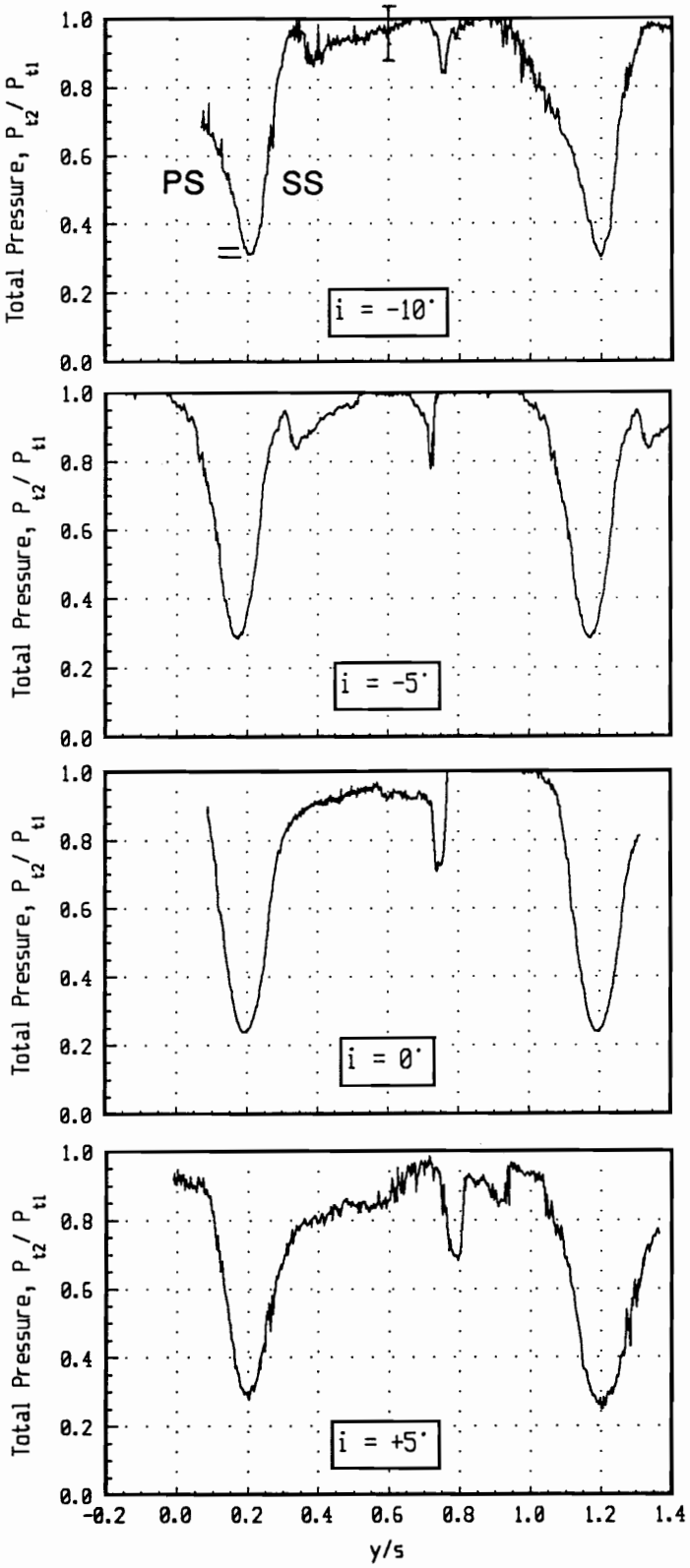

Figure 19. Total Pressure Profiles, x/c = 0.37

surface boundary layer is separated by an impinging shock. This separation generates large losses which show up downstream of the cascade as a thickened wake on the pressure side. For i = +5°, the shadowgraph in Figure 11 shows a separation bubble on the suction surface. Corresponding to this separation bubble, Figure 19 shows the wake to be skewed towards the suction surface.

The full set of profiles measured with the Pitot/static probe downstream of the cascade are presented in Appendix D. In Appendix D, the Mach number, Pitot pressure, total pressure, and static pressure are shown at all measurement locations. The figures in that appendix show that, at all measurement stations, the variation in static pressure across the blade passage is only about ±10%. The Mach number and total pressure can vary by a factor of two across the blade passage, and the Pitot pressure can vary as much as a factor of three. Compared to the variation in the other quantities, the blade-to-blade static pressure variation is quite small.

4.4 LDV Measurements

The two-dimensional LDV system was used to make blade-to-blade measurements downstream of the cascade similar to the profiles measured with the Pitot/static probe. At design incidence, LDV measurements were made at x/c = 0.11 and x/c = 0.37. At both these locations, the flow had been previously measured with the Pitot/static probe. In Figure 20 and Figure 21, the Mach numbers and flow angles measured with the LDV at these locations are plotted along with the Pitot/static probe measurements. Also in these plots are the total and static pressures calculated by combining the corresponding LDV and Pitot measurements. At -10° incidence, LDV measurements were made at x/c = 0.04, and at i = +5°, measurements were made at x/c = 0.10. Due to limited access downstream of the STFF cascade, no Pitot/static probe

measurements were possible at these locations. The Mach numbers and flow angles measured at these locations are plotted in Figure 22 and Figure 23. It should be noted in all these figures that LDV measurements were actually made only at $-0.25 < y/s < 0.75$. Data points shown in these figures at $y/s < -0.25$ or $y/s > 0.75$ are copied from the measured region to provide for a clearer picture of the wakes and a clearer comparison between the LDV and Pitot/static measurements.

As was stated in Chapter 3, one of the advantages of the LDV is its capability to make accurate measurements in turbulent flows. Therefore, the LDV could be used to make measurements in the wake with low uncertainty. The Pitot/static probe measurements were questionable in the wake region due to the unknown response of the static measurement in turbulent flow. The quantity actually measured with a static tap in a turbulent flow is a function of the flowfield and the probe geometry and is not amenable to a theoretical analysis. Figure 20 and Figure 21 both show excellent agreement between the Pitot/static probe and the LDV measurements in the wake. These measurements show that the static taps on the Pitot/static pressure probe measure very close to the true static pressure even in the wake regions.

In Figure 21, it is also apparent that there is good agreement between the LDV and Pitot/static measurements in the core flow region. It can be seen in this figure that the measurements agree within the plotted uncertainty bands (detailed in Appendix A). For the measurements made at $i = 0$, $x/c = 0.11$ shown in Figure 20, the LDV and Pitot/static measurements also generally agree within the measurement uncertainty, with the exception of one point in the center of the blade passage.

Also of interest in these two figures is the variation of the flow angle downstream of the cascade at design incidence. Both plots show the mass-averaged flow angle downstream of the cascade to be approximately 11°. This measurement agrees favorably with the 9° wake deviation angle measured with the Pitot/static probe when one recalls that (1) the uncertainty in the LDV

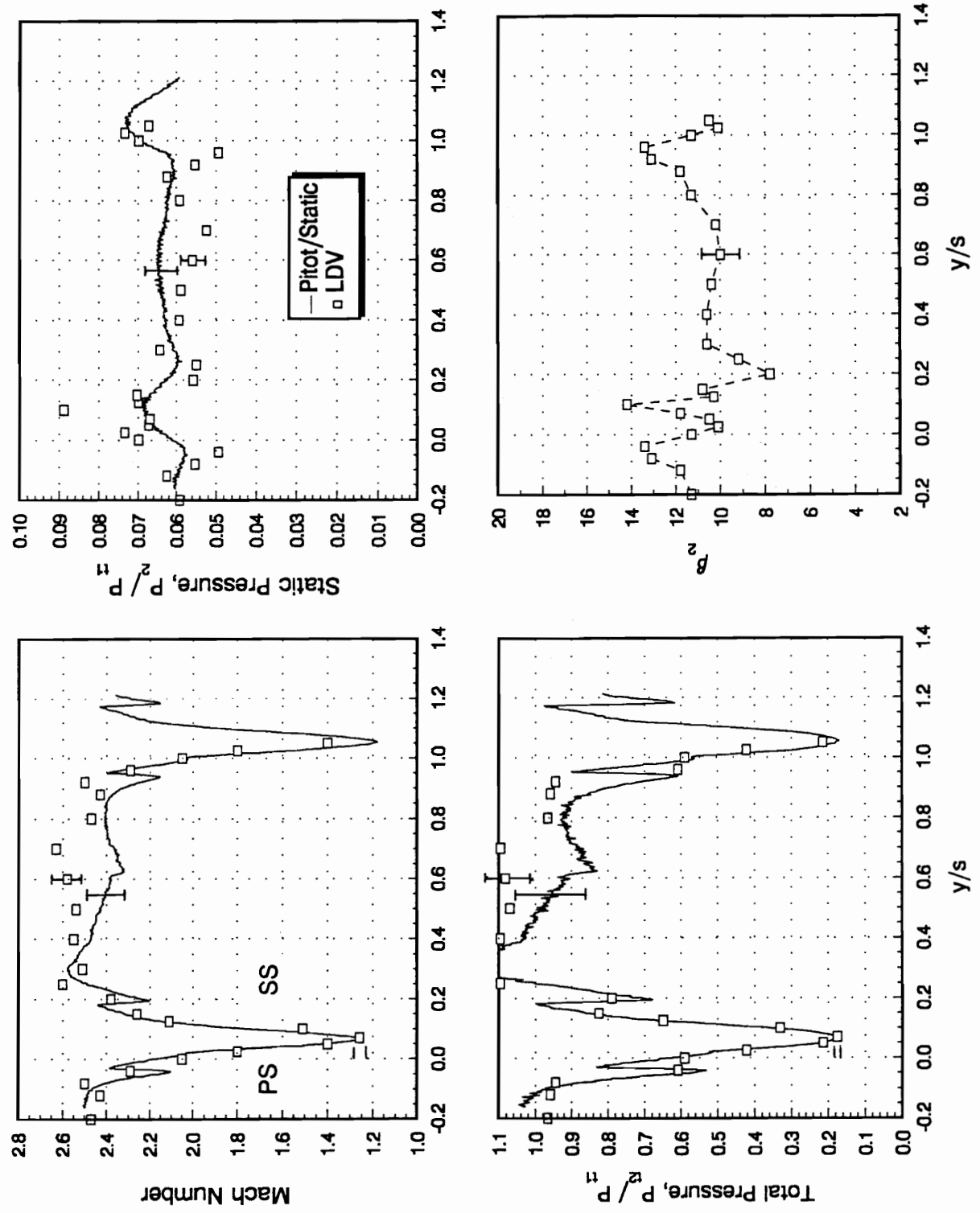

Figure 20. LDV Downstream Measurements, Design Incidence, $x/c = 0.11$

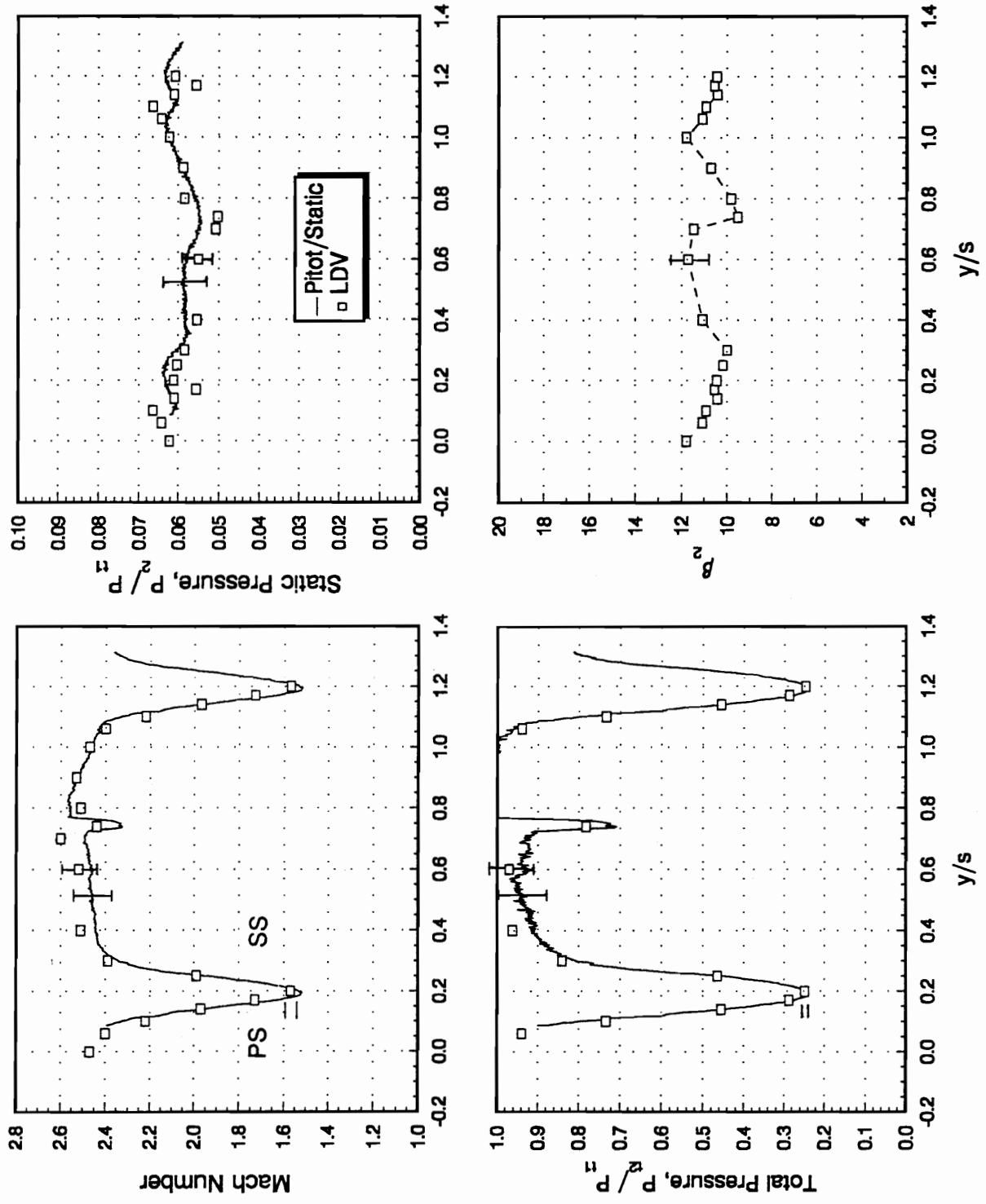

Figure 21. LDV Downstream Measurements, Design Incidence, x/c = 0.37

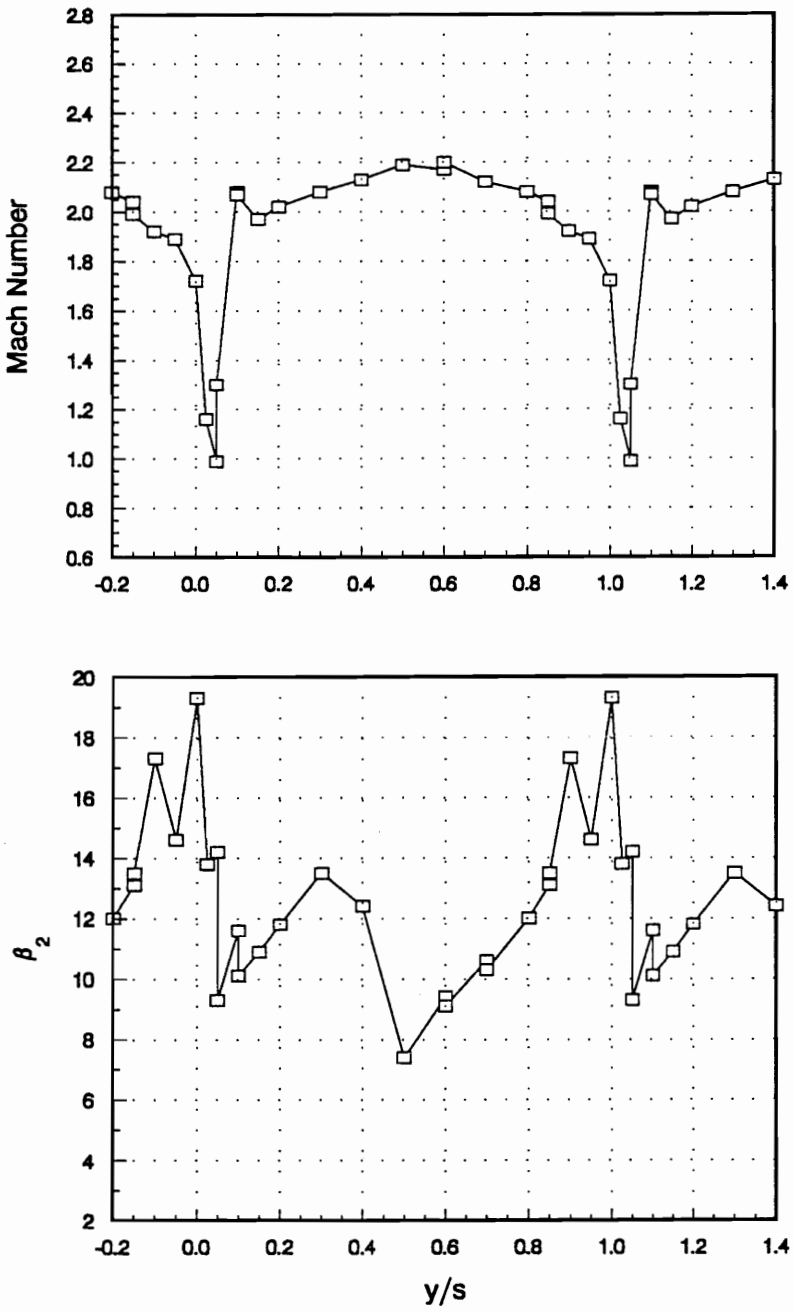

Figure 22. LDV Downstream Measurements, -10° Incidence, x/c = 0.04

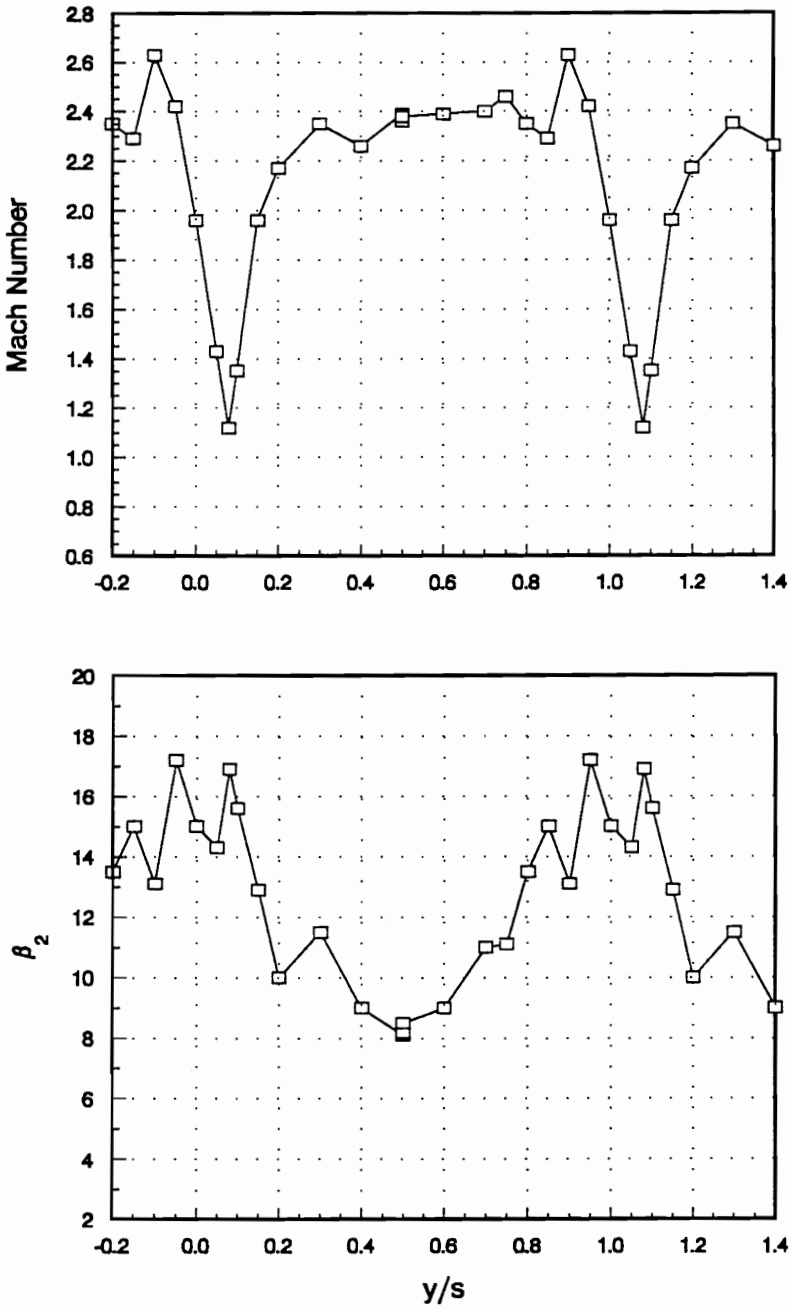

Figure 23. LDV Downstream Measurements, +5° Incidence, x/c = 0.10

measurement of β_2 is ±0.9°, and (2) the mass-averaged flow angle and the wake deviation angle are not necessarily the same thing. In Figure 20, the turning of the flow through the fishtail is apparent. Close to the trailing edge, the "fishtail shocks" actually exist as an expansion fan closely followed by an oblique shock. This occurs because at the end of the blade, the flow must first expand around the blunt trailing edge before being turned back by a shock. At x/c = 0.11, the expansion and compression have not yet completely merged. This can be seen in the variation of β_2 from y/s = -0.25 to 0.3. From y/s = -0.25 to y/s = -0.05, the right running expansion wave off the pressure side of the trailing edge turns the flow up from β_2 = 10° to β_2 = 14°. At y/s = -0.05, the lower fishtail shock then turns the flow back. On the suction side of the trailing edge, the same behavior can be seen, only now the waves are left running instead of right running, and the directions of flow turning are reversed. From y/s = 0.3 to y/s = 0.2, the left running expansion wave turns the flow from 10.5° to 8°. At y/s = 0.2, the left running shock then turns the flow back. Figure 21 shows that further downstream, at x/c = 0.37, the flow direction has become more uniform and the variation of the flow angle is small, only ±1°.

Figure 22 shows the Mach number and flow angle measured with the LDV at i = -10°, x/c = 0.04. This rake is very close to the trailing edge and the gradients in the wake are sharp. Through the center of the wake, the flow changes from β_2 = 19° on the pressure side to β_2 = 9° on the suction side. In agreement with the Pitot/static probe measurements made at i = -10°, x/c = 0.37, the LDV measurements show the wake to be steeper on the suction side than on the pressure side, indicating that the influence of the pressure side boundary layer separation bubble extends far downstream. The average flow angle is approximately 11°, very close to the trailing edge metal angle. The influence of the fishtail structures, however, is not readily apparent at this location due to the close proximity of the wake and the trailing edge shocks and the complex influence on the pressure surface separation bubble with the downstream flowfield.

In Figure 23 the Mach number and the flow angle at $i = +5°$, $x/c = 0.10$ are plotted. The distribution of flow angle is again difficult to interpret, due to the close proximity of the wake and trailing edge shocks and the complex interaction of the suction side separation bubble with the downstream flow. The average flow angle is found to be approximately 12°, reaffirming that the exit flow angle is nearly independent of the inlet flow angle.

4.5 Integrated Loss Coefficients

The measurements presented above show a great deal about the detailed structure of the cascade flowfield, but, in the form presented, say little about the performance of the cascade. In order to obtain a global assessment of the cascade performance, the detailed measurements of the downstream flowfield described above must be integrated. This can be done in one of two ways. In the first of these, an average downstream quantity, $\bar{n}$, is found by integrating the mass flux weighted value of n along a line parallel to the cascade across one blade passage. That is

$$\bar{n}_2 = \frac{\int_0^s (\rho u)_2 n_2 \, dy}{\int_0^s (\rho u)_2 \, dy} \tag{4.1}$$

$\bar{n}_2$ is then called the *mass-averaged* value of n_2. To compute the mass-averaged loss coefficient, ϖ_2, the mass-averaged total pressure, $\bar{p}_{t2}$, is found from

$$\bar{p}_{t2} = \frac{\int_0^s (\rho u)_2 p_{t2}\, dy}{\int_0^s (\rho u)_2\, dy} \tag{4.2}$$

and then the mass-averaged loss coefficient is calculated from

$$\bar{\omega}_2 = \frac{1 - \dfrac{\bar{p}_{t2}}{p_{t1}}}{1 - \dfrac{p_1}{p_{t1}}} \tag{4.3}$$

The second way of calculating an average downstream value is to postulate a station far downstream of the cascade, station 3, at which all quantities are mixed out and uniform across the blade passage. The flow area at station 3 is the same as for station 2, since the cascade is assumed to be infinite. The properties of the flow at station 3 can be found by solving the conservation of mass, momentum, and energy equations from station 2 to station 3. For cascades with uniform inlet flow, the total temperature will vary little from blade to blade at station 2, and can be assumed to be constant and equal to T_{t1}. The conservation of energy equation then becomes:

$$T_{t3} = T_{t2} = T_{t1} \tag{4.4}$$

The remaining two equations are then easily solved.

The flow properties at station 3 are then called the *mixed-out* values. The mixed-out loss

coefficient for the cascade, ω_3 is found by solving for p_{t3} and then computing

$$\omega_3 = \frac{1 - \frac{p_{t3}}{p_{t1}}}{1 - \frac{p_1}{p_{t1}}} \tag{4.5}$$

The mixed-out loss coefficient will always be larger than the mass-averaged loss coefficient since the mixing out process generates entropy.

The loss coefficients calculated for the Pitot/static probe data are plotted in Figure 24. The LDV measurements are not, by themselves, sufficient to calculate a loss coefficient. However, when both LDV and Pitot measurements are available, as they are for the design incidence, loss coefficients can be calculated. The loss coefficients for design incidence calculated from the LDV/Pitot data are also plotted on Figure 24.

In analyzing the results shown in Figure 24, it must be understood that the measurement of the loss coefficient in the STFF cascade is somewhat crude. As explained in Appendix A, the high Mach numbers in the cascade make an accurate total pressure measurement difficult, so that the measurement uncertainty in the loss coefficient is ±0.068. Keeping this in mind, some trends in the loss plots can be seen. In Figure 24 the loss bucket for the STFF cascade is apparent. The minimum loss angle is somewhere between design incidence and i = -5°. The minimum loss coefficient is 0.11 mass averaged or 0.16 mixed out. In general, the mixed-out loss coefficients are 30% higher than the mass-averaged loss coefficients. The losses rise sharply at positive incidence, but only slightly at negative incidence. At design incidence, the one point at which both Pitot/static and LDV/Pitot measurements of the loss were made, there is excellent agreement

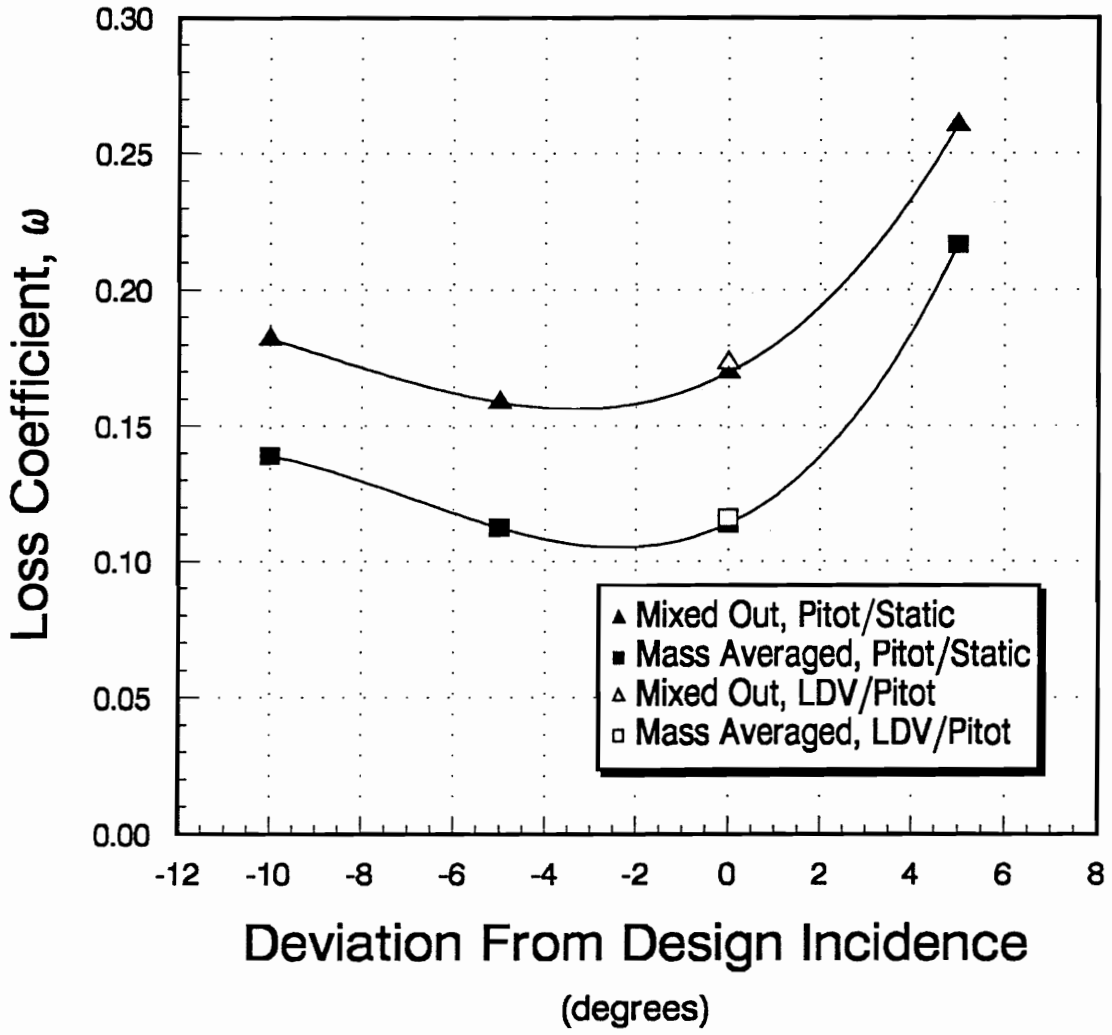

Figure 24. Measured Loss Coefficients for the STFF Cascade

between the two loss measurements.

The downstream profiles of the flowfield can also be used to determine the source of the losses in the STFF cascade. Schreiber[11] reasoned that for supersonic blading, viscous losses are generated only in the boundary layers, and appear downstream only in the wake region. Shocks, however, extend all the way across the blade passage, and so the shock losses account for all the losses in the core flow, and some of the losses in the wake. By assuming that, at the edge of the wake, all losses are due to shocks, and that the shock losses vary linearly across the wake, the viscous and shock losses are separated as shown in Figure 25. Thus, an estimate of the source of the measured losses can be obtained. In the analysis that follows, the losses will be split in this fashion, but the losses will be referred to as passage and wake losses rather than shock and viscous losses, since this method for determining the source of the cascade losses was developed for use in subsonic-axial, supersonic-relative blading, and not for supersonic through-flow blading. In fact, in Chapter 6 it will be shown that some adjustments to this method are required to determine the shock and viscous losses in a supersonic through-flow cascade.

Table 4. Measured Passage and Wake Losses

i	ϖ_2	ω_3	ϖ_w	ϖ_{pg}
-10	0.139	0.182	0.077	0.062
-5	0.112	0.159	0.072	0.040
0	0.114	0.170	0.076	0.038
5	0.216	0.260	0.064	0.152

The results of dividing the loss profiles in this way are shown in Figure 26. These losses

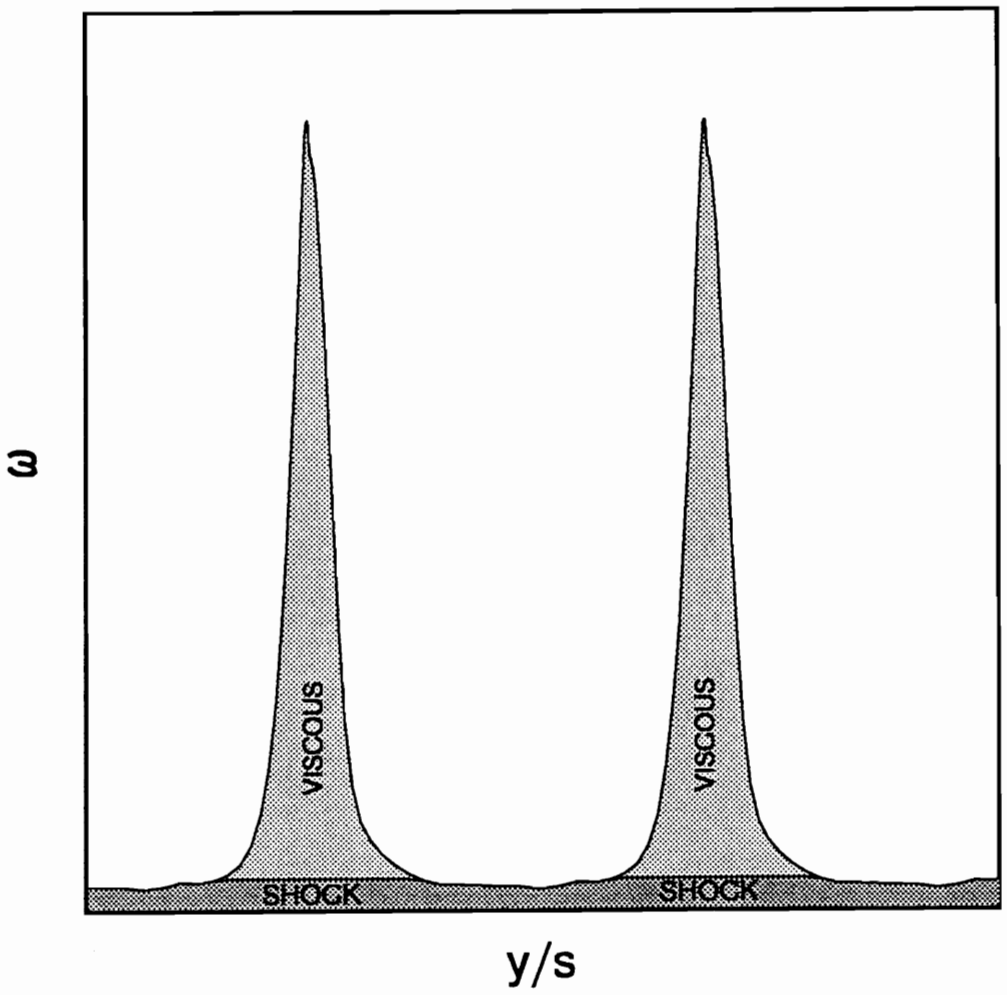

Figure 25. Division of Viscous and Shock Losses

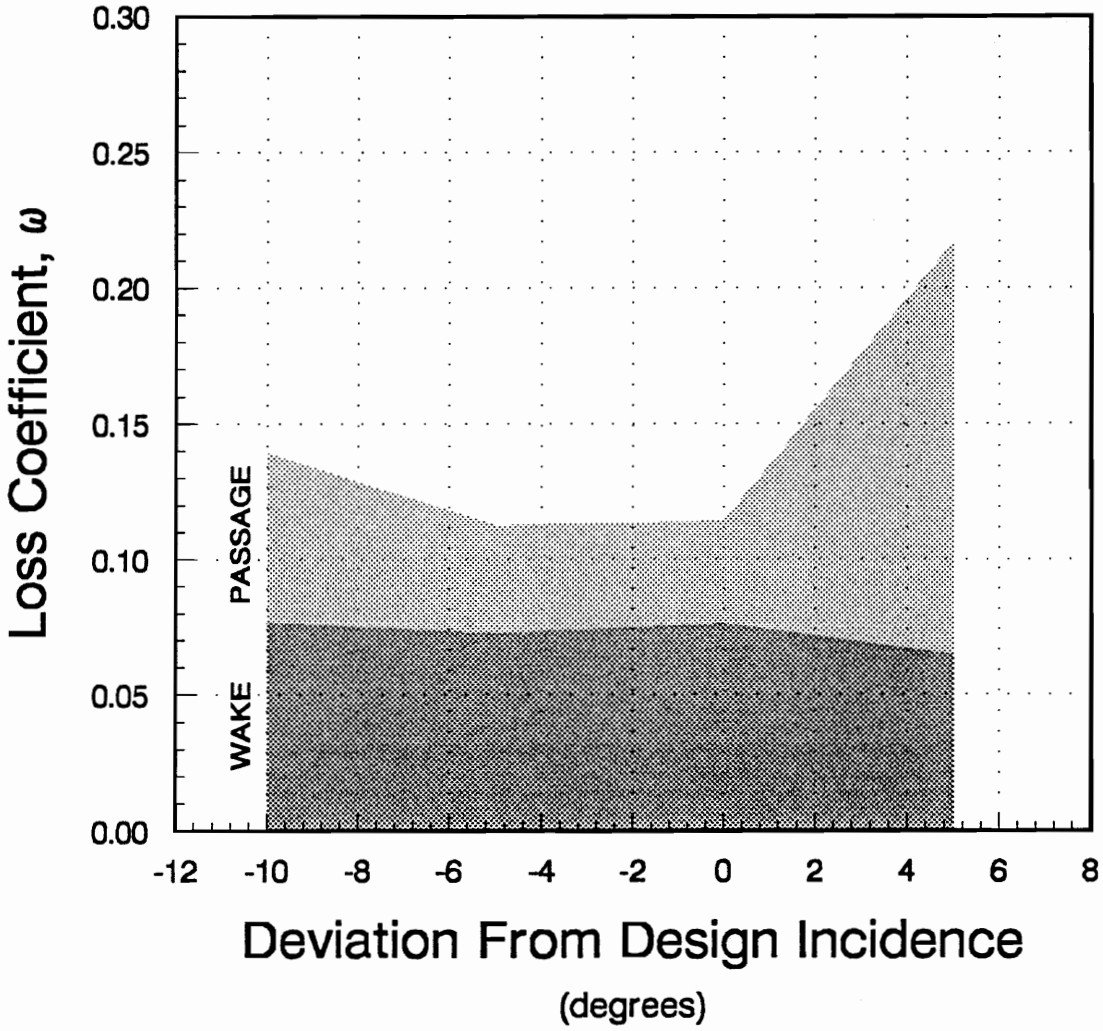

Figure 26. Measured Passage and Wake Losses, Mass Averaged

are also listed in Table 4. This figure shows two interesting results. First, the wake losses are nearly constant at approximately 0.073. There is very little variation with incidence. The shape of the loss bucket is due almost entirely to the variation in passage-shock losses. The second thing to note in this figure is the distribution of the losses. At design, 35% of the losses are due to passage shocks. At +5° incidence, the passage losses rise to approximately 70% of the total losses. It appears that shocks can account for a substantial portion of the losses in the STFF, even though no normal shocks exist in the blade passage. It must be kept in mind, however, that the numbers on the loss coefficients are somewhat rough due to (1) the large uncertainty in the total pressure measurements, and (2) the approximate nature of the loss source division. Further analysis in the following two sections will be used to refine these numbers.

Chapter 5

Numerical Analysis

A computational simulation of the flow through the supersonic through-flow fan blade cascade was performed in order to aid in the interpretation of the experimental data and to gain an understanding of the capabilities and limitations of computational fluid dynamics (CFD) to predict the flow in a STFF. In this section, the numerical modeling of the flow will first be described, followed by a presentation of the results of the numerical studies. Detailed analysis of the calculated flowfield will be presented for design incidence, along with comparison to the measured flow. Integrated loss coefficients will be presented for the 15° range of incidence measured in the wind tunnel.

5.1 Numerical Model

Numerical modeling of the flow was accomplished using ANSERS, a two-dimensional, implicit, cell-centered, finite-volume code developed at VPI. A detailed description of the code can be found in Taylor[12]. The code was employed to solve the complete Reynolds averaged Navier-Stokes equations. Inviscid flux terms were evaluated using the upwind scheme of Van

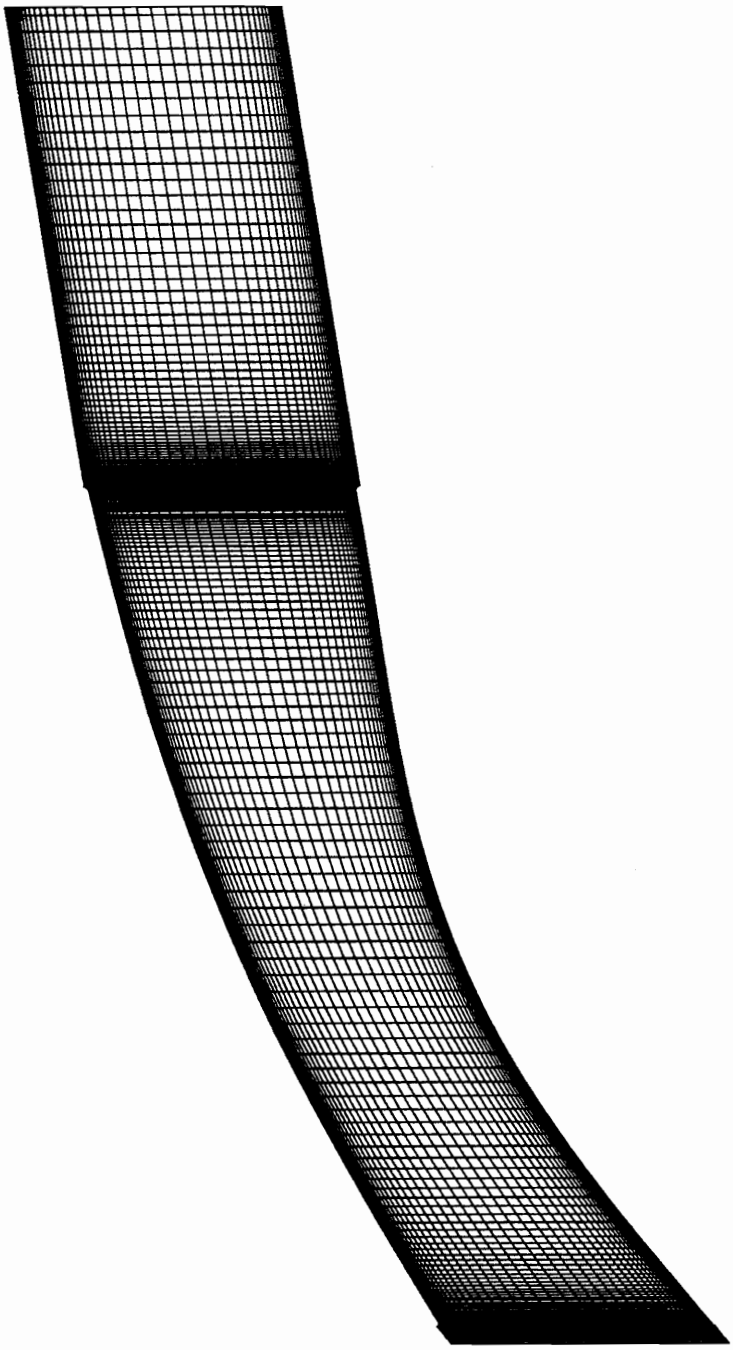

Figure 27. Computational Grid, Design Incidence

Leer (Flux Vector Splitting). The solution was performed on a 65 × 210 H-grid. A unique grid was used for each inflow angle. The grid for design incidence is shown in Figure 27. Turbulence was modeled using the Baldwin-Lomax eddy viscosity model. This model was chosen for its computational simplicity.

All calculations were performed with an inflow Mach number of 2.36. Four incidence angles were analyzed in order that the effect of entrance flow angle could be evaluated. All calculations were within 1° of the nominal measured incidence angles of β_1 = 27°, 32°, 37°, and 42°, and will be referred to in this section by these nominal values.

5.2 Comparison to Experimental Data

For the experimental data, the best way to see the global behavior of the flow through the STFF is with the shadowgraphs. For the CFD data, the best way to see the global behavior of the flow is with a contour plot. Figure 28 shows a contour plot of the calculated static pressure at design incidence. Comparison of this plot with Figure 10 illustrates the general agreement of the calculated and experimental flowfields. The positions of the leading edge shocks agree quite well in both of these figures, as do the positions of the reflected shocks in the blade passage. The calculation shows the left running leading edge shock (suction side) reflects off of the pressure surface at 15% chord as a single shock, just as in the shadowgraph. The calculation also shows the right running leading edge shock (pressure side) impinging on the suction surface at approximately 58% chord and reflecting weakly, if at all. This again agrees well with the experimental data. Comparison of Figure 28 with Figure 10 shows that the positions of the fishtail shocks are also predicted accurately. This comparison would then indicate that there

exists good agreement between the calculated and measured flows. The only discrepancy between the contour plot of static pressure and the shadowgraph of the cascade at design is that the contour plot does not seem to show the "precompression-type" shock discussed in the Experimental Results section.

The measured and calculated blade static pressures are shown in Figure 29. It can be seen from this figure that the agreement between the calculated and measured blade static pressure is generally good, with the following caveats. The calculated static pressure over the last part of the blade is generally low. This may be due in part to the slight three-dimensionality of the experimental flowfield. Also, the calculated static pressure shows no evidence of the "precompression-type" shock. On the measured profile, this shock causes distinct peaks at 32% chord on the pressure surface and at 65% chord on the suction surface. It is surmised that the grid is not sufficiently refined in the region where the compression waves from the suction surfaces coalesce to resolve this shock.

Comparison between the measured downstream rake profiles and the calculated flow also shows good agreement. Figure 30 shows the calculated Mach number, total pressure, static pressure, and Pitot pressure at $x/c = 0.37$ with both the Pitot/static probe and the LDV measurements. In Figure 30, all profiles show excellent agreement between the calculated and measured wake centers. The calculated profiles, however, do show the wake to be somewhat deeper than the measured wakes.

The conclusion to be drawn from all of these comparisons is that, although the calculated flowfield differs in some details from the cascade measurements, the code generally does a good job of predicting the flow in the STFF cascade at design incidence. Some of the discrepancies that do exist in the calculated flow could probably be resolved with further analysis. For example, with a refined grid, the code should be able to resolve the precompression shock. The code is

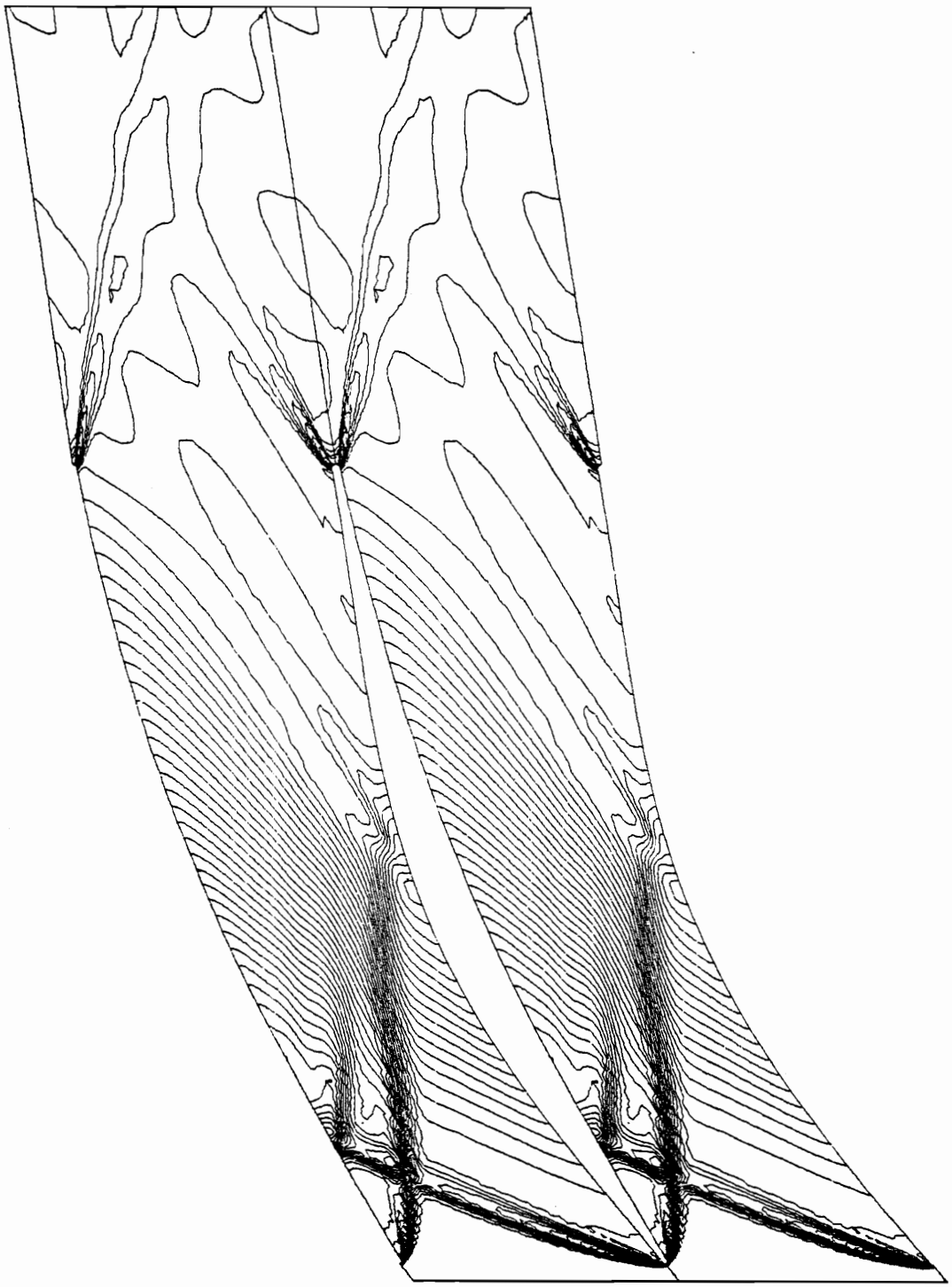

Figure 28. Contour Plot of Static Pressure at Design Incidence, Calculated

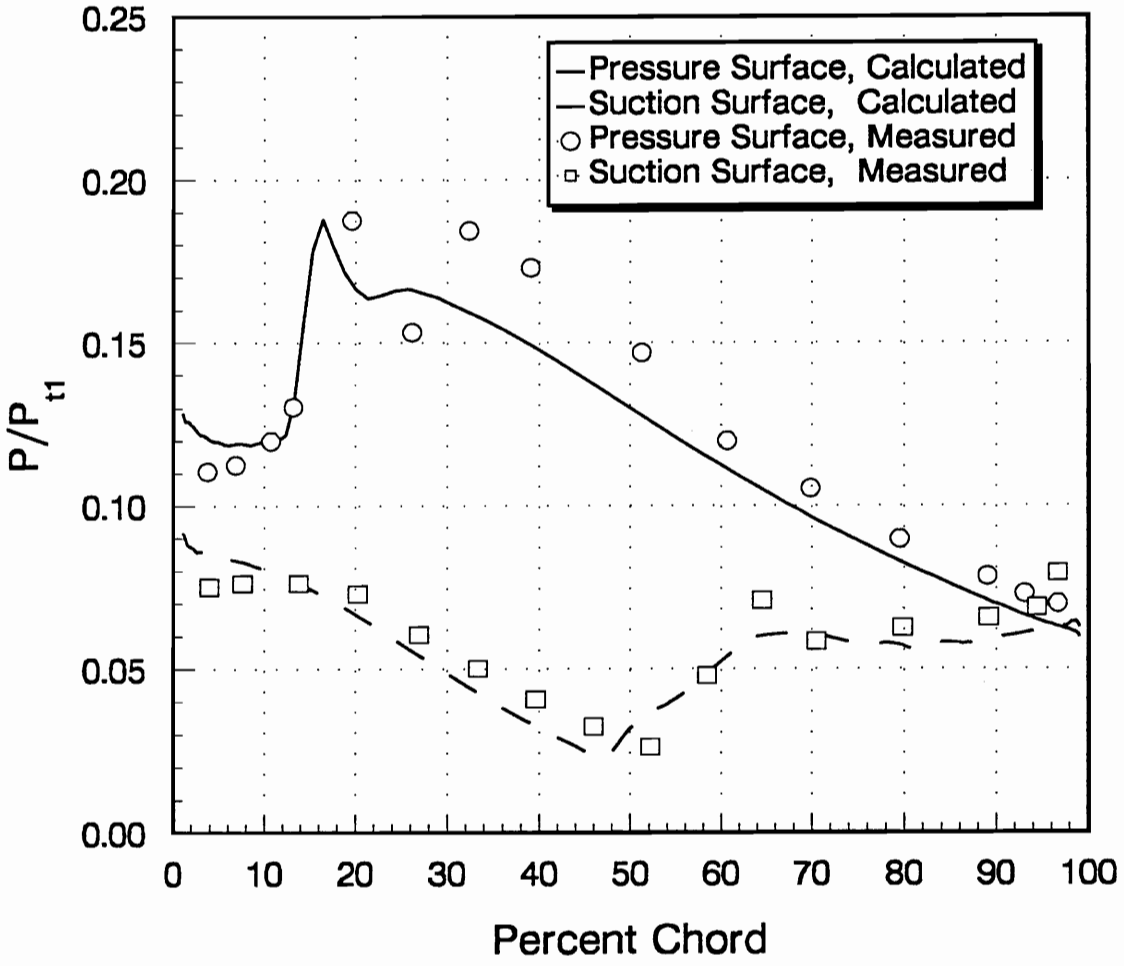

Figure 29. Blade Surface Pressure, Measured and Calculated

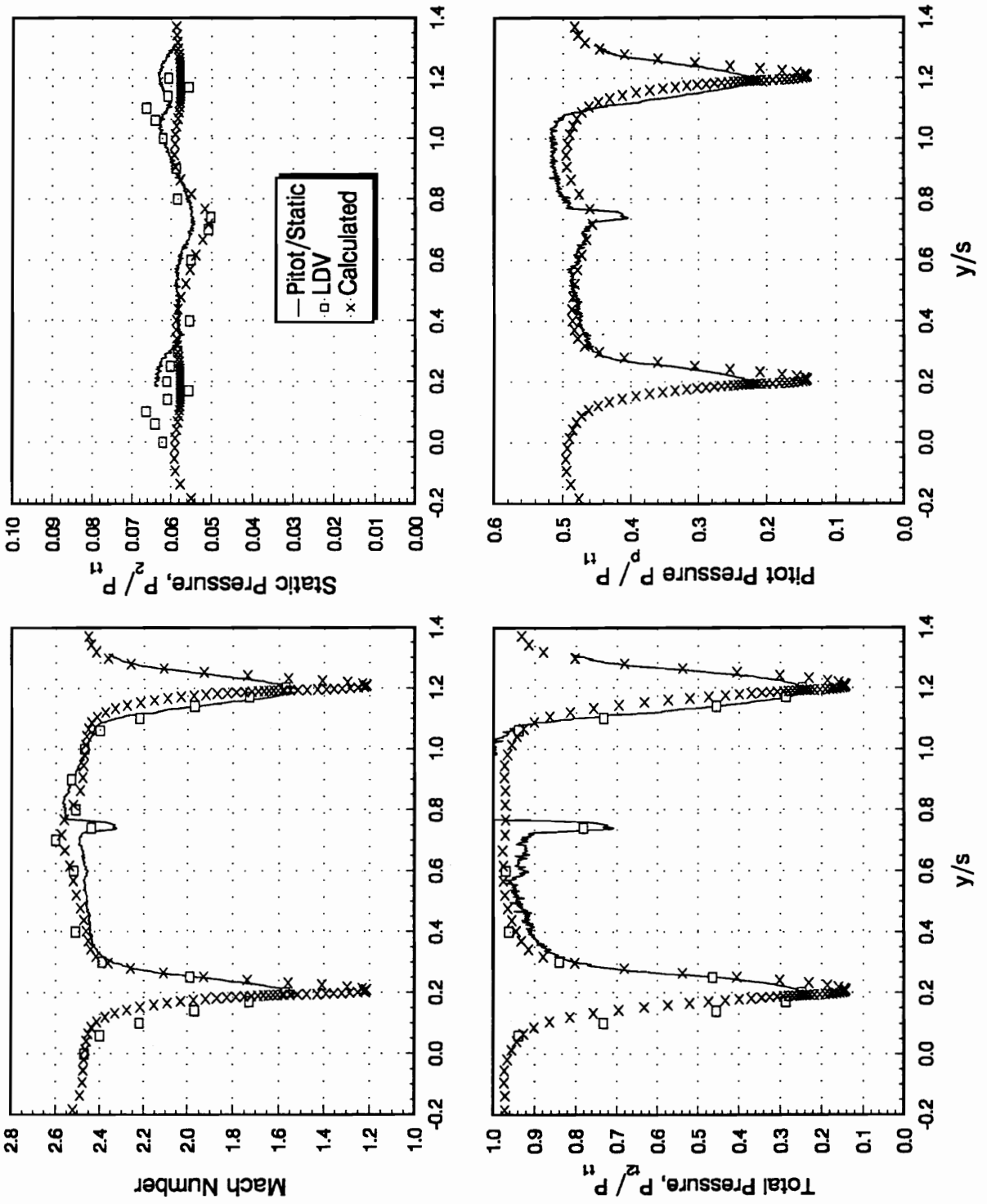

Figure 30. Downstream Flowfield, $i = 0°$, $x/c = 0.37$, Measured and Calculated

capable of adequately describing most of the features seen in the STFF cascade at design incidence.

Comparisons between the calculated flowfield and the cascade measurements at off design are not quite as good. Calculations of the flowfield by Andrew[13] at -10° incidence show the shock boundary layer interaction region to be poorly modeled. The CFD calculation shows a separation bubble at the shock impingement point, but the measured upstream influence of the separation zone, as revealed by the blade surface pressure, and the downstream reattachment point of the boundary layer, as revealed in the shadowgraph, are not correctly predicted. Further, the measurements show the separation zone on the pressure side of the blade to have a marked influence on the downstream rake measurements. The cascade measurements at -10° incidence show the wake to be thicker on the pressure side — the Mach number does not rise as quickly on the pressure side of the wake as on the suction side, and the total pressure is depressed on the pressure side of the wake. This behavior is not predicted by ANSERS, which shows the wake to be roughly symmetric. Thus, the code not only fails to describe the extent of the separation region, it also fails to describe the separation region's influence on the rest of the flowfield. The narrow wake region in the calculated profile indicates that the code does not predict the magnitude of losses generated by the boundary layer separation.

The comparison of the calculated flow with the cascade measurements at these two incidence angles shows that the CFD code is capable of adequately predicting the flow in a STFF cascade as long as there are no regions of strong shock/boundary layer interaction. The strong shock/turbulent boundary layer problem is a difficult one, and the turbulence in the separated region is not adequately modeled by the Baldwin-Lomax eddy viscosity model. It must be remembered that, although the Baldwin-Lomax model is frequently used to calculate separated flows, there is no theoretical justification for using this model in such flows. The modeling of

separated flows with this model has many faults. Among them are the fact that the Baldwin-Lomax model was developed based on data from boundary layer profiles. In a separated region, the boundary layer assumptions do not apply. Because it is an eddy viscosity model, the Baldwin-Lomax model predicts that the Reynolds shear stress, $-\rho\overline{u'v'}$ is zero at the separation point. This is clearly incorrect. So it is not surprising that the flow is not adequately modeled when separated regions exist. It is therefore concluded that the ANSERS code is accurate in predicting the flow in a STFF at design incidence, but has some trouble predicting the off-design flowfield when regions of strong shock/boundary layer interaction are present.

5.3 Integrated Loss Coefficients

The integrated loss coefficients, ϖ_2 and ω_3, were calculated from the CFD results for the four measured incidence angles and are plotted in Figure 31 along with the measured loss coefficients. The loss coefficients for -10° and +5° incidence were calculated using the flow solutions of Andrew[13]. The passage and wake losses were calculated from the CFD data using the same procedures as outlined in Chapter 4 and are plotted along with the experimentally measured passage and wake losses in Figure 32. These results are also listed in Table 5. It is clear from these figures that the calculated and measured losses agree within the experimental uncertainty of ±0.068. It is also seen in Figure 32 that the calculated passage and wake losses agree well with the measured losses, particularly at design and -5° incidence. The lesser agreement in the calculated ϖ_{pg} and ϖ_w with the measured results at -10° and +5° incidence is to be expected, since separated regions of the flow exist for both these cases. The comparison of the measured and calculated integrated loss profiles is perhaps more favorable than the comparison

Table 5. Measured Passage and Wake Losses

i	Measured				Calculated			
	ϖ_2	ω_3	ϖ_w	ϖ_{pg}	ϖ_2	ω_3	ϖ_w	ϖ_{pg}
-10°	0.139	0.182	0.077	0.062	0.151	0.196	0.058	0.093
-5°	0.112	0.159	0.072	0.040	0.108	0.161	0.070	0.038
0°	0.114	0.170	0.076	0.038	0.110	0.165	0.072	0.038
5°	0.216	0.260	0.064	0.152	0.170	0.230	0.076	0.094

of the measured and calculated downstream profiles. This, again, is to be expected since the integration process tends to hide the discrepancies which exist between the two profiles.

5.4 Discussion

Comparisons of the measured cascade data to numerical predictions made with a 2-D, finite volume CFD code show that the flow is predicted well at the design condition, but that off-design predictions are less satisfying. The downfall of the numerical predictions of the STFF cascade flow is the inability to adequately model the flow in regions of strong shock/boundary layer interaction. At the design condition, shocks within the blade passage are relatively weak, and large regions of separated flow do not occur. When the blades are at large angles of attack, the shocks generated at the leading edge of the blades are much stronger, and separation bubbles occur where these shocks impinge upon the boundary layer. The code does predict the presence of separated regions, but comparison of the computed flow to the cascade data shows that neither the extent of the upstream influence nor the location of the downstream reattachment point of the separated regions are correctly calculated. The errors in the modeling of the strong

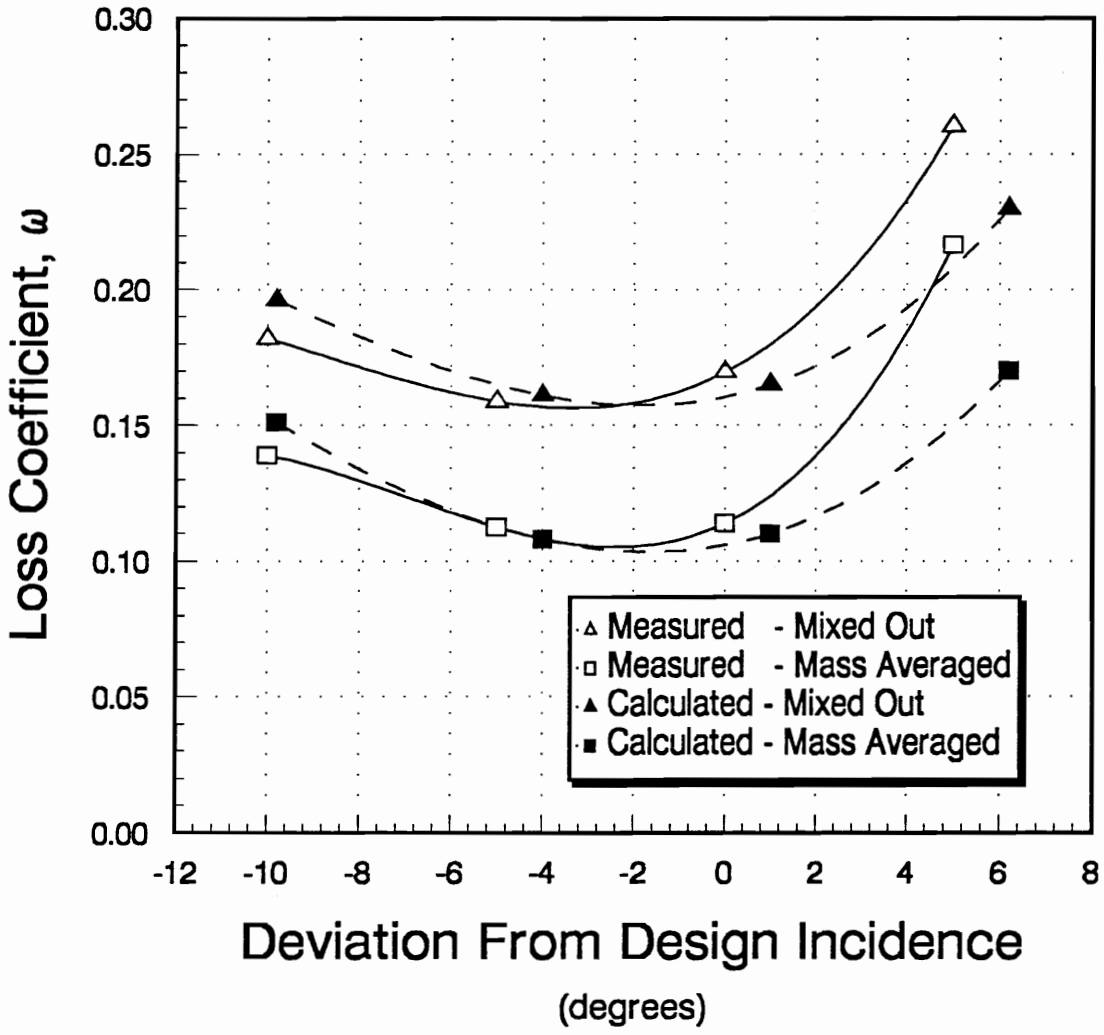

Figure 31. Integrated Loss Coefficients, Measured and Calculated

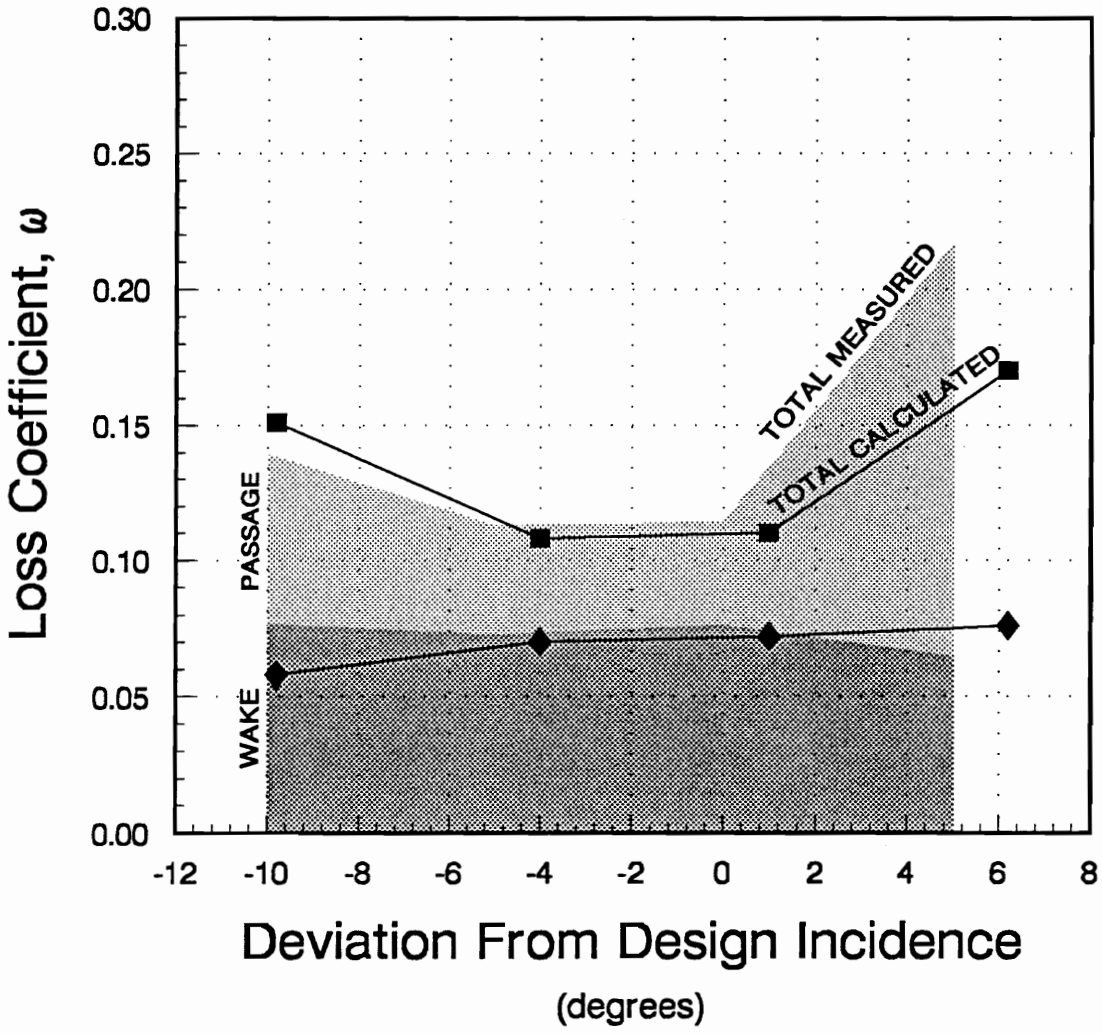

Figure 32. STFF Cascade Passage and Wake Losses, Measured and Calculated

shock/boundary layer interaction cause discrepancies with the cascade data not just in the immediate vicinity of the separation bubble, but also far downstream in the wake.

The heart of the problem in calculating the strong shock/boundary layer interactions at off design lies in the modeling of the turbulence in separated flows. The modeling of the turbulence in high speed separated flows is difficult, and is the subject of much ongoing research. The problem of adequately modeling the flow in these separated regions will not be easily resolved.

This discussion of the shortfalls of modeling the flow in a STFF with computational fluid dynamics should not be interpreted as indicating that the codes are not useful tools. On the contrary, the code actually does a very good job of predicting the flow at design and -5° incidence, and the -10° and +5° calculations are not badly inaccurate. The losses predicted by ANSERS agree quite well with the measured losses. The above discussion is merely intended to point out the limitations of these numerical tools when used to calculate the flow through supersonic through-flow blading so that the analyst can better interpret his results. In this context, it is just as important to understand what the numerical model can't do as to understand what it can.

Chapter 6

Shock Loss Modeling

A model has been developed for the losses from the leading edge shocks. The results of this relatively simple modeling of the leading edge shock losses can be used to better understand the experimental and computational data. In the following chapter, the model for the leading edge shocks will be described, and the estimates of shock losses based on this model will be presented. The estimates of shock losses will be compared to the computational results to show how shock losses and viscous losses are confounded in the wake region, and that a significant fraction of the losses in the wake arise from inviscid effects.

6.1 Shock Loss Model

The basis for the modeling of the leading edge shocks is the detached shock wave model of Moeckel[14]. This model is designed to predict the location and form of shocks standing off of an isolated body in a supersonic flow. The STFF blades are, of course, not isolated bodies, but the model is easily extended to model the leading edge shocks from these blades.

Moeckel used as the starting point for his model the assumption that the shape of any

shock wave standing off a planar body would be a hyperbola. He further made the assumption that the upper and lower asymptotes of the hyperbola would be left and right running Mach waves. In this way, the shock strength would go to zero far from the body. The location of the body sonic point, S, is assumed to be at the point on the body where the slope is equal to the minimum angle of a wedge which would detach a shock, θ_d, as shown in Figure 33. The sonic point on the shock, that is the point on the shock behind which the flow is at Mach 1, is known if the incoming Mach number and the form of the shock wave is known. Moeckel assumed that the sonic line, that is the locus of points in the flow at which the flow is sonic, is a straight line as shown in Figure 34. Moeckel then used these assumptions on the shock wave and sonic line shapes to solve for the location of the shock sonic point, S, and thus the form and location of the detached shock wave, by solving the conservation of mass in the region bounded by the detached shock, the sonic line, the body, and the stagnation streamline. With this analysis, he was able to calculate the location of point S as a function only of the incoming Mach number, M, and the height of the body at the sonic point, y_{sb}.

To model the leading edge shocks of the STFF cascade, Moeckel's model was applied with the following modifications. The stagnation streamline was assumed to intersect the blade at the furthest point forward on the leading edge. If a blade surface was at a positive incidence, δ, to the flow, the solution found using Moeckel's method was patched to an oblique shock with turning δ at the point on Moeckel's shock profile where the flow would be turned by δ. The shock wave off the suction surface and the shock wave off the pressure surface were then computed independently. With the shape of the waves known, the total pressure loss across each shock could be found. To obtain the total pressure ratio across both shocks, the total pressure ratios across each shock were multiplied.

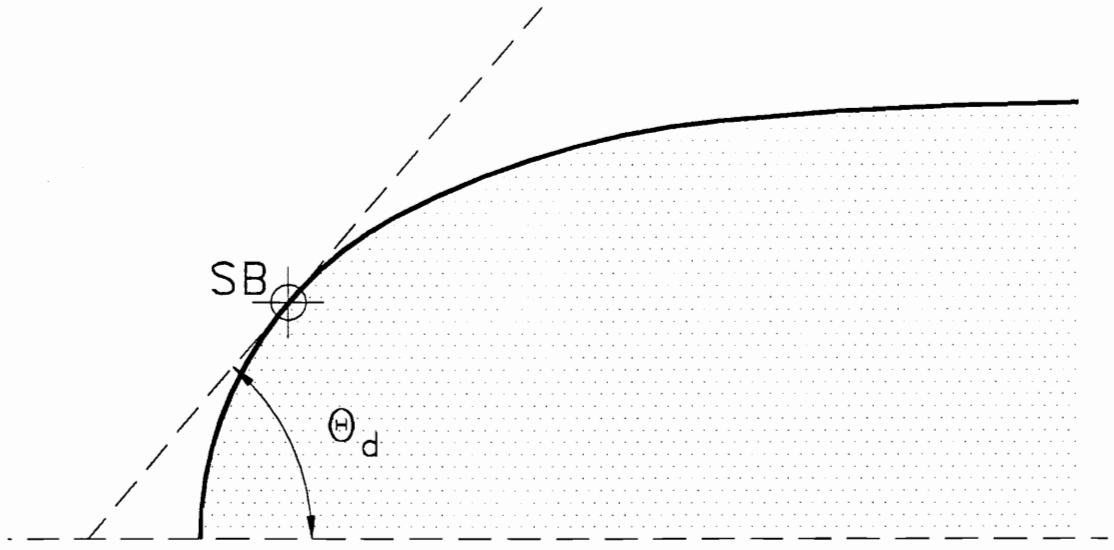

Figure 33. Approximate Location of the Body Sonic Point

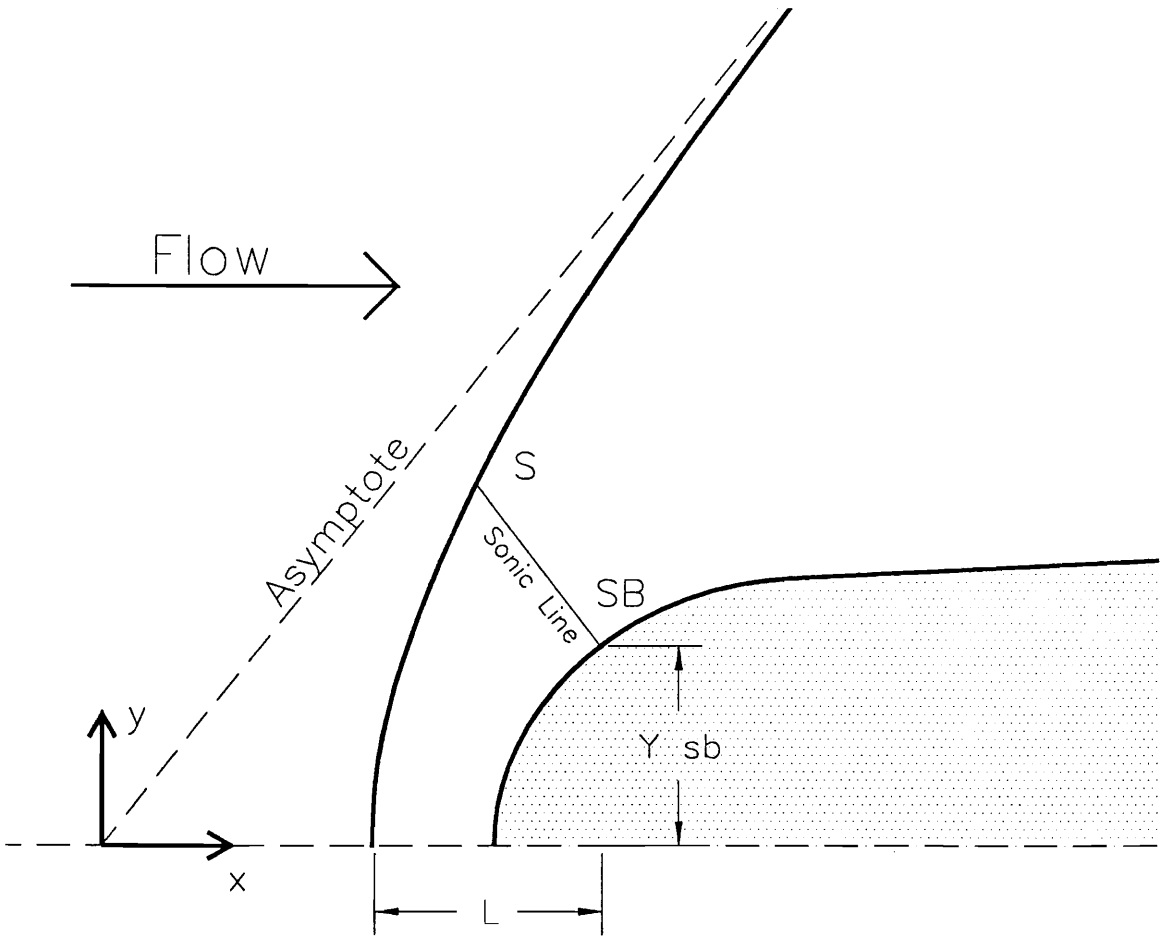

Figure 34. Graphical Representation of Moeckel's Shock Model

6.2 Results

The spanwise distribution of shock losses calculated with this model are plotted in Figure 35. As a reference, the downstream distributions of loss from all sources, as calculated using ANSERS, are also plotted in Figure 35. The interesting thing to note from these profiles is that the shock loss model has generated loss profiles with wakes. The dips in the total pressure profiles calculated from the shock model are, of course, not wakes in the conventional sense, since the model is an inviscid one. What these results show is that the leading edge shocks generate an "inviscid wake" due to the fact that the shock waves are strongly curved near the leading edge. The shock is strongest just in front of the leading edge, where it is normal to the flow. Because these losses will diffuse very little from the near blade region as the flow moves downstream, the maximum shock losses will appear in the same region downstream of the blades as the viscous losses and will be impossible to distinguish.

From Figure 35, it is apparent that a significant portion of the losses in the wake region are actually due to inviscid effects. In fact, the shock losses are a much higher proportion of the wake losses than Figure 35 would indicate, since the shock loss model and CFD profiles are somewhat mismatched. The total pressure profile plotted for the shock loss model is calculated at the entrance to the blade passage where the mass flux, ρu, is constant. The total pressure profiles shown for the CFD data are calculated downstream of the blade passage where the mass flux is not constant. In the wake region, ρu is about 60% of the core flow mass flux. In Figure 36 the loss profiles are plotted multiplied by the mass flux to give a clearer indication of the shock loss contribution to the wake losses.

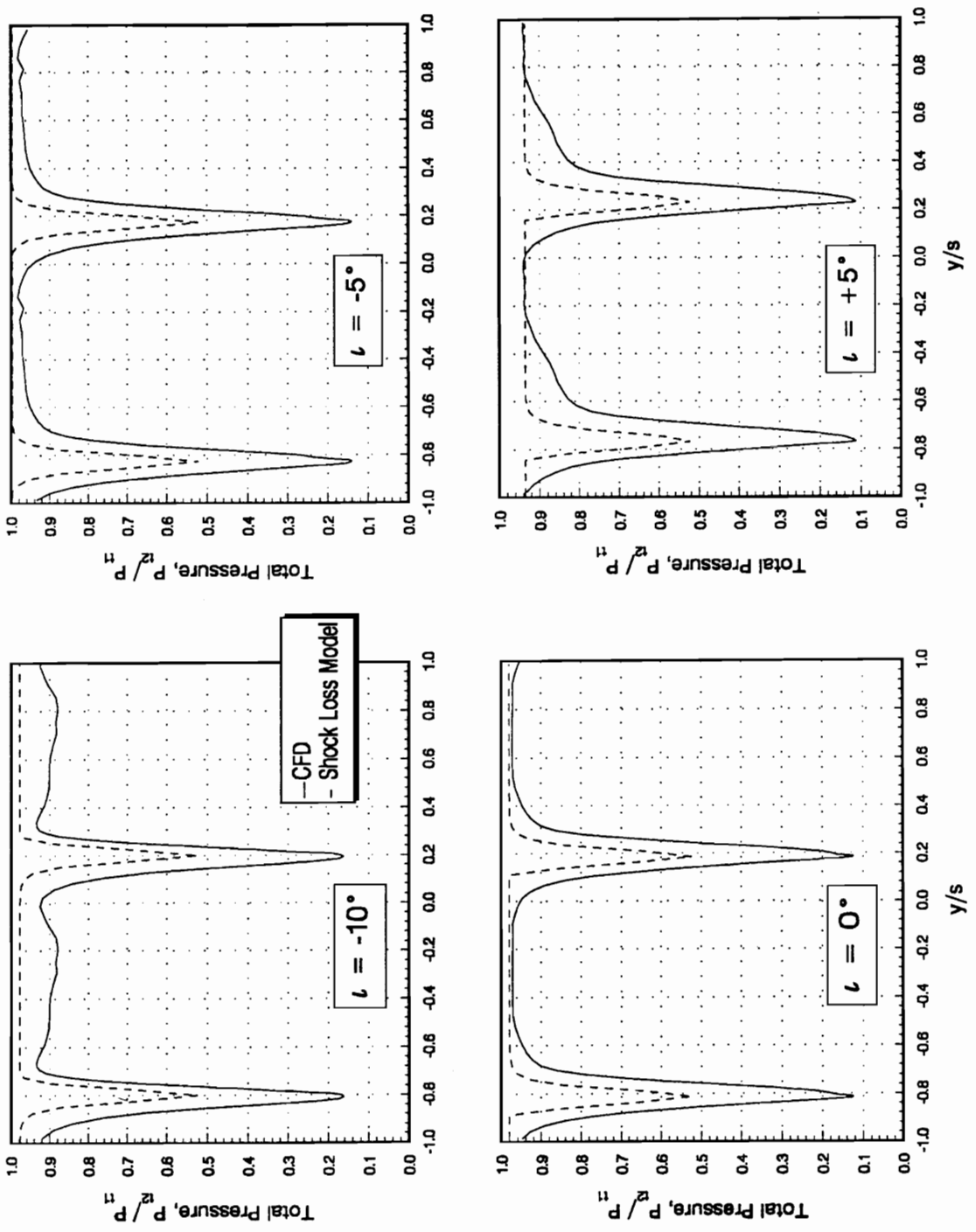

Figure 35. Calculated Leading Edge Shock Loss Profiles

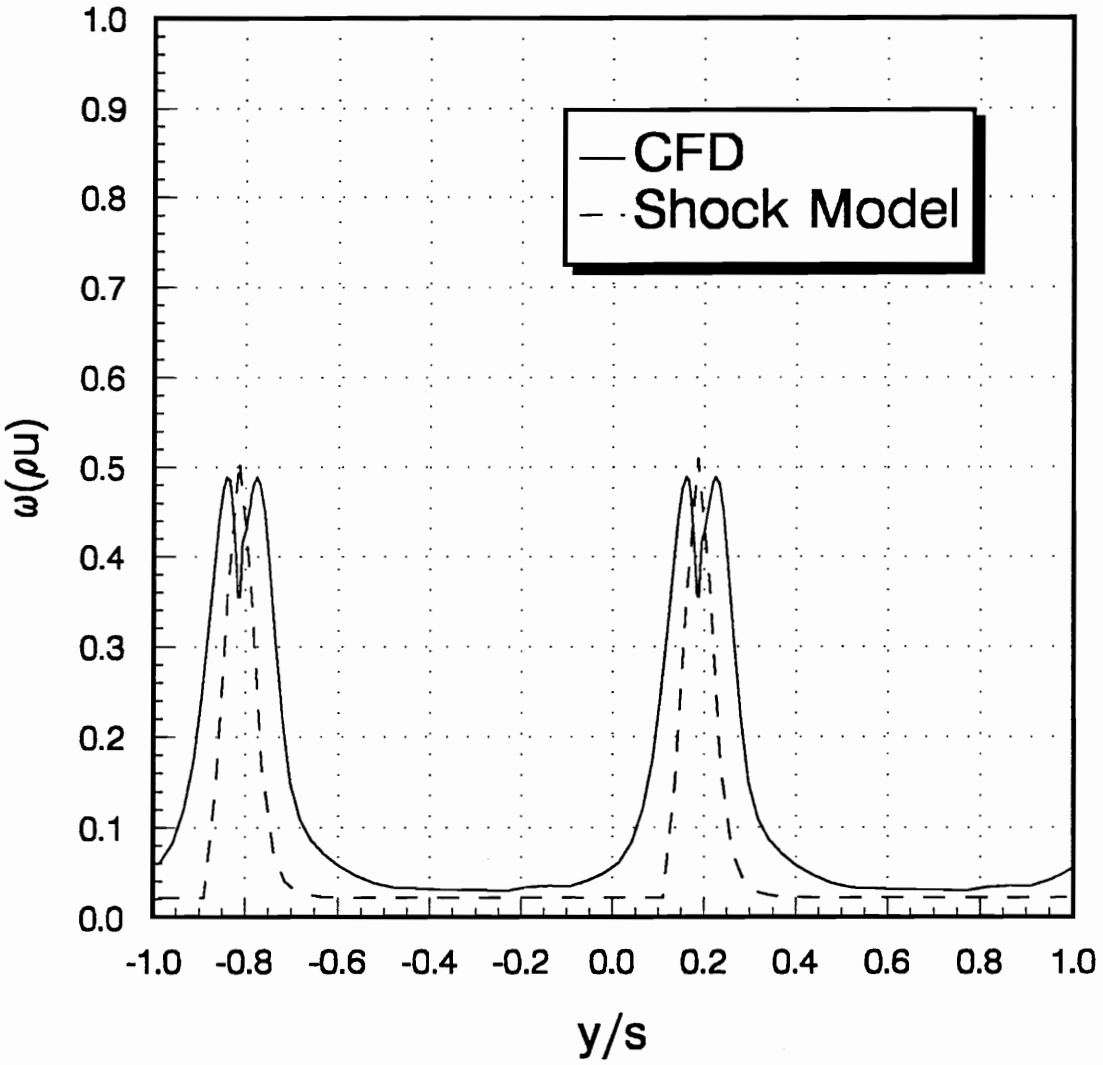

Figure 36. Mass Flux Weighted Loss Profiles at Design Incidence

Table 6. Losses From Leading Edge Bluntness

i	ϖ_b
-10°	0.032
-5°	0.036
0°	0.036
+5°	0.035

The losses from the leading edge shocks can be determined from the inviscid profiles in Figure 35 by first integrating the quantity $p_{t2}(\rho u)_2/(\rho u)_1$ across the blade passage to obtain the mass-averaged total pressure, and then using Equation 4.3 to find the mass-averaged loss coefficient. The loss coefficient for sharp blades can be similarly determined, using the value of p_{t2}/p_{t1} at the center of the passage to calculate the mass-averaged loss coefficient. The loss contribution from the leading edge bluntness is then determined by subtracting losses for sharp blades from the losses generated by the blunt blades. The losses calculated using this method are listed in Table 6. They are also plotted in Figure 37 on top of the losses calculated using ANSERS. The losses from the leading edge bluntness vary little with incidence angle and range from 0.032 to 0.036. As can be seen in Figure 37, this is a significant fraction of the total losses. The bluntness losses range from 21% to 33% of the total losses; this from a leading edge radius of only 0.18 mm. Perhaps just as important as the magnitude of the leading edge bluntness loss is the fact that the loss shows up in the wake region — a region normally associated with viscous losses. Figure 37 shows that about 50% of the losses in the wake, losses that appeared to be viscous losses, are actually shock losses. The source of these losses was not apparent in either the experimental or CFD data.

It is evident that the loss accounting methods used for lower speed supersonic cascades

Table 7. Loss Sources in the STFF Cascade

i	Measured			Calculated		
	ϖ_2	ϖ_v	ϖ_s	ϖ_2	ϖ_v	ϖ_s
-10°	0.139	0.045	0.094	0.151	0.026	0.125
-5°	0.112	0.036	0.076	0.108	0.034	0.074
0°	0.114	0.040	0.074	0.110	0.036	0.074
5°	0.216	0.029	0.187	0.170	0.041	0.129

— described in Chapter 4 — are not valid in the supersonic through-flow fan cascade. Using those methods, it is calculated that the shock losses are 40% to 50% of the total losses. If the accounting is adjusted to reflect the substantial inviscid loss in the wake region, the loss distribution changes considerably. As shown in Table 7, Figure 38, and Figure 39, it is now apparent that shock losses are the major source of losses in the STFF cascade. Shock losses account for 70% to 80% of the total losses in the cascade. The modeling of the leading edge shocks has shown that the leading edge radius has a major effect on the losses in the STFF, and that ignoring the leading edge bluntness will cause any understanding of the loss generation mechanisms to be grossly in error.

When compared to conventional supersonic blading, the magnitude of the shock losses in the STFF is, at first, surprising. In subsonic axial supersonic cascades, a *normal* shock exists in the blade passage, and the shock losses range between 20% and 40% of the total. In the STFF cascade, all shocks are *oblique*, and yet the shock losses are about 70% to 80% of the total. This seemingly contradictory result is the consequence of three effects. The first two relate to the behavior of shocks in the STFF and the last one relates to the behavior of the boundary layer. First, at the high Mach numbers in the STFF blades, significant losses can be generated even by oblique shocks. Thus, the expectation that the normal shock in conventional supersonic blading

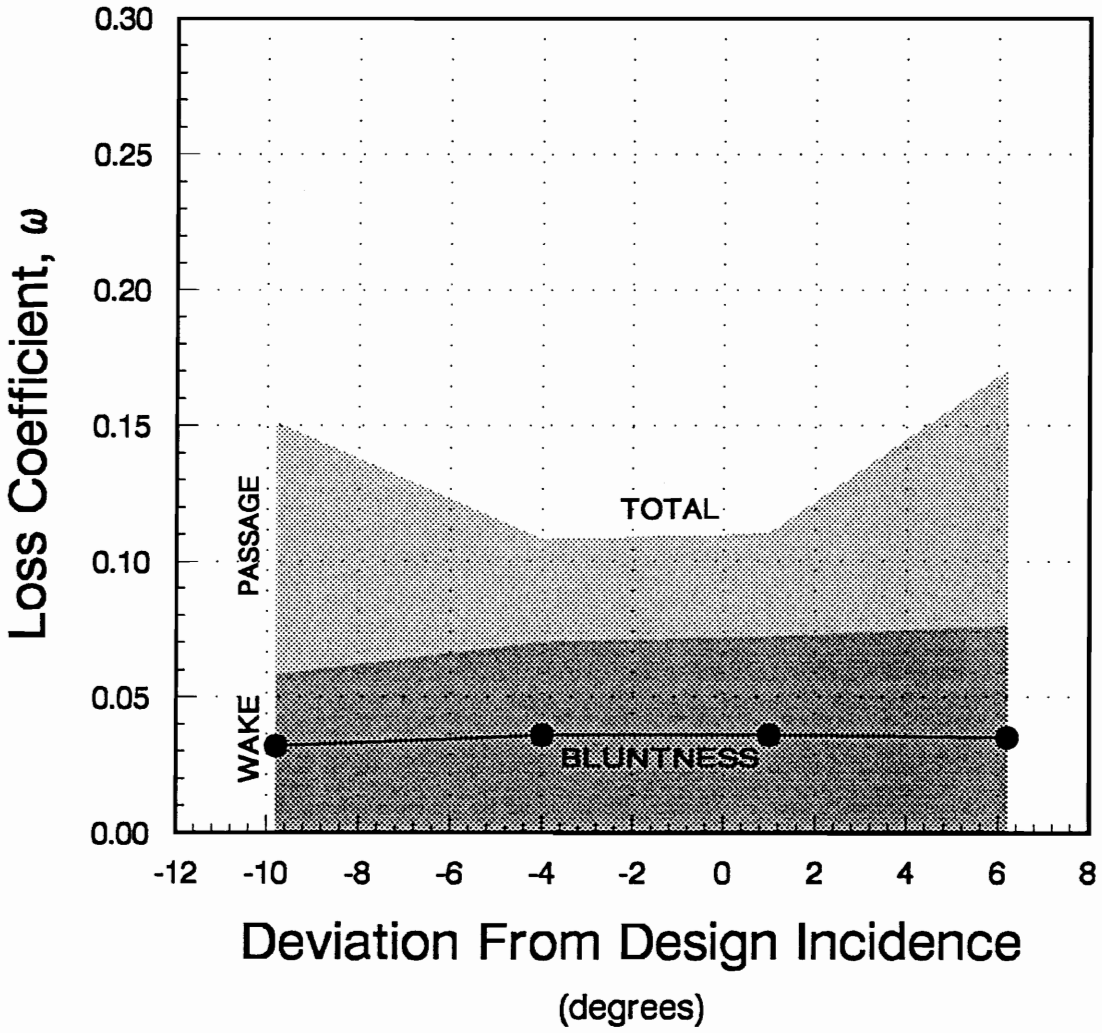

Figure 37. Leading Edge Bluntness Losses vs. CFD Losses

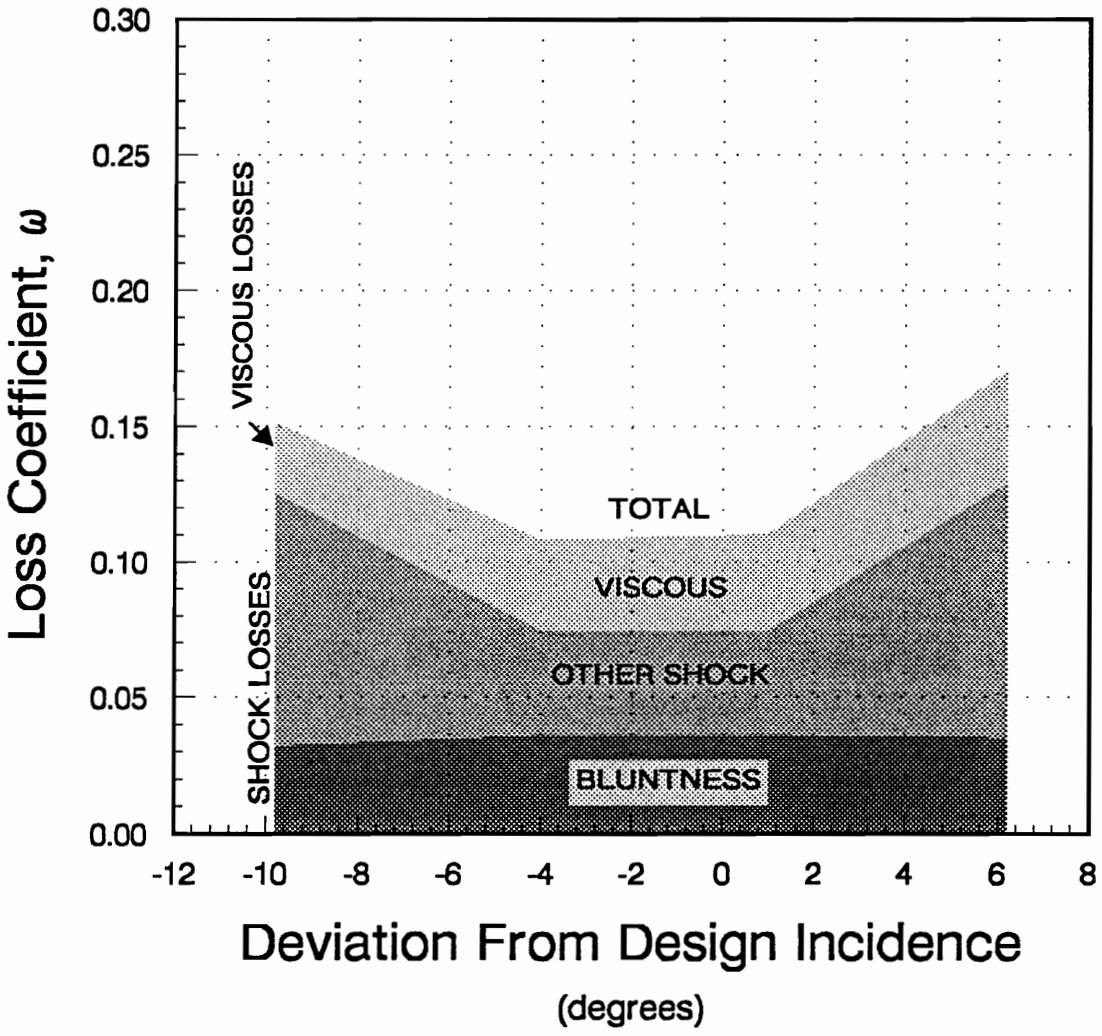

Figure 38. Loss Generation in the STFF Cascade, From CFD Results

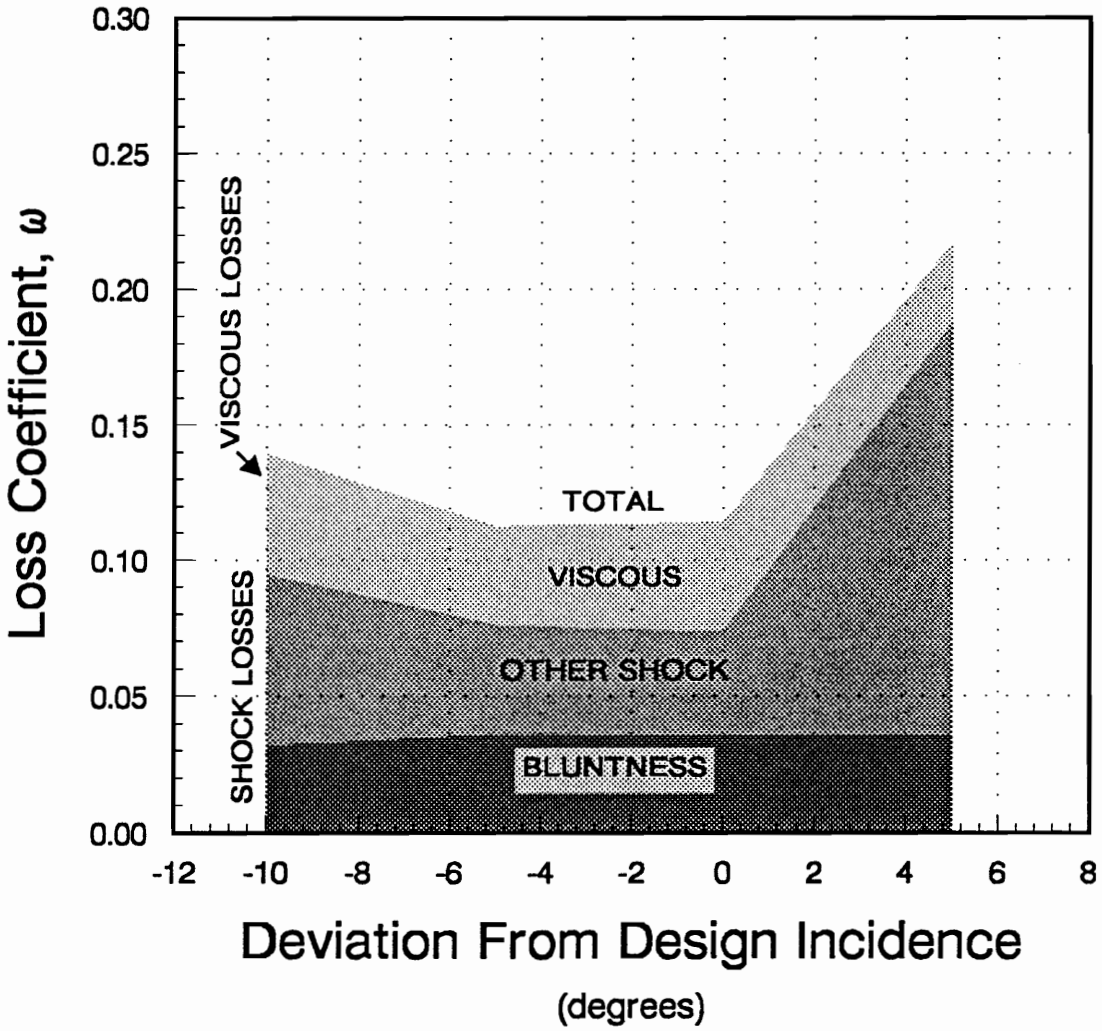

Figure 39. Loss Generation in the STFF Cascade, From Pitot/Static Data

will generate higher losses than the oblique shocks in these blades is not valid. Second, at the Mach numbers in the STFF, small departures from a sharp leading edge can cause large shock losses. The losses due to the leading edge bluntness are very small in subsonic axial blading. Finally, with the generally favorable pressure gradient in the blade passage, viscous losses are kept under control. When weak shocks intersect the boundary layer, the boundary layer does not separate. When stronger shocks do cause separation, the boundary layer quickly reattaches. In subsonic axial blading, the pressure gradient is adverse, and the boundary layer separates massively in the vicinity of the passage shock. The comparison to low Mach number supersonic blading can be misleading.

Chapter 7

Conclusions

The supersonic through-flow fan is a new and unproven technology. In an attempt to gain an understanding of the operation of this new type of compressor, a study has been conducted to thoroughly document the mean flow in a cascade of baseline STFF blades. Through a combination of flow visualization techniques, pressure probe measurements, and 2-D LDV measurements, a detailed picture of the flow physics and the loss mechanisms in a STFF has emerged.

Comparisons of the measured cascade data to numerical predictions made with a 2-D, finite volume CFD code show that the flow is predicted well at the design condition, but that off design, some discrepancies exist between the measured and calculated flow. The numerical solutions of the STFF cascade flow deviate from the measured flow due to the inability to adequately model the flow in regions of strong shock/boundary layer interaction. The discrepancies, however, are not large enough to greatly affect the integrated loss coefficients for the cascade, and the measured losses are well predicted by the numerical model at all incidence angles.

A simple model was developed to predict the losses from the leading edge shocks based on the detached shock model of Moeckel[14]. When the results of this model were combined with

the experimental and computational data, it became clear that shock losses were the major source of losses in the STFF cascade. The model shows that a small but finite leading edge radius can generate substantial losses in supersonic through-flow blading. In this cascade, the blades have a leading edge radius of only 0.18 mm and this leading edge bluntness accounts for up to 34% of the total losses. Because these losses are generated very close to the blade surface, they appear downstream in the wake region. In both the experimental and CFD data, the source of these losses is not apparent. Downstream of the blades, the leading edge bluntness losses are confounded with, and thus hidden by, the viscous losses.

Using the loss accounting techniques developed for lower speed supersonic blading, nearly all the losses in the wake region are attributed to viscous effects. Using those methods, one would come to the conclusion that shocks account for 35% to 55% of the total losses, depending on the incidence angle. The model developed here for the leading edge shock losses demonstrates that about 50% of the wake losses are actually due to inviscid effects. Using this information, it then becomes apparent that the shocks account for 70% to 80% of the total losses. The loss accounting techniques for subsonic axial, supersonic blading are clearly not applicable to supersonic through-flow blading.

The magnitude of the shock losses found in this cascade has important implications for the designers of future supersonic through-flow blading. It is clear that control of the shocks in a STFF has to be a top priority. The shape of the leading edge is particularly important in this respect. A sharp, thin leading edge will be needed to keep the shock losses to a minimum.

It should be remembered that, although the losses in this cascade are relatively high, these blade sections are from a *proof-of-concept* supersonic through-flow fan. These blades were not designed with high performance as the goal, but rather were designed somewhat conservatively. The primary objectives were to design a moderate performance fan that would demonstrate the

possibilities of supersonic through-flow blading, and would lead to a better understanding of the flow physics of supersonic through-flow fans. The cascade studies of these blades have shown that through better control of the shock losses, substantial improvements in the fan performance should be possible. These cascade studies have also shown that computational fluid dynamic codes are capable of accurately modeling the flow through well behaved blades. Thus, the direction is clear and the tools are available to proceed with higher performance supersonic through-flow fan designs.

Appendix A

Uncertainty Analysis

In order that the measurements presented in this paper can be properly interpreted, the following chapter is devoted to quantifying the measurement uncertainty for each of the measurement systems. For each instrument, the sources of measurement errors will be enumerated and quantified. If, for an individual measurement, multiple independent sources of uncertainty exist, the total uncertainty for that measurement will be assumed to be the square root of the sum of the squares of the individual uncertainties. If a quantity of interest, y, was not measured directly, but was calculated from the measured quantities, (x_1, x_2, x_3...x_n), the uncertainty in the measured quantities, w_i, will be assumed to be independent of one another, and the uncertainty in the calculated quantity, w_y, will be found from the following equation:

$$w_y = \sqrt{\sum_{i=1}^{n} \left(\frac{\partial y}{\partial x_i} w_i \right)^2} \qquad \text{(A.1)}$$

A.1 Blade Static Pressure

Uncertainty in the blade static pressure measurements comes from four sources: errors in the pressure measurement due to turbulence, errors in the pressure measurement due to tap geometry, errors in transducer calibration, and errors due to digitizing the transducer output. All reported blade static pressures are normalized by the settling chamber pressure, and so the error in the settling chamber pressure measurement is also a source of uncertainty.

From Goldstein[15], the pressure measured by a static pressure tap in a turbulent flow is approximately

$$p_{meas} = \bar{p} + \frac{1}{3}(\bar{p}_t - \bar{p})\overline{\left(\frac{V'}{V}\right)^2} \tag{A.2}$$

That is, in a turbulent flow, the measured static pressure will be higher than the true average static pressure. For 2% turbulent intensity at Mach 2.43, the error is approximately 0.6%.

The pressure taps on the instrumented blades were examined under a microscope to confirm that the holes were square and free of burrs. From Volluz[16], these taps should then indicate the static pressure within 0.1% of the dynamic head, or about 1% of the static pressure.

Calibration of the pressure transducer was estimated to be accurate to 0.3%. Signals from the transducer were digitized to 12 bit accuracy, therefore the errors from this source were minimal.

In the settling chamber, errors due to tap geometry were minimal due to the low speed of the flow. Errors arose primarily from the calibration of the transducer, and were estimated as

0.1%

Assuming all errors in measurement to be independent, the range of uncertainty for the blade static pressure measurements is approximately ±1.2%.

A.2 Pitot/Static Probe

When making measurements in the flow downstream of the cascade, the Pitot/static probe encountered widely varying conditions. Since the flow varied greatly across the passage, the uncertainty in the measurements varies as well. For this reason, the Pitot/static uncertainty is calculated for two flow conditions. The first condition of $M = 2.5$ with 1% turbulence was chosen as representative of the freestream. The second condition of $M = 1.75$ with 10% turbulence was chosen as representative of the wake. In the following analysis, the uncertainty in the Pitot and static measurements for the two flow conditions will first be quantified, and then the uncertainty in the derived quantities, M and p_t, will be calculated.

The Pitot tube portion of the Pitot/static probe was subject to errors from several effects. For these experiments, angle of the probe to the flow was less than 10°, and had a negligible effect on the measurement. The turbulence in the flow was approximately 1% in the freestream and 10% in the wake. From Goldstein[15], the pressure measured by a Pitot tube in a turbulent flow is approximately

$$p_{t\,meas} = \bar{p}_t + (\bar{p}_t - \bar{p})\overline{\left(\frac{V'}{V}\right)^2} \tag{A.3}$$

The error in the Pitot tube measurement due to turbulent effects was then negligible in the freestream and approximately 1% in the wake. Calibration of the pressure transducer was estimated to be accurate to 0.15%. Signals from the transducer were digitized to 12 bit accuracy, therefore the errors from this source were minimal.

Assuming all errors to be independent, the range of uncertainty for the Pitot pressure measurements is approximately ±0.15% in the freestream and ±1.0% in the wake.

Sources of errors in the two static pressure measurements were the same as those for the blade static pressure measurements with three additions: misalignment of the two plates with respect to one another, misalignment of the probe with respect to the flow, and 3-D effects.

For the freestream region of the downstream flow, the error due to turbulence is approximately the same 0.6% as for the blade static pressure. For the wake region, the error due to turbulence was approximately 1.5%. Errors due to tap geometry were again about 1% in the freestream and about 0.4% in the wake. Calibration errors were within 0.3%. The two plates were measured to be parallel within ±0.3°. A discrepancy of 0.3° would lead to an error of approximately 0.9% in the measured static pressure in the freestream and 0.1% in the wake. Probe pitch has little effect on the static pressure measurement. The yaw of the probe was estimated to no more than 2°, which would indicate that the error in the measured static pressure due to yaw of no more than 0.5% in the freestream and 0.1% in the wake.

As was noted in Chapter 3, the Pitot/static probe was designed for use in two-dimensional flows. When the flow has gradients in the third dimension, the three pressure measurements are

made at different flow conditions. As documented in Appendix B, there is some spanwise nonuniformity in the flow in this wind tunnel. The static pressure measurement is very sensitive to gradients in the third dimension. With the gradients shown in Appendix B, the error in the static pressure measurement was within approximately 7% in the freestream and 3% in the wake.

Assuming all errors to be independent, the range of uncertainty for the static pressure measurements is approximately ±7.4% in the freestream and ±3.4% in the wake. The uncertainty in the static pressure measurement is dominated by the three-dimensional effects.

The uncertainty in the Mach number measured with the Pitot/static probe is calculated from:

$$\frac{w_M}{M} = \sqrt{\left[\left(\frac{\partial M}{\partial p_p}\frac{p_p}{M}\right)\left(\frac{w_{p_p}}{p_p}\right)\right]^2 + \left[\left(\frac{\partial M}{\partial p}\frac{p}{M}\right)\left(\frac{w_p}{p}\right)\right]^2} \qquad \text{(A.4)}$$

Since Equation 3.1 is not explicit in M, the derivatives in the above equation are not easily calculated, and so were evaluated numerically. When the above uncertainties were inserted into this equation, the uncertainty in M was calculated to be ±3.7% in the freestream and ±2.0% in the wake.

The uncertainty in the total pressure measured with the Pitot/static probe is calculated from:

$$\frac{w_{p_t}}{p_t} = \sqrt{\left[\left(\frac{\partial p_t}{\partial p_p}\frac{p_p}{p_t}\right)\left(\frac{w_{p_p}}{p_p}\right)\right]^2 + \left[\left(\frac{\partial p_t}{\partial p}\frac{p}{p_t}\right)\left(\frac{w_p}{p}\right)\right]^2} \qquad \text{(A.5)}$$

Once again, the derivatives are awkward, and so were evaluated numerically. When the above uncertainties in p_p and p were inserted into this equation, the uncertainty in p_t was calculated to be ±7.4% in the freestream and ±2.3% in the wake.

Table 8. Simplified Downstream Profile

	Core	Wake
p_{t2}/p_{t1}	0.95	0.40
$(\rho u)_2/(\rho u)_1$	0.90	0.50
$\Delta y/s$	0.80	0.20

In estimating the uncertainty in the mass-averaged loss coefficient, ϖ, it was necessary to make some assumptions about the error. It was first assumed that in calculating a mass-averaged total pressure, $\bar{p}_t$, from the individual pressure measurements, the integration did not decrease the uncertainty. That is, errors in p_t were not assumed to be random. It was then assumed that the uncertainty in the mass-averaged total pressure could be approximated by examining the uncertainty in the simplified freestream/wake profile described in Table 8. In this simple stairstep profile the uncertainties in the wake and freestream were assumed to be those calculated above. The uncertainty in the mass-averaged total pressure was then calculated by mass averaging the total pressure uncertainty. The result of this procedure is that the uncertainty in $\bar{p}_t$ is approximately ±7.1% and the uncertainty in ϖ is approximately ±0.068. Since ϖ is

approximately 0.15, this uncertainty is undeniably large. It is an unfortunate reality that total pressure is difficult to measure with precision at high Mach numbers. It is also the nature of the loss coefficient, which is approximately 1 - $\bar{p}_t$ for high Mach numbers, that small uncertainties in total pressure lead to large uncertainties in the loss coefficient. These two realities lead inevitably to high uncertainties in ϖ.

A.3 LDV

For the LDV system, uncertainty in the velocity measurement arose primarily from three sources: uncertainty in the frequency measurement due to the finite resolution of the counter output, uncertainty in the velocity mean due to finite sample size in a turbulent flow, and uncertainty in the frequency/velocity calibration due to uncertainty in the beam half angle, κ. The first two of these errors are minimized as the number of data points becomes large. The uncertainty in κ, however, is a systematic error, and is not affected by averaging. With 1024 data points at each measurement position, the uncertainty in the beam half angle, κ, predominates. For both the blue and green beams, κ was approximately 2°, and was measured with an optical protractor to ±2 minutes. This leads to an uncertainty in the velocity magnitude of 1.2% in the freestream and ±1.3% in the wake. When the velocity uncertainty is combined with a 0.5° uncertainty in the alignment of the LDV system relative to the wind tunnel, an uncertainty in the flow direction of 0.9° is calculated.

In supersonic flows, the quantity of interest is typically not the velocity, but the Mach number. To obtain the Mach number, the temperature of the flow must be known as well. In the STFF cascade, the total temperature of the flow, T_t, was measured upstream of the nozzle to

±0.5°K (±0.02%). When the total temperature and velocity of the flow are known, the Mach number can be obtained with the following relation:

$$M = \left[\frac{\gamma R T_t}{V^2} - \frac{\gamma - 1}{2} \right]^{-1/2} \tag{A.6}$$

The uncertainty in the Mach number, w_M, can then be expressed in terms of the uncertainties in V and T_t as:

$$w_M = \sqrt{\left(\frac{\partial M}{\partial V} w_V \right)^2 + \left(\frac{\partial M}{\partial T_t} w_{T_t} \right)^2} \tag{A.7}$$

When the appropriate partial derivatives of Equation A.6 are inserted into Equation A.7, the uncertainty in the Mach Number becomes:

$$\frac{w_M}{M} = \left(1 + \frac{\gamma - 1}{2} M^2 \right) \sqrt{\left(\frac{w_V}{V} \right)^2 + \left(\frac{1}{2} \frac{w_{T_t}}{T_t} \right)^2} \tag{A.8}$$

The important thing to note about Equation A.8 is that as the Mach number becomes large, the uncertainty in the Mach number becomes large compared to the uncertainty in the velocity. The reason for the greater uncertainty is that in calculating the Mach number, the

velocity can be thought of as being used twice: first in the direct proportionality of Mach number to velocity and second in the calculation of static temperature used to calculate the local speed of sound. If the uncertainty in the total temperature is small compared to the uncertainty in the velocity, as it was in this experiment, the uncertainty in the Mach number is approximately twice the uncertainty in the velocity for a Mach number of 2.2. The uncertainty in the Mach number for this experiment was then ±2.6% in the freestream and ±1.7% in the wake.

When the velocity and total temperature measurements are combined with a Pitot pressure measurement, it is possible to calculate the total pressure of the flow. With the Mach number calculated as above, the total pressure is calculated from

$$p_{t_2} = p_{p_2}\left[\frac{(\gamma+1)M^2}{(\gamma-1)M^2+2}\right]^{-\frac{\gamma}{\gamma-1}}\left[\frac{\gamma+1}{2\gamma M^2-(\gamma-1)}\right]^{-\frac{1}{\gamma-1}} \tag{A.9}$$

The uncertainty in the total pressure is then

$$\frac{w_{p_t}}{p_t} = \sqrt{\left(\frac{w_{p_p}}{p_p}\right)^2+\left[\left(\frac{\partial p_t}{\partial T_t}\frac{T_t}{p_t}\right)\left(\frac{w_{T_t}}{T_t}\right)\right]^2+\left[\left(\frac{\partial p_t}{\partial V}\frac{V}{p_t}\right)\left(\frac{w_V}{V}\right)\right]^2} \tag{A.10}$$

When the derivatives in the above equation were evaluated, and the uncertainties in p_p, V and T_t were inserted into this equation, the uncertainty in p_t was calculated to be ±5.4% in the freestream and ±2.4% in the wake.

The uncertainties in the Pitot/static and LDV measurements downstream of the cascade

Table 9. Uncertainty Analysis, Summary

	Freestream		Wake	
	Probe	LDV	Probe	LDV
M	±3.7%	±2.6%	±2.0%	±1.7%
p_t	±7.4%	±5.4%	±2.3%	±2.4%
V	–	±1.2%	–	±1.3%
β	–	±0.9°	–	±0.9°

are summarized in Table 9.

Appendix B

Test Section Flow Quality

B.1 Upstream Flow

Probe traverses were made at several locations upstream of the cascade to document the flow at the inlet of the blade passage. The upstream Mach number is plotted at five locations — from -25 to +25 mm in the flow direction and from -13 to +13 mm across the span of the blades — in Figure 40. The x, y, and z-directions are as shown in Figure 3. From Figure 40, it can be seen that the upstream Mach number is 2.36 ± 0.05. The freestream turbulence intensity, as measured by Bowersox[9] using the hot wire technique, was approximately 1%.

From these measurements, the total pressure can also be calculated. These total pressure measurements are plotted in Figure 41. From this figure it can be seen that there is some variation in the measured upstream total pressure, and that the average of the total pressure measurements upstream of the cascade is 0.96 times p_{t0}, the settling chamber pressure. This plot indicates that either something is causing a total pressure loss through the nozzle or that a systematic bias exists in the probe measurement of the total pressure.

If the total pressure measurements are correct, there are two mechanisms that could create losses in the nozzle. The first mechanism is for there to be incomplete expansion through the

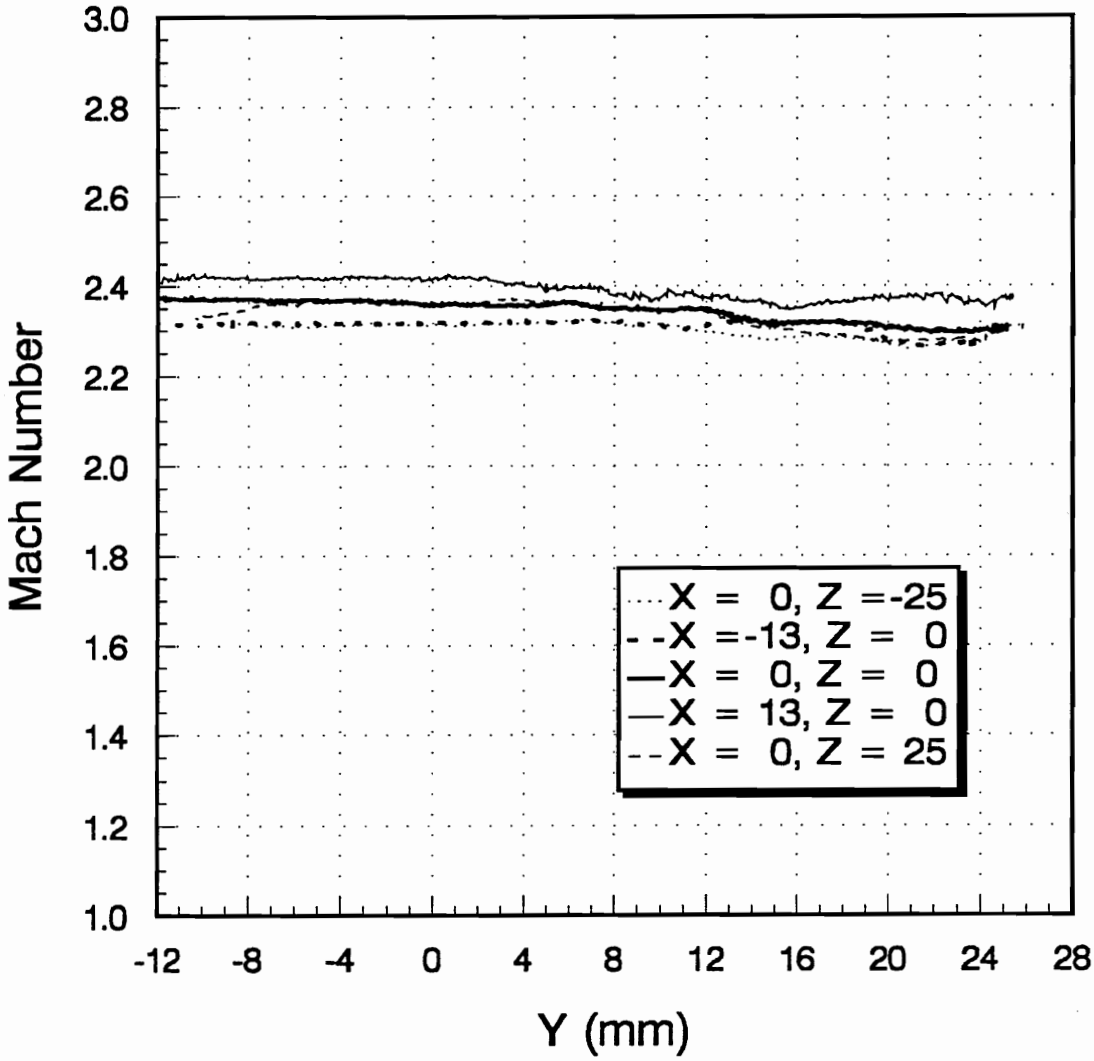

Figure 40. Measured Upstream Mach Number

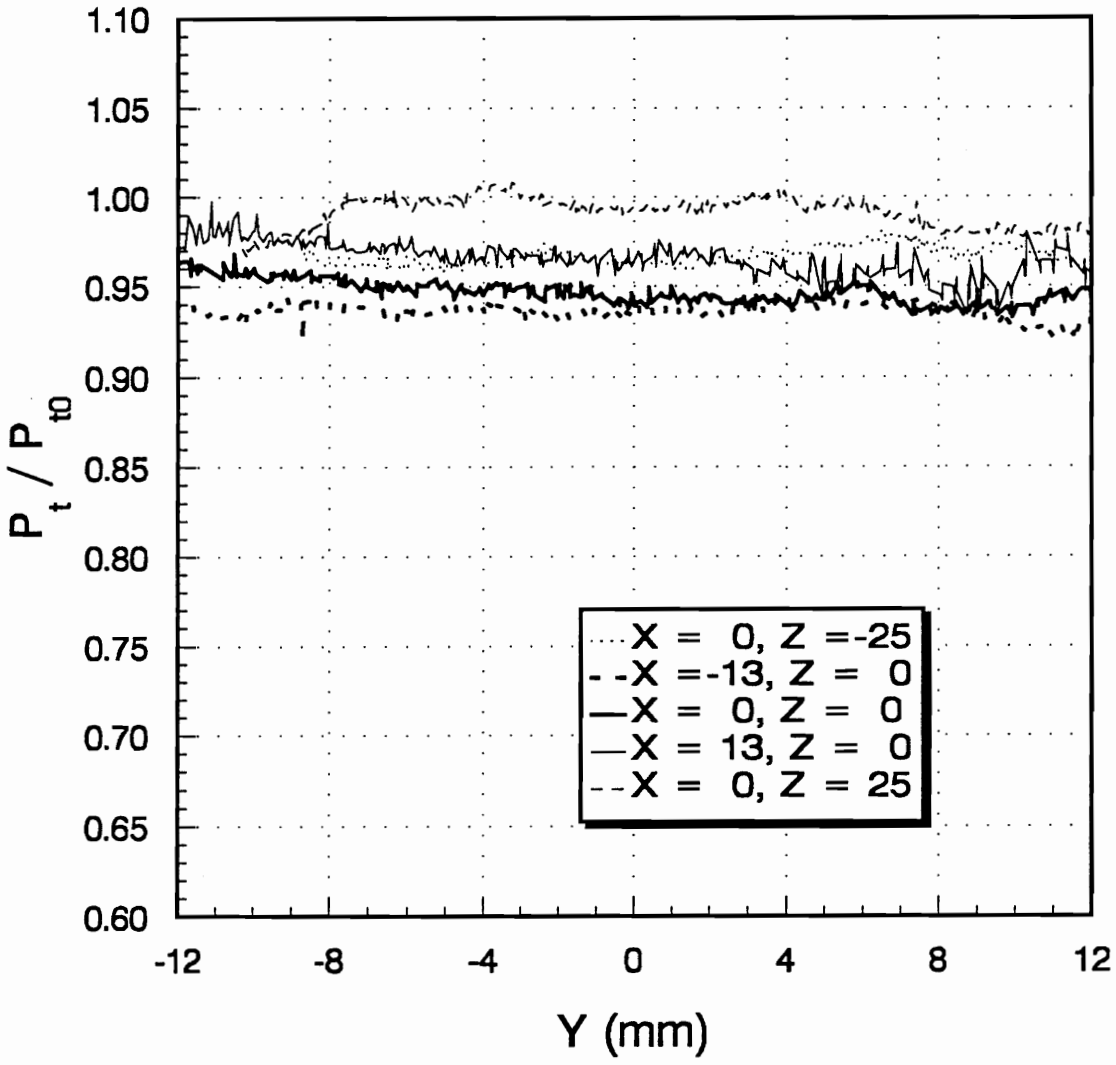

Figure 41. Measured Upstream Total Pressure

nozzle, thus causing shocks to exist in the nozzle. If this were the case, the shocks could be eliminated by increasing the settling chamber pressure. Increasing the settling chamber pressure was attempted and was found to have no effect on the measured total pressure. The other possible mechanism which could cause a total pressure drop in the nozzle is for there to exist strong condensation shocks in the nozzle.

Condensation shocks are complicated phenomena which exist in supersonic nozzles when there is sufficient moisture in the supply air. As the air passes through the nozzle, the temperature drops, and the saturation pressure of water vapor drops as well. The drop in the saturation pressure is greater than the drop in the air pressure, so if the moisture content is high enough, the air can become supersaturated with water. The moisture will then eventually condense very suddenly in a condensation shock. Wegener and Mack[17] have shown that for Mach numbers above 2, virtually impossible levels of dryness are needed to prevent a condensation shock from forming in a supersonic wind tunnel. However, they also showed that for achievably low levels of humidity, the effects of a condensation shock will be negligible. The moisture content of the supply air for the VPI supersonic cascade tunnel was measured with a EG&G Model 911 dewpoint hygrometer and found to be 0.334 g H_2O per kg of dry air. This level of humidity is sufficient only to cause a total pressure drop of, at most, 0.6%. The effect on the Pitot/static probe measurement of total pressure, however, would be greater. In a supersonic wind tunnel, a Pitot pressure measurement is almost totally insensitive to humidity, since any water that condensed in the nozzle will generally re-vaporize passing through the shock in front of the Pitot tube. No shock exists at a static pressure tap to re-vaporize the water, and the measured static pressure in a humid tunnel will be lower than that measured in a dry tunnel. Because a condensation shock does not affect the Pitot and static pressures equally, the total pressure measured with a Pitot/static probe in a flow in which condensation has occurred will be lower

than the true total pressure. For the humidity level measured in this wind tunnel, the total pressure measured by the Pitot/static probe should be no lower than $0.985 \times p_{t0}$. It is therefore concluded that no identifiable mechanisms exist which could cause the total pressure loss measured through the nozzle.

It is not clear, then, what causes the measured loss through the nozzle. It is possible that mechanisms which have not yet been identified are causing a loss in the nozzle. It is also possible that the probe systematically measures the total pressure to be lower than the true value. In either case, it makes sense to make all calculations of the downstream conditions assuming that $p_{t1} = 0.96 \times p_{t0}$, since in either case, the same mechanisms which affect the upstream measurements will affect the downstream measurements. For this reason, all pressure measurements in this paper are normalized by the nominal value of p_{t1}, $0.96 \times p_{t0}$.

B.2 Two-Dimensionality

To asses the two-dimensionality of the cascade flow, Pitot probe traverses were made downstream of the cascade off the tunnel centerline. The results of these measurements are shown in Figure 42. Measurements were obtained at 0 and ± 13 mm from the centerline. The figure indicates that the downstream flow is two-dimensional to the same extent as the upstream flow. Observation of oil streaks on the blade surfaces verified that disturbances created by the endwall boundary layer growth did not propagate to the center of the passage.

B.3 Periodicity

To asses the blade-to-blade variation of the cascade flow, Pitot probe traverses were made across adjacent blade wakes. The results of these measurements showed only slight aperiodicity in the downstream flowfield, as shown in Figure 43. The cascade was checked for variation in stagger and blade to blade spacing. None was found. It was then concluded that this slight aperiodicity results from the small non-uniformities in the upstream flow.

B.4 Repeatability

Experiments in the STFF cascade were performed in stages, with several months sometimes separating each stage of the program. In between these stages, the cascade test section was removed from the wind tunnel and disassembled. Figure 44 shows that this procedure did not influence the cascade measurements. The two Pitot profiles shown in this figure were generated several months apart, after the cascade test section had been taken apart and reassembled.

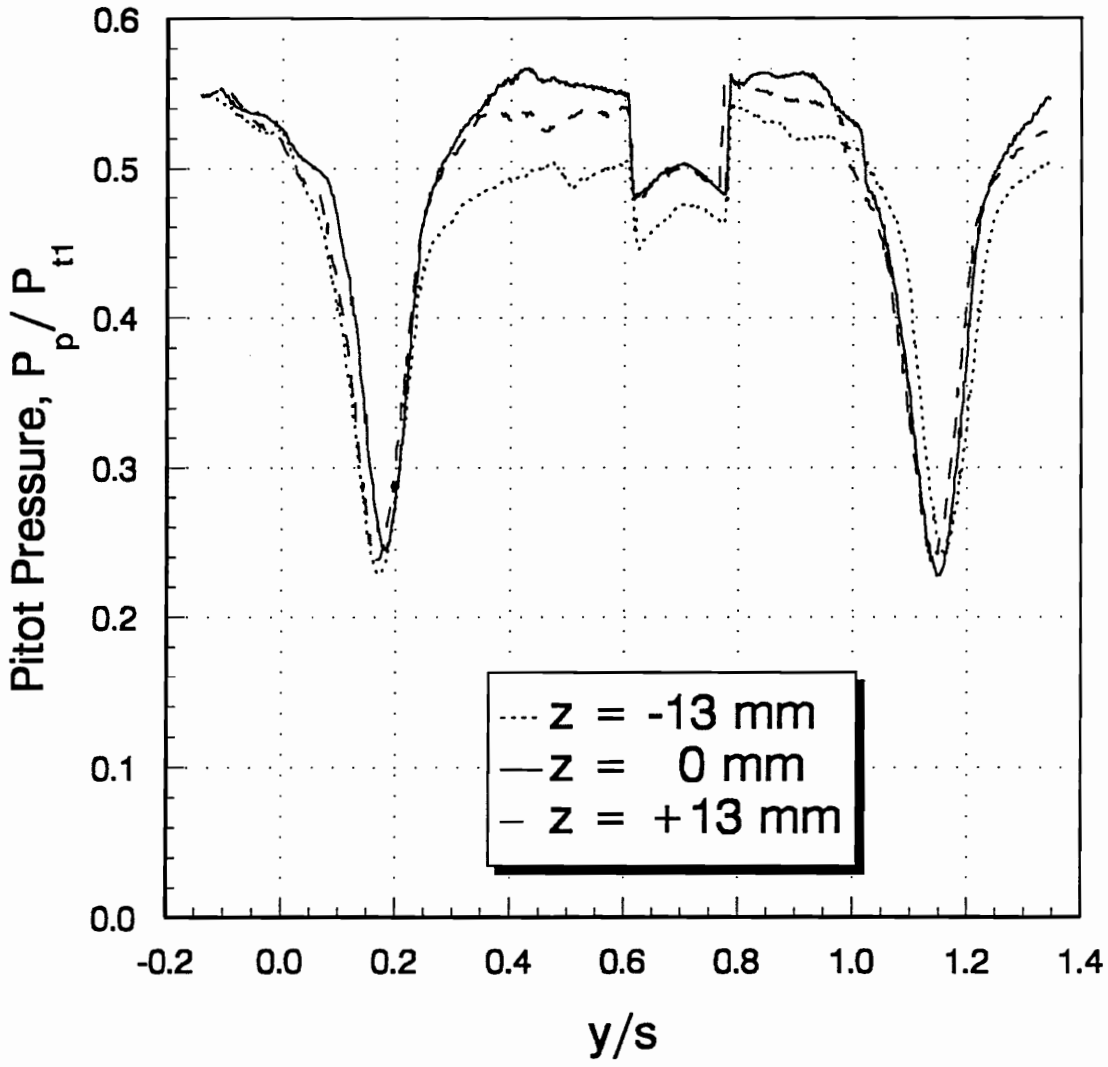

Figure 42. Downstream Two-Dimensionality (Pitot Pressure)

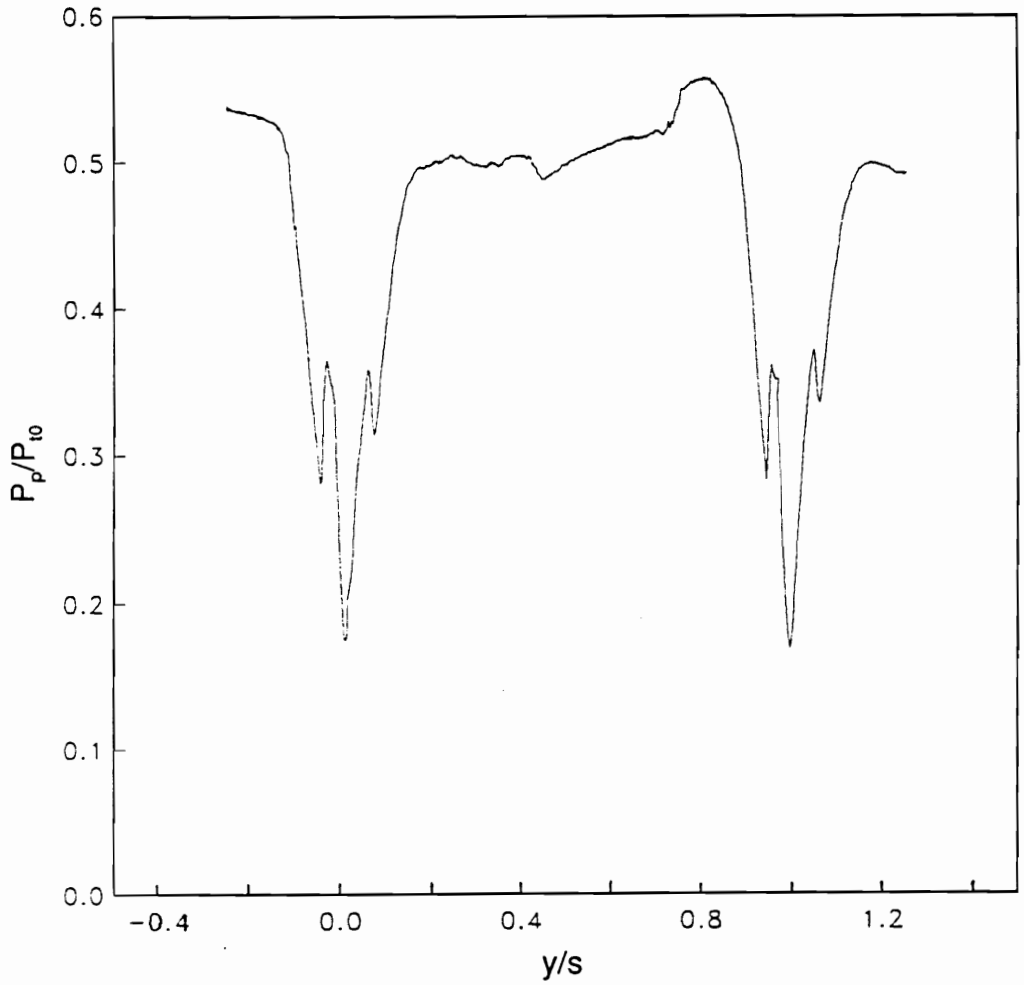

Figure 43. Downstream Periodicity (Pitot Pressure)

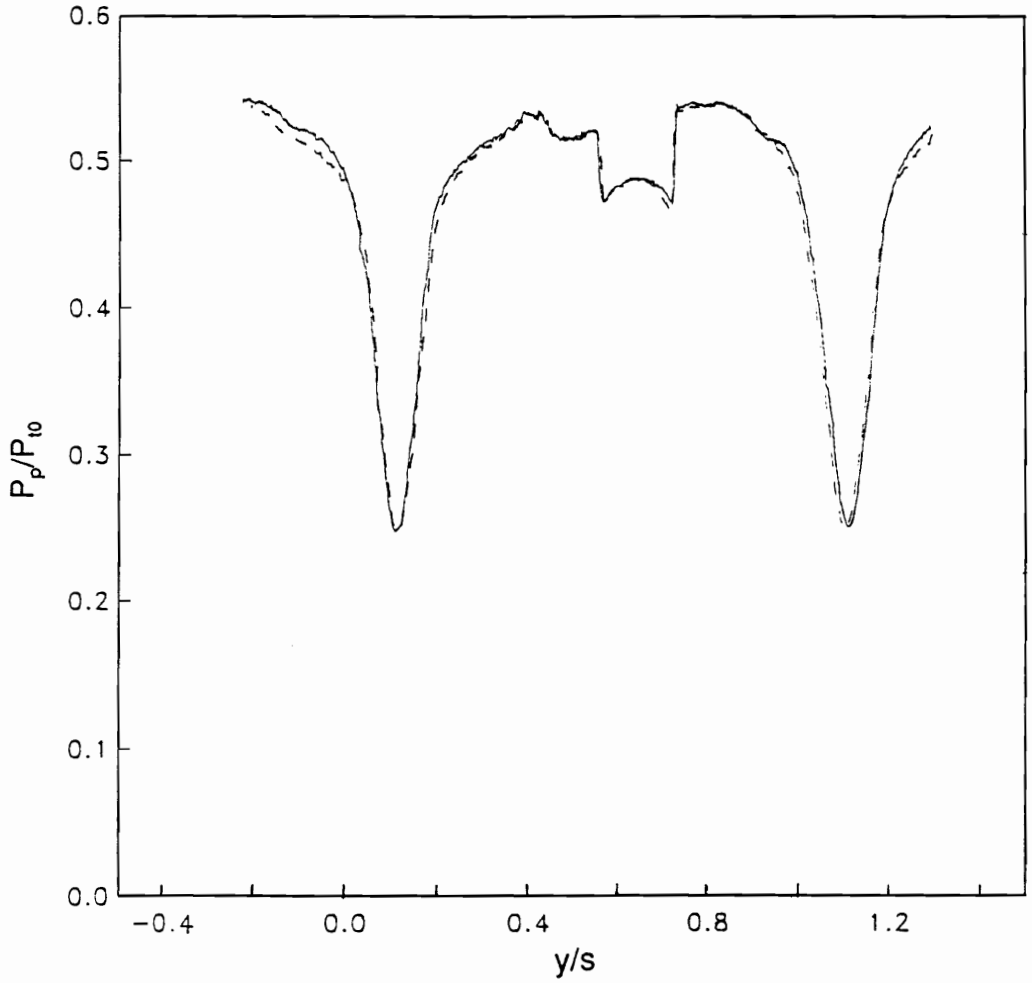

Figure 44. Flow Repeatability (Pitot Pressure)

Appendix C

Particle Lag Analysis

A test was performed to experimentally determine the lag of the seed particles in the supersonic through-flow cascade. In this appendix, the test will be described, and the results of this testing will be presented. Several particle drag models will be presented, and the models will be examined for their suitability for the prediction of particle lag in supersonic flows in light of the experimental results. The particle lag through the supersonic through-flow fan blade cascade will be estimated using an empirical particle drag model to predict the behavior of a particle traveling through the CFD generated STFF cascade flowfield.

C.1 Background

Perhaps the most significant limitation of the LDV when used in high speed flows is that the system measures not the velocity of the fluid, but rather the velocity of particles suspended in the fluid. These are usually particles introduced into the flow specifically for LDV measurements. To ensure adequate signal to noise ratio, these particles should be made large. To ensure that these particles will adequately follow the flow, these particles should be made

small. For low speed applications it is not difficult to find particles which will meet both these criteria. However, for supersonic flows, where particle residence time in the measurement volume is small and velocity gradients are very large, compromise in meeting these criteria is inevitable.

Care must be taken to ensure that the ability of the particles to follow the flow is not compromised too much. While it is theoretically possible to calculate the flow velocity given knowledge of the motion of a lagging particle, to make this calculation both the velocity and acceleration of the particle must be accurately known. Acceleration of the particle can only roughly be inferred from discrete velocity measurements of finite accuracy. Therefore, as a practical matter, velocity measurements made on lagging particles cannot be corrected to obtain the velocity of the flow[18]. When making measurements with an LDV, then, it must always be assumed that the particles follow the flow with a reasonable degree of fidelity. It is therefore important to have a good model of particle response in order that validity of this assumption may be justified.

At the present time there are several models available for predicting the drag of spherical particles. However, for the range of flow conditions which may be encountered by supersonic LDV seed particles — compressible, rarefied flow with Reynolds numbers below 50 — these models have not been experimentally verified. Out of necessity, these models are still frequently used in particle lag studies. Samimy and Abu-Hijleh[19], for example, used the model of Walsh[20] to infer the size distribution of polydisperse oil droplets based on the lag of these particles through an oblique shock. Maxwell and Seaholtz[21] used the model of Carlson and Hoglund[22] to examine the behavior of small particles passing through a Mach 1.6 normal shock and in flow with a sinusoidally varying velocity.

For the supersonic through-flow fan blade cascade studies, an analysis of particle drag was undertaken which did not rely solely on unverified particle drag models. The particle lag was first

evaluated theoretically using a variety of particle drag models, and then the particle lag in a simple representative supersonic flowfield was measured and used to evaluate the suitability of the drag models to the STFF flowfield.

C.2 Particle Lag Experiment

In order to obtain a clear measure of the particle lag in the STFF, a sharp edged flat plate was placed in the VPI Mach 2.4 supersonic cascade wind tunnel inclined at 10° to the flow. The oblique shock generated for this experiment was chosen to be representative of the largest flow gradients in the STFF cascade. The oblique shock generated a flow with a step velocity profile, through which the velocity of particles moving with the flow was measured using the two-dimensional LDV system described in Chapter 3. For these measurements, the system was oriented to measure velocity components at plus and minus 45° to the freestream. After the shock, the flow was at 35° to the blue component and 55° to the green. The experimental flowfield and the directions of the measured velocity components are illustrated in Figure 45.

In order to discern the effect of particle size on lag, two sizes of PSL spheres were used: 0.6 μm and 1.5 μm. 0.24 μm particles were available, but proved to be unsuitable for this application due to the low levels of scattered light.

C.3 Particle Lag Modeling

The equation of motion for a single spherical particle moving in an infinite, viscous fluid

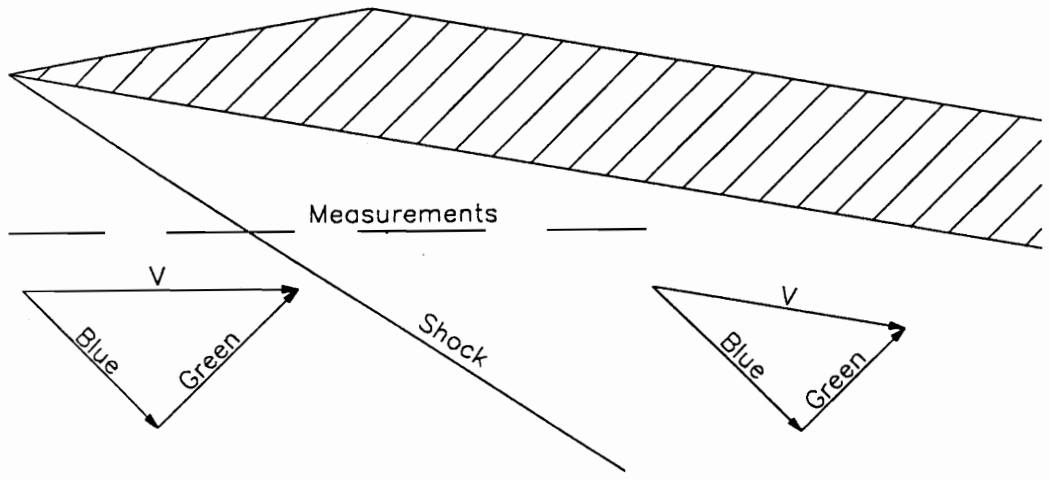

Figure 45. Lag Experiment Flowfield and Velocity Components

and not subject to external force fields from Hjelmfelt and Mockros[23] is:

$$\frac{\pi d^3}{6}\rho_p\frac{dV_p}{dt} = C_D\rho_f\frac{\pi d^2}{8}(V_f-V_p)^2 + \frac{\pi d^3}{6}\rho_f\frac{dV_f}{dt} + \frac{1}{2}\frac{\pi d^3}{6}\rho_f\left(\frac{dV_f}{dt}-\frac{dV_p}{dt}\right) + \frac{3}{2}d^2\rho_f\sqrt{\pi\nu}\int_{t_0}^{t}\frac{\frac{dV_f}{d\xi}-\frac{dV_p}{d\xi}}{\sqrt{t-\xi}}\,d\xi \qquad \text{(C.1)}$$

where d is the particle diameter, V represents velocity, ν is kinematic viscosity, ρ is density, the subscript f represents fluid, and p represents particle. The first term on the left-hand side is the force required to accelerate the particle. The term on the right-hand side is the steady-state viscous drag force, based on a coefficient of drag, C_D. The second term is due to the pressure gradient within the fluid surrounding the particle that arises from the acceleration of the fluid. The third term, known as the apparent mass, is the force required to accelerate the mass of fluid surrounding and moving with the particle. This term is viewed as an addition to the inertia of the particle and is taken to be proportional to one-half the mass of the displaced fluid. The last term, known as the Basset history integral, accounts for the deviation of the flow from steady-state over a period from time t_0 to the present time t. The Basset term becomes significant when the particle is accelerated at a high rate.

When the flow is steady with gradually changing properties, or when ρ_p is much greater than ρ_f — as when solid particles are suspended in air — Hjelmfelt and Mockros[23] showed that the pressure gradient, apparent mass, and Basset integral terms could be neglected. Thus Equation C.1 becomes:

$$\frac{\pi d^3}{6}\rho_p\frac{dV_p}{dt} = C_D\rho_f\frac{\pi d^2}{8}(V_f - V_p)^2 \qquad \text{(C.2)}$$

If the mass fraction of particles in the suspension is small, as is typically the case in LDV applications in air, Maxwell and Seaholtz[21] showed that Equation C.2 becomes unlinked from the particle energy equation and can be solved independently. This equation can then easily be integrated to find the particle motion through a given flowfield once an expression for the coefficient of drag is given. For the conditions typically experienced in supersonic LDV applications, however, the model one should use for C_D is not generally agreed upon.

For most subsonic flows, the Stokes flow coefficient of drag, given by:

$$C_D = \frac{24}{Re} \qquad \text{(C.3)}$$

where Re is the relative particle Reynolds number based on diameter, is an adequate model. The Stokes drag model is supported by both strong theoretical and experimental evidence. However, the formula is only applicable to incompressible, continuum flows of low Reynolds number (less than about 1). For supersonic LDV applications, none of these conditions may apply.

To extend the Stokes drag formula, many high Reynolds number "correction factors" to Equation C.3 have been empirically derived. White[24] suggests that:

$$C_D = \frac{24}{Re} + \frac{6}{1+\sqrt{Re}} + 0.4 \qquad \text{(C.4)}$$

This equation extends the usefulness of the Stokes drag formula to Reynolds numbers of 250,000 but still retains the incompressible continuum assumption.

When the mean free path of the fluid molecules, λ, becomes significant compared to the diameter of the particles, the fluid can no longer be treated as a continuum. The parameter determining whether or not the fluid is a continuum, the Knudsen number, is defined as:

$$Kn = \frac{\lambda}{d} \qquad \text{(C.5)}$$

When Kn is of the order 1 or larger, the gas is no longer considered to be a continuum. From kinetic theory, the mean free path length for a gas can be computed from:

$$\lambda = \frac{\mu}{p}\sqrt{\frac{\pi R T}{2}} \qquad \text{(C.6)}$$

By combining Equations C.5 and C.6 with the definitions of the relative Mach and Reynolds numbers for the particle, a more convenient formulation of the Knudsen number is found to be:

$$Kn = \sqrt{\frac{\pi\gamma}{2}}\ \frac{M_r}{Re} \tag{C.7}$$

This indicates that when the Reynolds number is high and the relative Mach number is low, as it is for large objects in low speed flows, the Knudsen number is low and the fluid can be considered to be a continuum. When the relative Mach number is high and the Reynolds number is low, as it is for small particles in high speed, low pressure flows, the Knudsen number can become large and the fluid must be considered to be rarefied. Millikan[25] showed that for a rarefied gas, the coefficient of drag is reduced compared to that for a continuum by:

$$C_D = \frac{24}{Re}\left[\frac{1}{1 + 2Kn\left(A + Be^{-C/2Kn}\right)}\right] \tag{C.8}$$

where A, B, and C are all positive constants.

Carlson and Hoglund[22], in an attempt to develop a particle drag model which accounted for the combined effects of viscosity, inertia, rarefaction, and compressibility developed the following equation:

$$C_D = \frac{24}{Re}\left[\frac{\left(1 + 0.15\,Re^{0.687}\right)\left(1 + \exp\left(-0.427/M_r^{4.63} - 3/Re^{0.88}\right)\right)}{1 + M_r/Re\left(3.82 + 1.28\exp\left(-1.25\,Re/M_r\right)\right)}\right] \qquad \text{(C.9)}$$

This equation was obtained from the Stokes drag formula modified by three terms. The first term in the numerator is the inertia correction of Torobin and Gauvin[26] used to extend the equation to higher Reynolds numbers. The second term in the numerator is a correction for compressibility effects based on data presented by Hoerner[27]. The denominator is Millikan's Equation C.8 with the constants determined by the Mach 0.5 data of Stadler and Zurick[28]. Equation C.9 was later used by Maxwell and Seaholtz[29] to analyze the motion of particles through a normal shock.

Walsh[20] analyzed Equation C.9 in light of more recent particle drag data and found it to be inaccurate at relative Mach numbers much different than 0.5. Walsh also examined several other particle drag models and found all of them to be accurate only over limited ranges. He then developed a new model to fit the experimental data. Starting with the model of Cuddihy, Beckwith, and Schroeder[30], Walsh adjusted the constants of the model so that the best fit of the data was obtained. Walsh found the coefficient of drag for a solid spherical particle to be:

$$C_D = C_{Dc} + (C_{Dfm} - C_{Dc})\exp\left[-A\,Re^N\right] \qquad \text{(C.10)}$$

The coefficients A, N, and $C_{D\,c}$ are empirically derived functions of the particle relative Mach number and are tabulated in Table 10. $C_{D\,fm}$ is the free molecular coefficient of drag for diffuse reflection of molecules given by Emmons[31] as:

Table 10. Walsh Model Coefficients

M_r	$C_{D\,fm}$	A	N
0.10	0.380	1.7269	0.1976
0.15	0.381	1.4099	0.2196
0.20	0.390	1.1908	0.2399
0.25	0.392	1.0339	0.2562
0.30	0.398	0.9144	0.2706
0.35	0.403	0.8159	0.2846
0.40	0.410	0.7356	0.2973
0.45	0.419	0.6672	0.3097
0.50	0.426	0.6085	0.3215
0.55	0.435	0.5637	0.3301
0.60	0.443	0.5244	0.3384
0.65	0.453	0.4890	0.3467
0.70	0.466	0.4602	0.3536
0.75	0.480	0.4367	0.3585
0.80	0.500	0.4163	0.3630
0.85	0.513	0.4043	0.3620
0.90	0.540	0.3909	0.3631
0.95	0.600	0.4735	0.3096
1.00	0.710	0.4384	0.3086
1.10	0.780	0.4332	0.3059
1.20	0.820	0.4261	0.3036
1.30	0.860	0.4252	0.3003
1.40	0.890	0.4260	0.2969
1.50	0.910	0.4334	0.2895
1.60	0.920	0.4392	0.2826
1.70	0.930	0.4483	0.2747
1.80	0.940	0.4535	0.2696
1.90	0.940	0.4545	0.2649
2.00	0.940	0.4489	0.2640

$$C_{Dfm} = \frac{(1 + 2s^2)}{\sqrt{\pi}\, s^3} \exp\left(\frac{-s^2}{2}\right) + \frac{(4s^4 + 4s^2 - 1)}{2s^4} \mathrm{erf}(s) + \frac{2\sqrt{\pi}}{3s} \sqrt{\frac{T_p}{T_f}} \qquad \text{(C.11)}$$

where

$$s = \sqrt{\frac{\gamma}{2}}\, M_r \qquad \text{(C.12)}$$

For the purposes of calculation, Walsh assumed that the temperature ratio in the last term of Equation C.11 was unity.

Walsh showed that this model agrees well with drag data for relative Mach numbers from 0.2 to 2.0, and for Reynolds numbers from 40 to 200. However, the model has no experimental support to justify its use in the region of relative Reynolds numbers of less than 40 and relative Mach numbers of less than 1 — precisely the region which is most likely to be encountered in supersonic LDV studies.

C.4 Results

In light of the above discussion of particle drag models and their ranges of applicability, it is important to outline the conditions experienced by the particles downstream of the oblique shock. Assuming that the particles were traveling with the flow immediately upstream of the shock, and assuming that the flow turned abruptly by 10°, the particles immediately downstream were at Mach 0.42 relative to the air. Based on the conditions described in the facilities section,

the mean free path of the molecules downstream of the shock was 0.053 μm. Therefore the Knudsen number was 0.089 for the 0.6 μm PSL particles and 0.036 for the 1.5 μm particles. The Reynolds number was 7.0 for the 0.6 μm PSL particles and 17.6 for the 1.5 μm particles. These numbers are typical of the conditions encountered in many blow down supersonic flow studies. For continuous tunnels, the total pressure would typically be lower, making the Knudsen number higher and the Reynolds number lower.

The LDV system measured the velocity of the particles downstream of the shock. Simultaneously, the total temperature of the flow was measured. In order to normalize the total temperature variation from run to run, the particle lag data are presented in terms of the measured Mach number, M_{meas}, which is the Mach number of air moving at the measured particle velocity, with the measured total temperature. M_{meas} is computed from Equation A.6 using the measured particle velocity in place of the gas velocity. The Mach number data are plotted in terms of M^*, which is the measured Mach number normalized by the difference between the upstream and the downstream Mach numbers as follows:

$$M^* = \frac{M_{meas} - M_y}{M_x - M_y} \tag{C.13}$$

The angular data are similarly normalized by the flow turning angle, $\delta = 10°$, so that α^* is equal to α/δ. Plotting the data in this reduced form not only simplifies the plot but also normalizes the calibration errors discussed in the uncertainty analysis section. Thus the error bars shown in Figure 46 and Figure 47 show only the uncertainty due to clock resolution and flow turbulence.

Measurements were made of the particle velocity and direction from 0.7 to 13.2 mm downstream of the shock. The results of these measurements are plotted with the predicted

particle behavior from the four particle drag models detailed above. The Stokes drag model is presented because it is a commonly used simple particle drag model. The White model is a simple correction to the Stokes drag formula which greatly extends the range of the model. The Carlson and Hoglund drag model is a more complicated model which purports to account for rarefaction and compressibility effects as well as inertia effects. Finally, the Walsh particle drag model is presented since it is the particle drag model which has been adapted to the widest range of experimental data.

Figure 46 shows the measured Mach number of the particles behind the shock while Figure 47 shows the angle of the particle trajectory behind the shock. From these plots it can be seen that for both the 0.6 μm and the 1.5 μm particles, the White model predicts the shortest relaxation distance. The Carlson and Hoglund model predicts a larger relaxation distance than the White model and the Stokes drag model predicts a larger relaxation distance than Carlson and Hoglund. The Stokes drag model over-predicts the lag because, at Reynolds numbers greater than 1, inertia effects become significant and the Stokes drag model predicts a C_D which is too low. The White model predicts the shortest relaxation distance since it does not include a correction for rarefaction effects of the Carlson and Hoglund model. The C_D for a particle in a rarefied gas is lower than that of a particle in a continuum. Even for Kn = 0.036, the C_D is reduced by about 10% compared to that in a continuum. The compressibility correction of the Carlson and Hoglund model has no effect on this comparison since the correction factor is very near 1 for relative Mach numbers below 0.5.

The results of the Walsh model are more complicated. The particles' initial response to the step change in velocity is similar to the response of the Carlson and Hoglund model. But, as the particles move downstream of the shock, and the particle Mach number becomes smaller, the particle response in the Walsh model becomes sluggish. This is because the Walsh model has

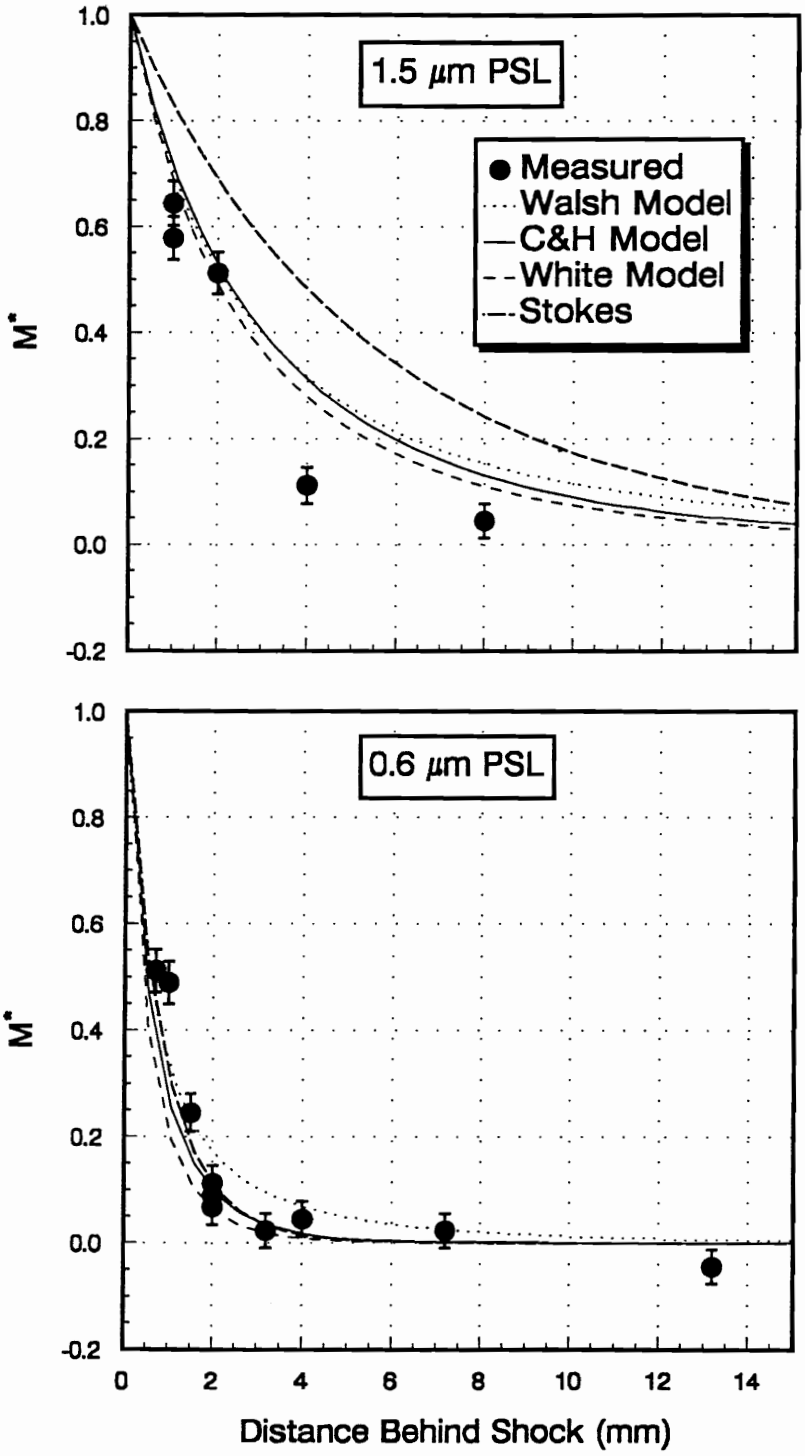

Figure 46. Normalized Particle Mach Number Across the Shock

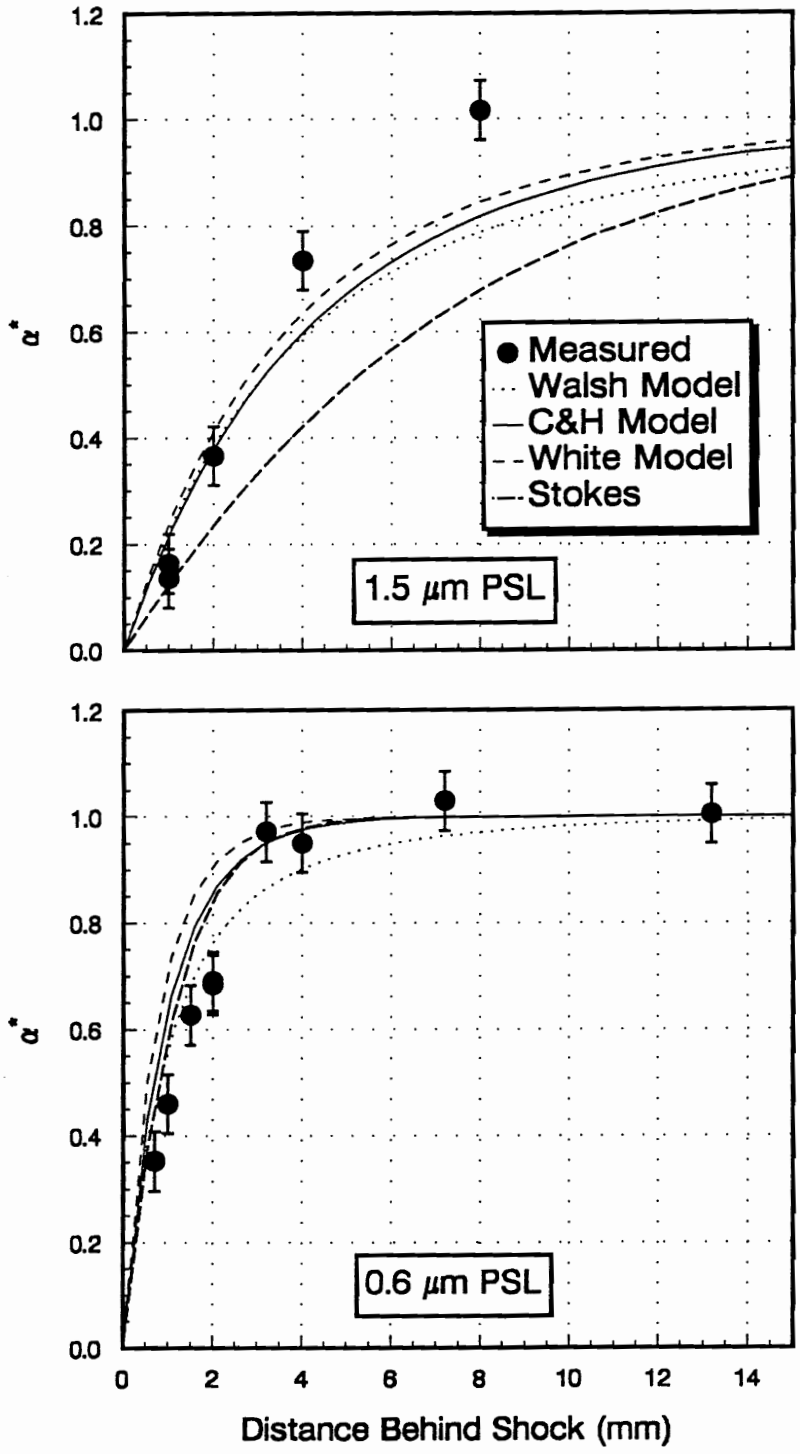

Figure 47. Normalized Particle Turning Across the Shock

been formulated for relative Mach numbers from 0.1 to 2.0, and the extrapolation to relative Mach numbers below 0.1 is of limited validity.

The experimental data show that the Stokes, White and Carlson and Hoglund drag models all closely predicted the behavior of the 0.6 μm particles. All predicted the approximately 3 mm relaxation distance in angle and Mach number measured in the wind tunnel. There is insufficient difference between the lag predictions of the three models to distinguish between them. The Walsh model predicted a relaxation distance of 8 to 10 mm, primarily because the model underestimates the C_D at low Mach numbers.

The measurements on the 1.5 μm particles show the particle lag predictions of all four models to be high. The Stokes drag model is particularly inaccurate for the 1.5 μm particles, which have a Reynolds number of 17.6 behind the shock. While the data show a relaxation distance of 8 to 10 mm for the 1.5 μm particles, the White, Carlson and Hoglund and Walsh models show relaxation distances of 17, 19, and 29 mm respectively.

C.5 Conclusions

No existing particle drag model has been experimentally verified for the conditions encountered by particles in the supersonic through-flow cascade. All models are based on data acquired at significantly different combinations of relative Mach and Reynolds numbers. The Stokes drag model in particular is inappropriate for supersonic LDV studies since it assumes particle Reynolds numbers less than 1. The White model is only valid for low relative Mach number flows with Knudsen numbers much less than 1. The model of Carlson and Hoglund is a correction to the Stokes drag model designed to be valid for a wide range of Mach number and

Reynolds number, but it's coefficients were determined by data only at relative Mach Numbers of 0.5. Walsh has developed a particle drag model which is based on a broad range of experimental data, but the model proved to be inadequate for this particular application since the model is not intended for low particle relative Mach numbers. The use of any of these models in supersonic LDV particle lag studies is an extrapolation of questionable validity.

Although the Carlson and Hoglund, Stokes, and White models adequately predicted the behavior of 0.6 μm particles, all reviewed models predicted the lag of 1.5 μm particles through the oblique shock to be greater than that which was measured. The conclusion which must be drawn from these results is not that all models are valid for the 0.6 μm particles and invalid for the 1.5 μm particles, but rather none of the models are valid for the conditions experienced by these particles. That the behavior of the 0.6 μm particles is predicted is only coincidence.

Though it is clear that the response of small particles to velocity gradients in supersonic flows is not adequately predicted by existing particle drag models, the mechanisms which cause the discrepancies are not well understood. At present, sufficient data to extend the particle drag models for typical supersonic LDV flow conditions do not exist. It must therefore be concluded that particle lag predictions should only serve as a guide to supersonic LDV seed selection. The actual response of seed in a supersonic flow should always be experimentally verified in a simple known flowfield such as the oblique shock used in this experiment. Failure to perform such a test on the seed could lead to misinterpretation of the data or to a non-optimal tradeoff between particle trackability and particle visibility.

C.6 Particle Lag in the STFF Cascade

Although the above experiment was performed under conditions which were similar to those found in the supersonic through-flow cascade, it must be remembered that an oblique shock of 10° turning is among the sharpest of gradients found in the STFF cascade. Through most of this flow, the gradients are not nearly so extreme, and the particle lag should be much less than that which was measured in the above experiment. A calculation was therefore performed to estimate the lag of the particle not just in the region of shocks, but throughout the entire cascade.

A representative flow through which the particle lag would be calculated was obtained from the CFD solution. A streamline was calculated from the CFD solution at design incidence starting from the passage entrance at $y/s = 0.85$. This streamline is illustrated in Figure 48. Particle lag was then calculated through a flow which had $u(x)$, $v(x)$, and $\rho(x)$ equal to the values calculated for the 85% streamline, but which did not vary in the y-direction. In this way the particle motion through a simplified, quasi 2-D flow was performed.

The calculation was performed for the 0.6 μm PSL particles used for the cascade LDV studies. Particle drag was modeled using the White method discussed above. The results of this particle lag calculation are summarized in Figure 49 and Figure 50. Figure 49 compares the particle velocity to the flow velocity, and Figure 50 compares the particle direction of motion to the flow angle. In both these figures it can be seen that the particle lag is negligible through most of the blade passage. The calculation shows that the velocity lag is generally less than 0.5% and the angular lag generally less than 0.3°. Only in the immediate vicinity of the shocks is there any significant lag.

The lag of the seed particles in the STFF cascade should then only have a minor effect

Figure 48. Streamline Used for STFF Particle Lag Analysis

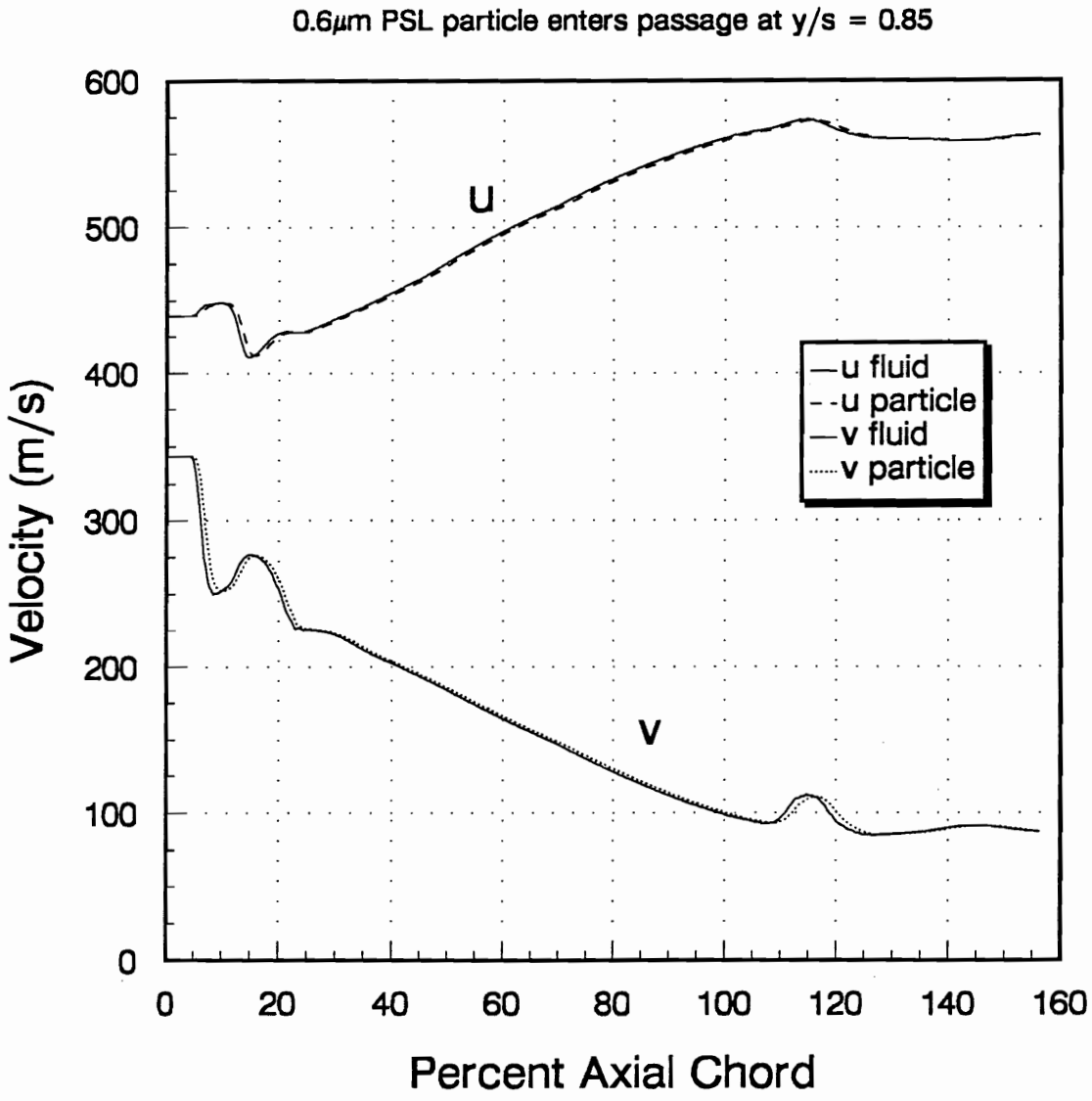

Figure 49. Particle Velocity Through the STFF Cascade

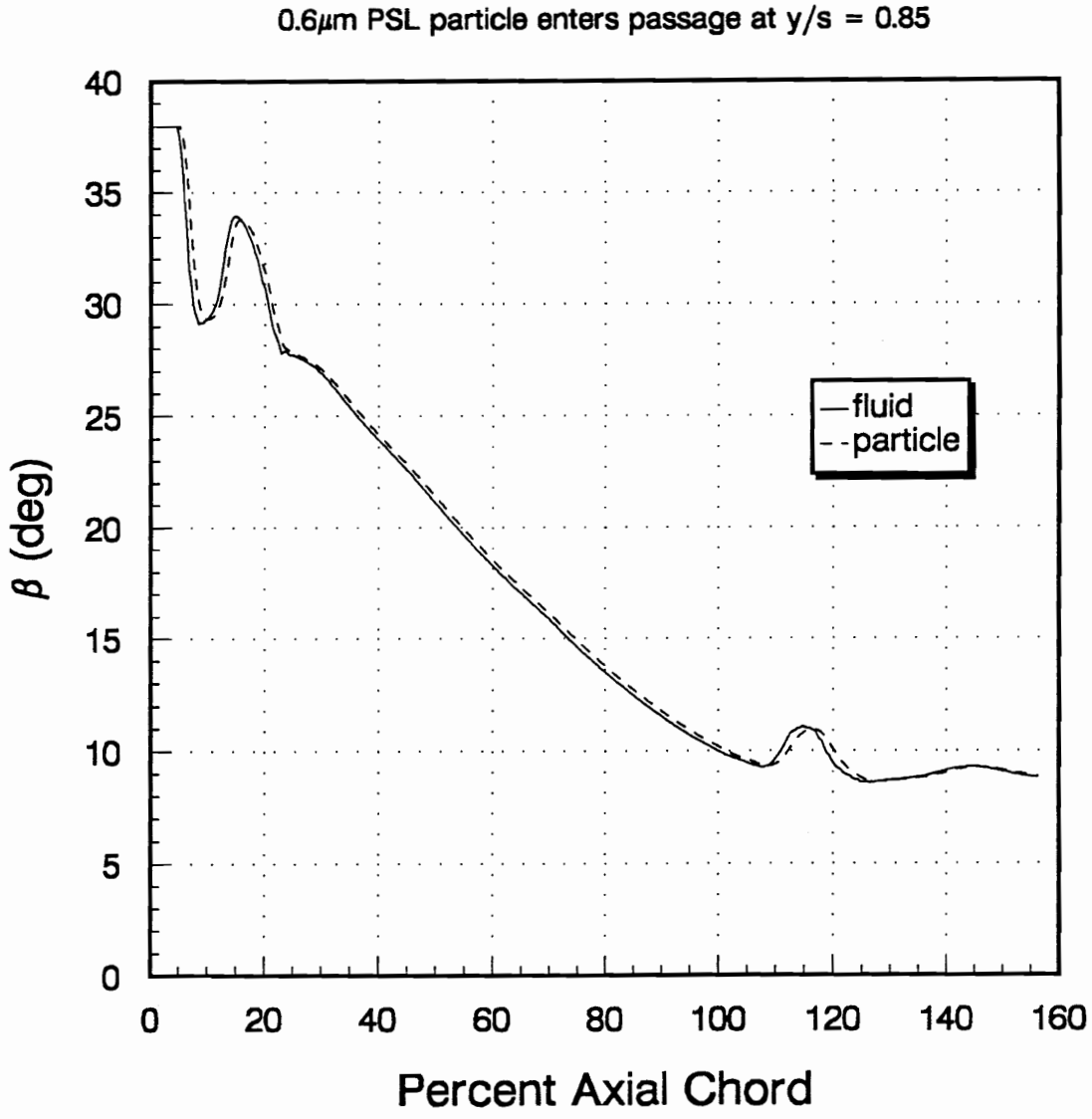

Figure 50. Particle Turning Through the STFF Cascade

on the accuracy of the LDV mean flow measurements. Through most of the blade passage, particle lag is negligible. The lag of the 0.6 μm particles is only significant in very small regions of the flowfield. It is therefore concluded that the 0.6 μm particles are suitable for use in LDV studies of the STFF cascade.

Appendix D

Downstream Rake Profiles

Downstream of the cascade, the Pitot/static probe was used to make measurements of the Pitot pressure and static pressure across the blade passage. From these two measurements the total pressure and the Mach number could be calculated. The full set of these measurements is presented in Figure 51 through Figure 57.

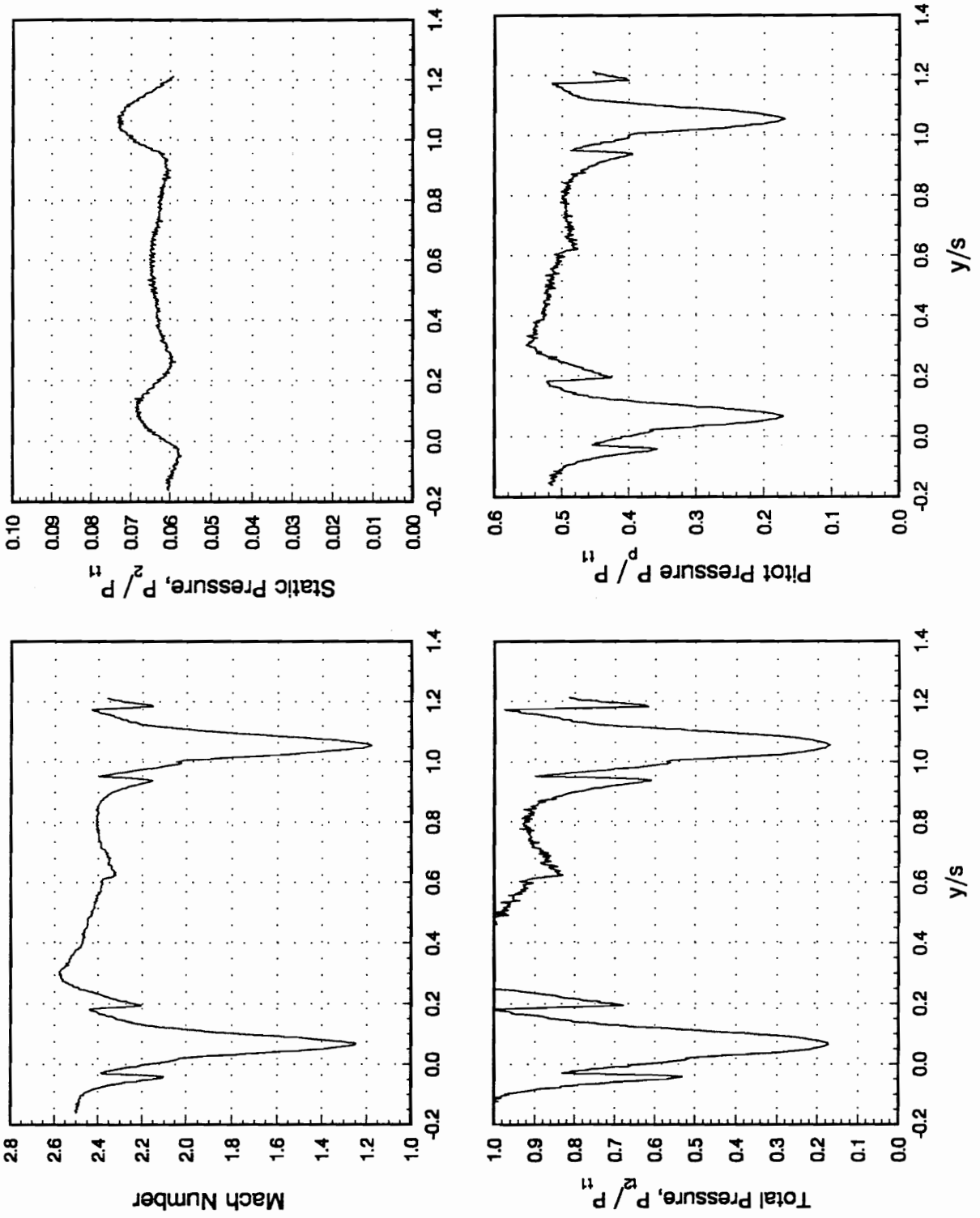

Figure 51. Pitot/Static Downstream Measurements, Design Incidence, $x/c = 0.11$

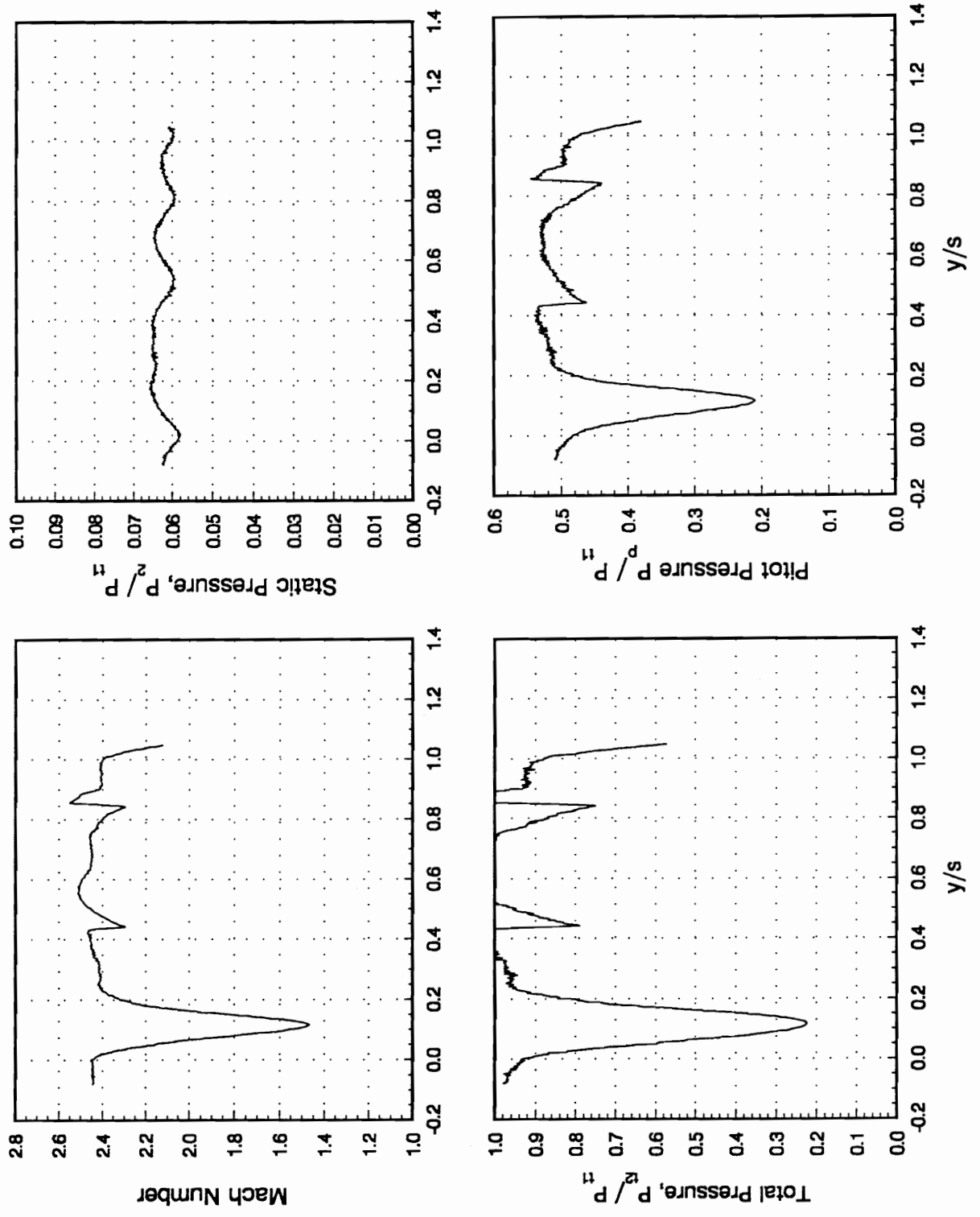

Figure 52. Pitot/Static Downstream Measurements, Design Incidence, $x/c = 0.24$

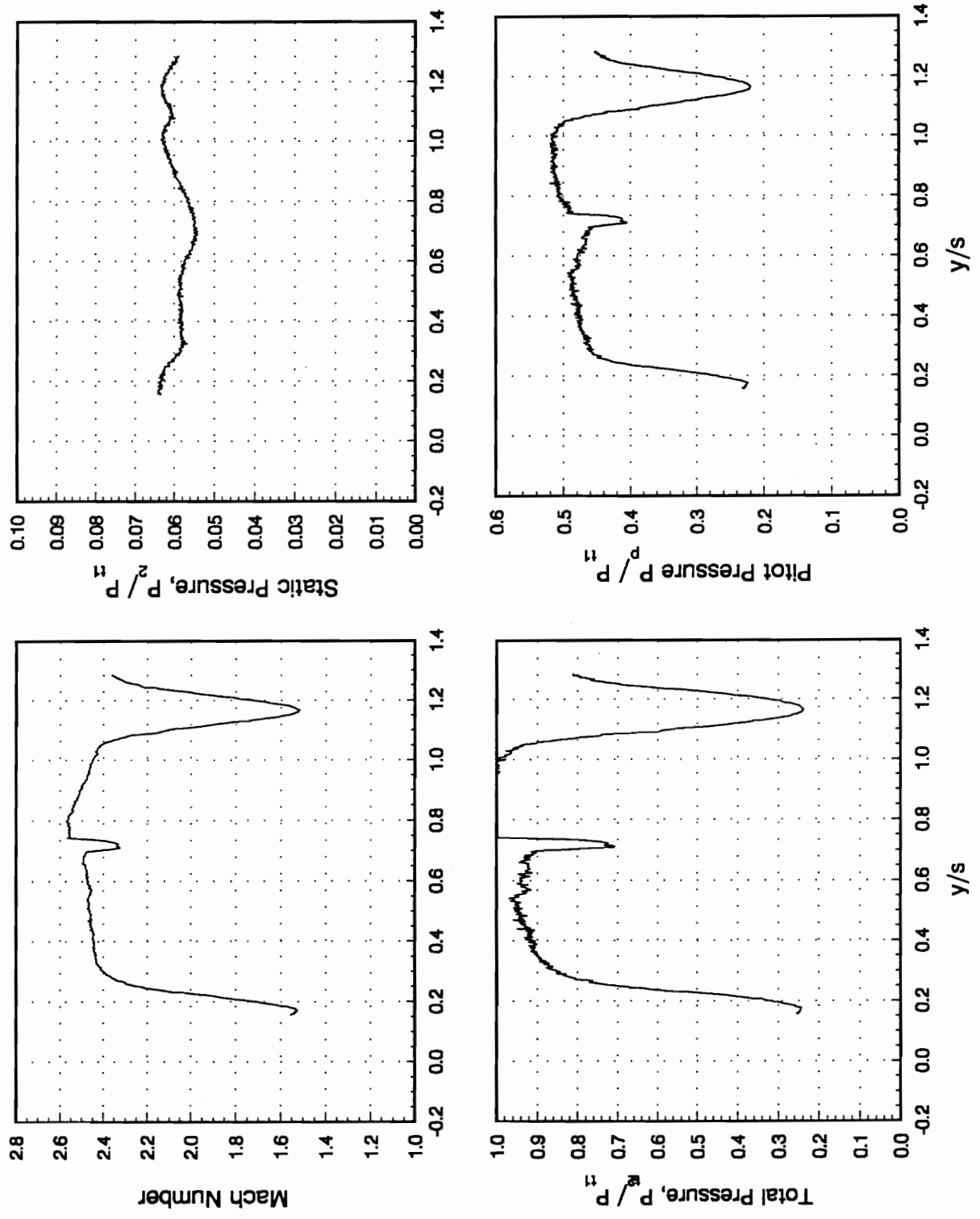

Figure 53. Pitot/Static Downstream Measurements, Design Incidence, x/c = 0.37

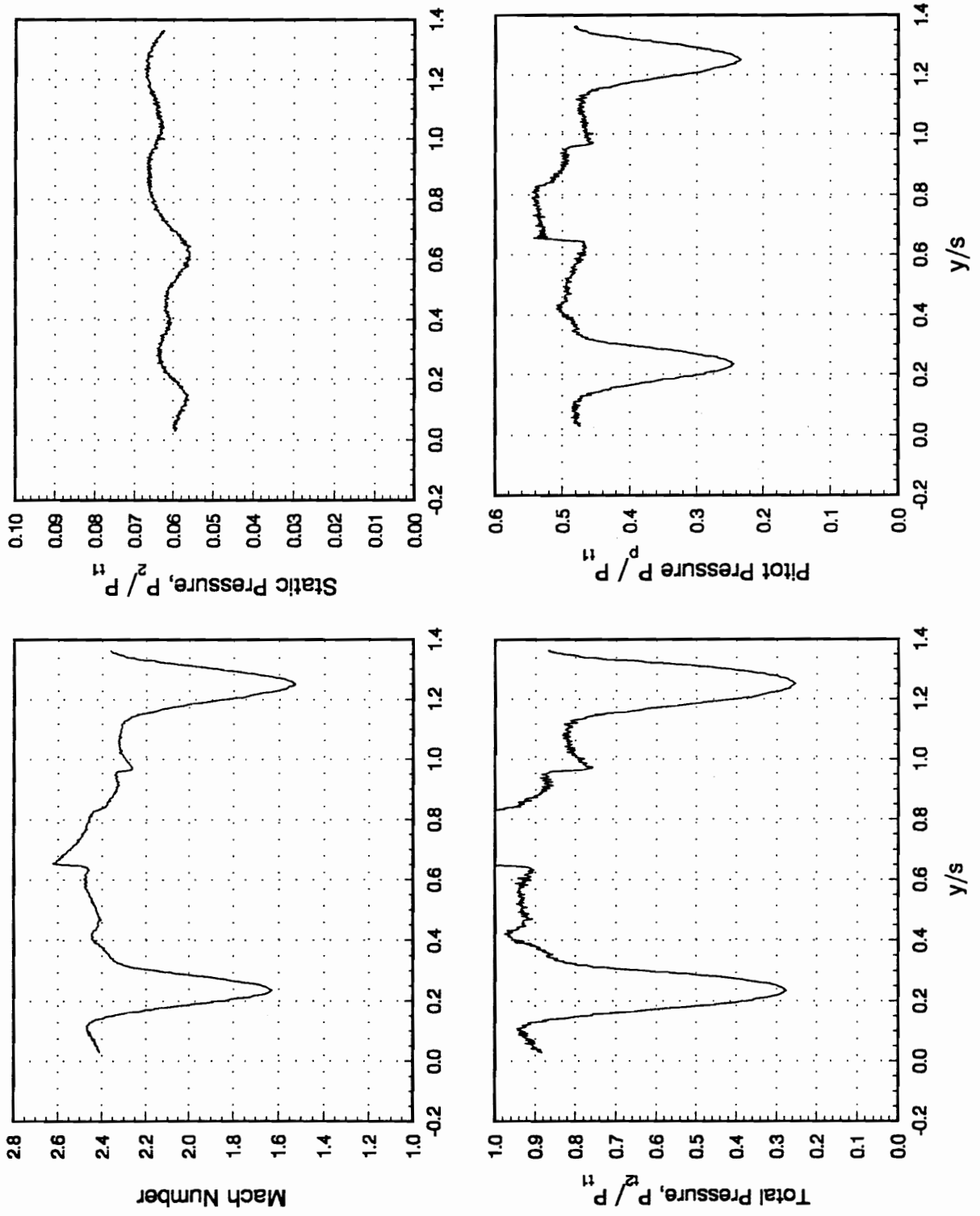

Figure 54. Pitot/Static Downstream Measurements, Design Incidence, x/c = 0.50

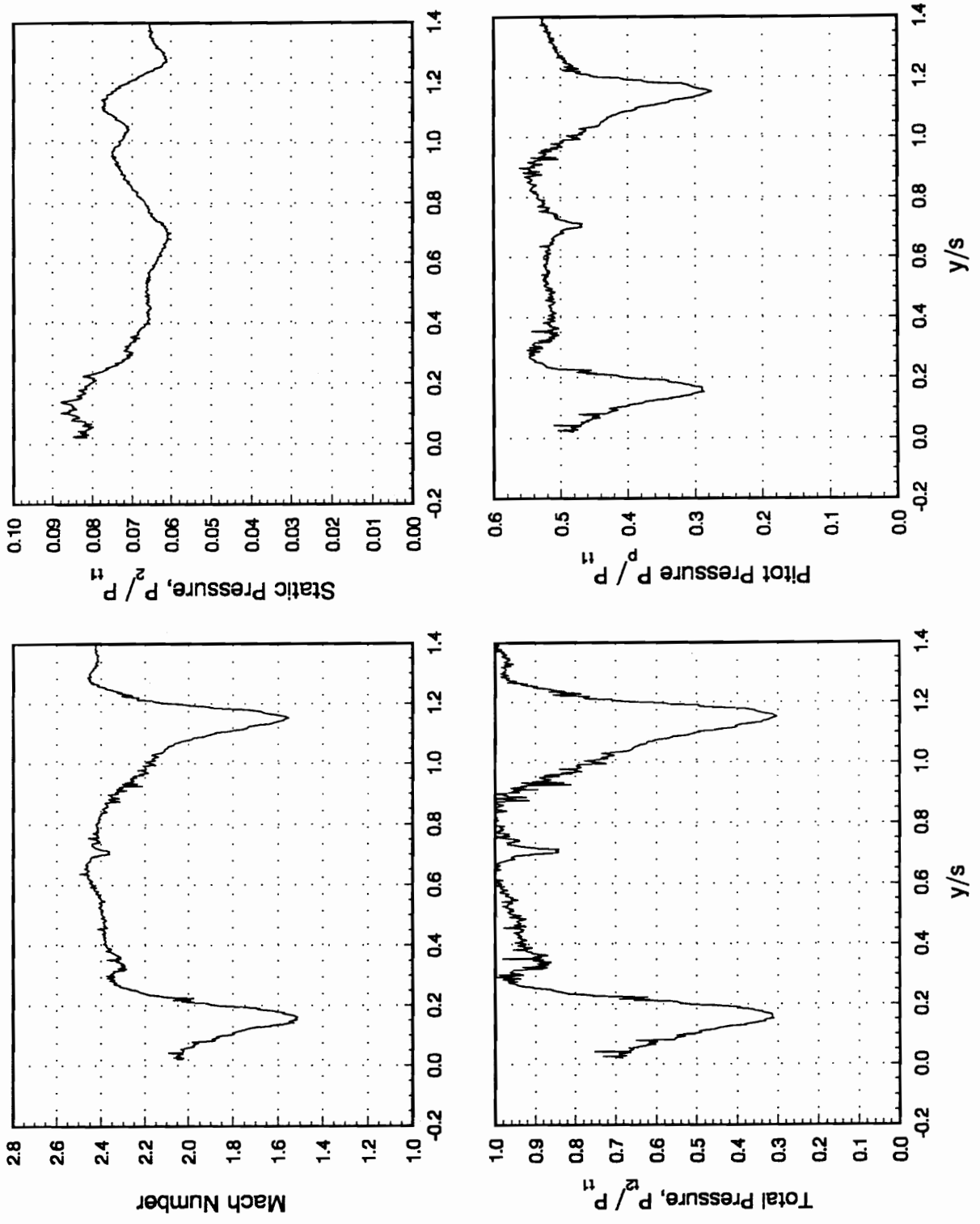

Figure 55. Pitot/Static Downstream Measurements, -10° Incidence, x/c = 0.37

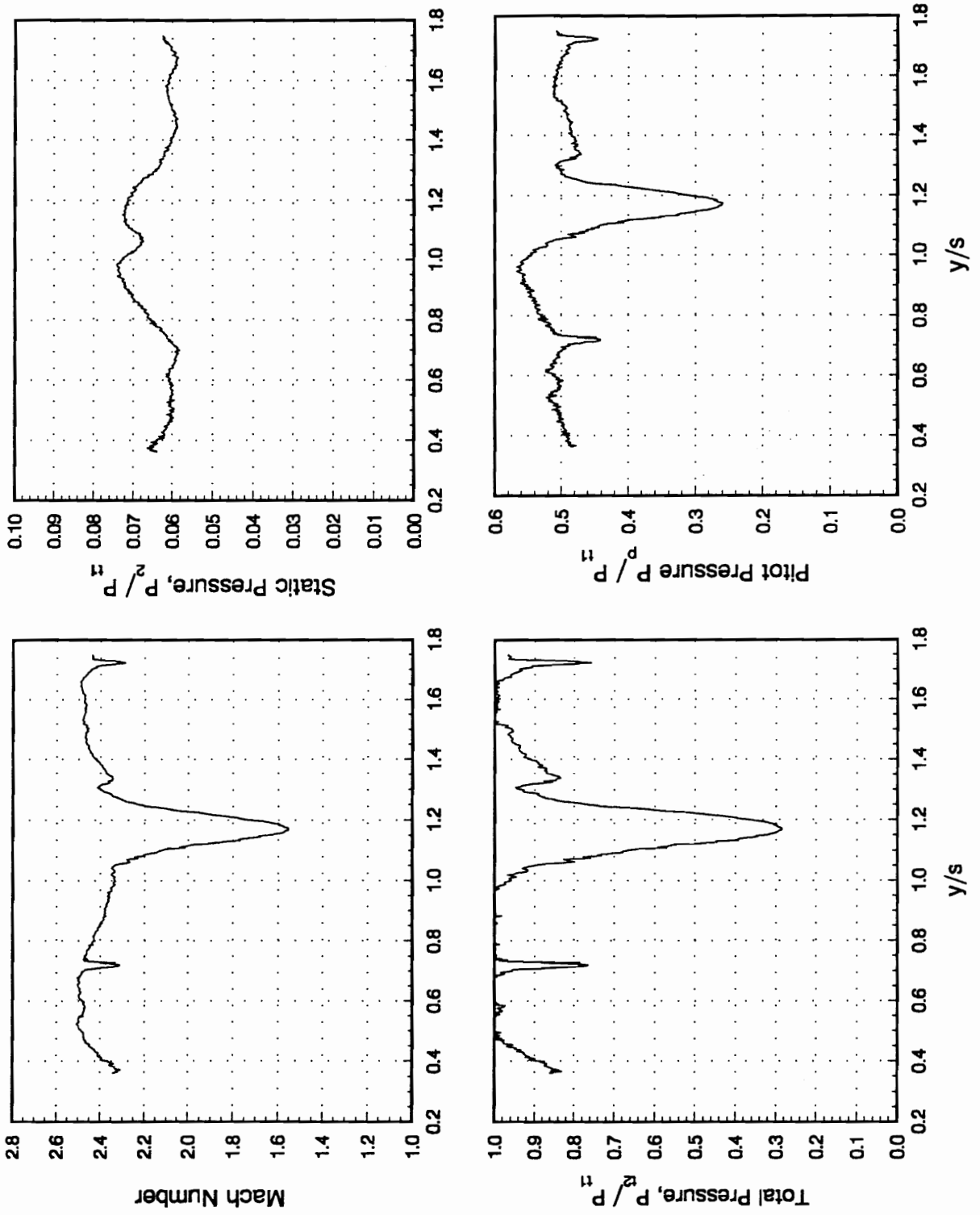

Figure 56. Pitot/Static Downstream Measurements, -5° Incidence, x/c = 0.37

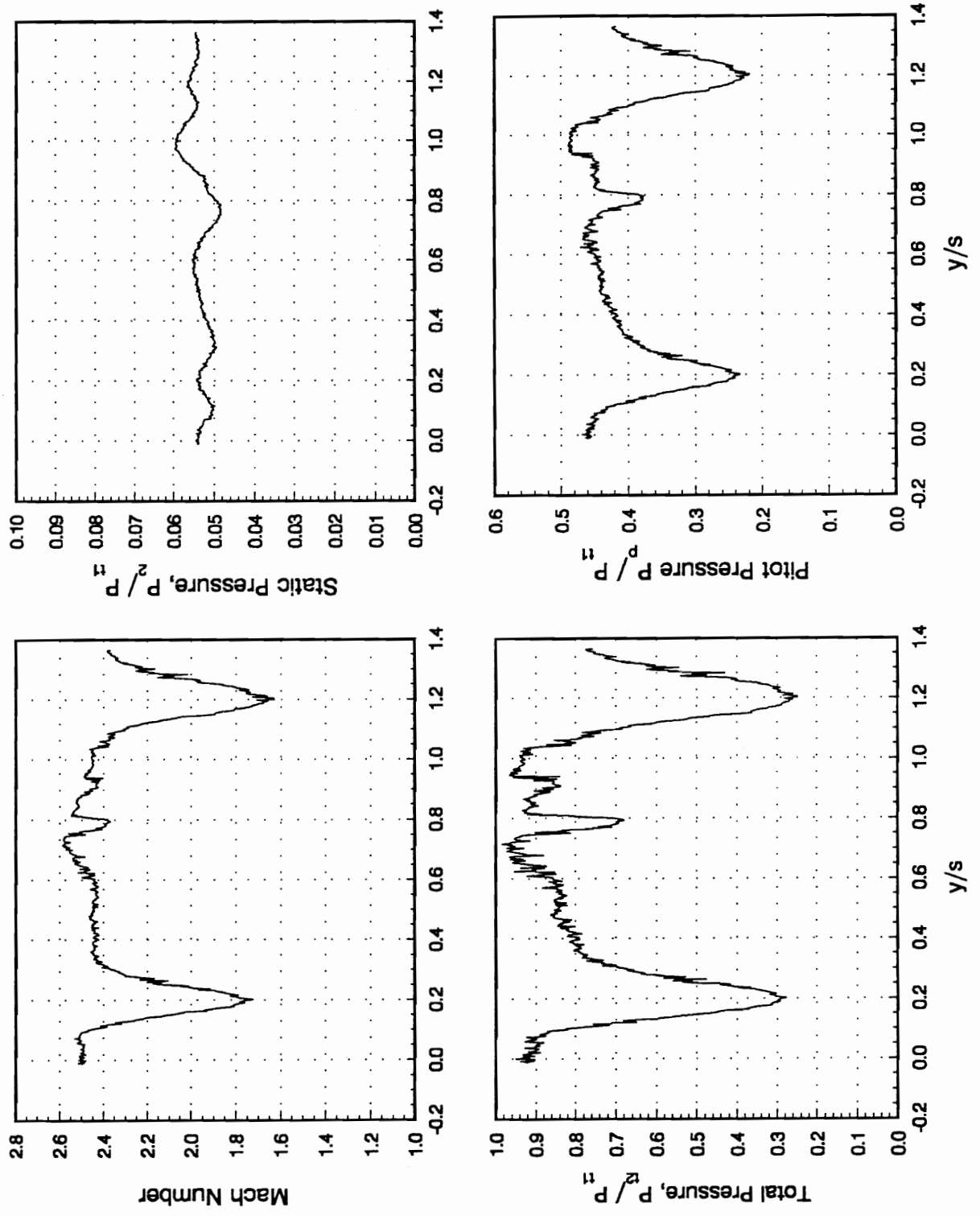

Figure 57. Pitot Static Downstream Measurements, +5° Incidence, x/c = 0.37

References

1. Ferri, A., "Problems Related to Matching Turbojet Engine Requirements to Inlet Performance as Function of Flight Mach Number and Angle of Attack," *Air Intake Problems in Supersonic Propulsion*, J. Fabri, ed., AGARDograph No. 27, AGARD, France, 1956.

2. Trucco, H., "Study of Variable Cycle Engines Equipped With Supersonic Fans, Final Report," (ATL TR 201, Advanced Technology Laboratories Inc., NAS-17559), NASA CR-134777, 1975.

3. Tavares, T. S., "A Supersonic Fan Equipped Variable Cycle Engine for a Mach 2.7 Supersonic Transport," NASA CR-177141, 1985.

4. Champagne, G. A., "Payoffs for Supersonic Through Flow Fan Engines in High Mach Transports and Fighters," *AIAA paper 88-2945*, 1988.

5. Franciscus, L. C., and Maldonado, J. J., "Supersonic Through-Flow Fan Engine and Aircraft Mission Performance," *AIAA Paper 89-2139*, 1989.

6. Savage, M., Boxer, E., and Erwin, J. R., "Resume of Compressor Research at the NACA Langley Laboratory," *Journal of Engineering for Power*, Vol. 83, No. 3, July 1961, pp. 269 - 285.

7. Breugelmans, F. A. E., "The Supersonic Axial Inlet Component in a Compressor," *ASME paper 75-GT-26*, March 1975.

8. Schmidt, J. F., Moore, R. D., Wood, J. R., and Steinke, R. J., "Supersonic Through-Flow Fan Design," *AIAA paper 87-1746*, June 1987.

9. Bowersox, R. D. W., "Meanflow and Turbulence Measurements in the Wake of a Supersonic Through-Flow Fan Cascade," Masters Thesis, VPI&SU Aerospace Engineering Department, January 1990.

10. Seegmiller, H. L., "Seeding Subsonic, Transonic and Supersonic Flows with 0.5 Micron Polystyrene Spheres," *Wind Tunnel Seeding Systems of Laser Velocimeters*, NASA Conference Publication 2393, 1985.

11. Schreiber, H. A., "Experimental Investigations on Shock Losses of Transonic and Supersonic Compressor Cascades", *Transonic and Supersonic Phenomena in Turbomachines*, AGARD CP 401, 1986.

12. Taylor, A. C., III, "Convergence Acceleration of Upwind Relaxation Methods for the Navier-Stokes Equations", PhD Dissertation, Virginia Polytechnic Institute and State University, July, 1989.

13. Andrew, P. L., Virginia Polytechnic Institute and State University Department of Mechanical Engineering, personal communication, to be published in future doctoral thesis, October, 1990.

14. Moeckel, W. E., "Approximate Method for Predicting the Form and Location of Detached Shock Waves Ahead of Plane or Axially Symmetric Bodies", NACA TN 1920, July 1949.

15. Goldstein, S., "A Note on the Measurement of Total Head and Static Pressure in a Turbulent Stream," *Proceedings of the Royal Society of London, Series A*, Vol. 155, No. 886, London, July 1, 1936.

16. Volluz, R. J., *Handbook of Supersonic Aerodynamics*, Section 20, "Wind Tunnel Instrumentation and Operation," NAVORD Report 1488, vol. 6, January 1961.

17. Wegener, P. P., and Mack, L. M., "Condensation in Supersonic and Hypersonic Wind Tunnels," *Advances in Applied Mechanics*, Volume V, New York, Academic Press Inc., 1958, pp. 307-447.

18. Dadi, M., "Étude de Modèles de Comportement de Traceurs Dans un Écoulement et Leur Validation Expérimentale par Vélocimétrie Holographique à Expositions Multiples," ONERA Technical Report 87/30, 1988.

19. Samimy, M., and Abu-Hijleh, B. A., "Performance of Laser Doppler Velocimeter with Polydisperse Seed Particles in High-Speed Flows," *Journal of Propulsion and Power*, Vol. 5, No. 1, January-February 1989.

20. Walsh, M. J., "Influence of Particle Drag Coefficient on Particle Motion in High-Speed Flow With Typical Laser Velocimeter Applications," NASA TN D-8120, February 1976.

21. Maxwell, B. R., and Seaholtz, R. G., "Velocity Lag of Solid Particles in Oscillating Gases and in Gases Passing Through Normal Shock Waves," NASA TN D7490, 1974.

22. Carlson, D. J., and Hoglund, R. F., "Particle Drag and Heat Transfer in Rocket Nozzles," *AIAA Journal*, Vol. 2, No. 11, November 1964, pp. 1980-1984.

23. Hjelmfelt, A. T. Jr., and Mockros, L. F., "Motion of Particles in a Turbulent Fluid," *Applied Scientific Research*, vol. 16, pp. 149-161, 1966.

24. White, F. M., *Viscous Fluid Flow*, New York: McGraw-Hill, 1974, p. 209.

25. Millikan, R. A., "The General Law of Fall of a Small Spherical Body Through a Gas and its Bearing Upon the Nature of Molecular Reflection From Surfaces," *Physics Review*, No. 22, pp. 1-23, 1923.

26. Torobin, L. B., and Gauvin, W. H., "Fundamental Aspects of Solids-Gas Flow," *Canadian Journal of Chemical Engineering*, Vol. 37, No. 4, August 1959, pp. 129-141.

27. Hoerner, S. F., "Fluid-Dynamic Drag," Published by the author, 148 Busteed Drive, Midland Park, New Jersey 07432, 1965.

28. Stadler, J. R., and Zurick, V. J., "Theoretical Aerodynamic Characteristics of Bodies in a Free-Molecule-Flow-Field," NACA TN 2423, 1951.

29. Maxwell, B. R., and Seaholtz, R. G., "Velocity Lag of Solid Particles in Oscillating Gases and in Gases Passing Through Normal Shock Waves," NASA TN D-7490, March 1974.

30. Cuddihy, W. F., Beckwith, I. E. and Schroeder, L. C., "Flight Test and Analysis of a Method for Reducing Radio Attenuation During Hypersonic Flight," NASA TM X-1331, 1967.

31. Emmons, H. W., ed., *Fundamentals of Gas Dynamics*, Volume III, Princeton University Press, 1958.

Vita

Christopher J. Chesnakas was born in Nashua, New Hampshire on September 10, 1963. Shortly thereafter, he moved to Baltimore, Maryland. In September of 1981 he entered Virginia Polytechnic Institute and State University. While at VPI he co-oped at the Army Materiel Systems Analysis Activity at Aberdeen Proving Ground in Maryland. In June of 1986 he received his Bachelor of Science in Mechanical Engineering, Summa Cum Laude.

He began work on his Master of Science degree at in September of 1986 at VPI, working with Dr. Clinton L. Dancey of the Mechanical Engineering Department. In February of 1988 he completed his thesis entitled "Total Velocity Vector Measurements in an Axial-Flow Compressor using a 3-Component Laser Doppler Anemometer." He then started work on his Doctor of Philosophy program in March of 1988. In July of 1989 he received the Gordon C. Oates Air Breathing Propulsion Award from the AIAA at the Joint Propulsion Conference in Monterey, California. This award was received for work in progress on his PhD program.

After completing his degree, he plans to work with Dr. Roger Simpson of the Aerospace and Ocean Engineering department of Virginia Polytechnic Institute. He will be working on the development of miniature fiber-optic LDV probes.